UNIVERSITY of CALIFORNIA

Santa Barbara

Molecular Design, Simulation and Synthesis of Narrow-Bandgap Organic Semiconductors for Near-Infrared Optoelectronics Applications

A dissertation submitted in partial satisfaction of the requirements for the degree

Doctor of Philosophy in Chemistry

by

Ziyue Zhu

Committee in charge:

Professor Guillermo C. Bazan, Chair

Professor Javier Read de Alaniz

Professor Thuc-Quyen Nguyen

Professor Trevor W. Hayton

March 2023

The dissertation of Ziyue Zhu is approved.

Professor Javier Read de Alaniz, Exam Chair

Professor Thuc-Quyen Nguyen

Professor Trevor W. Hayton

Professor Guillermo C. Bazan, Thesis Chair

March 2023

Molecular Design, Simulation and Synthesis of Narrow-Bandgap Organic Semiconductors for Near-Infrared Optoelectronics Applications

by

Ziyue Zhu

dedicated to friends and family who have supported me,

colleagues who have guided and challenged me,

and all those who share a passion for science

Acknowledgements

"Rome was not built in a day", and the same can be said for completing the doctoral program. I am deeply grateful for the support and assistance of the numerous individuals and organizations who have contributed to the research presented in this work over the past five years.

First and foremost, I'd like to express my deepest gratitude to my supervisors, Prof. Guillermo C. Bazan and Prof. Javier Read de Alaniz for their invaluable guidance, support, and mentorship throughout my Ph.D. journey. Their expertise, insights, and constructive feedback have been instrumental in shaping my research and helping me grow both academically and personally. My first opportunity to work in a lab came in my first quarter as graduate students. After knowing Gui in the UCSB Chemistry Department area-advisor meeting section, I'm impressed his research area diversities, varying from traditional organic semi-conductors synthesis and applications to bio-electronic devices and anti-biotics drug development. I was also amazed by how well his research transition from traditional methodology studies to organic semiconducting solids has been after he started his own research group, which is exactly what I'm interested in since I wanted to research more on organic materials development and their applications after obtaining basic organic synthetic capability in my undergrad research group of Prof. Xumu Zhang's studying on phosphine ligand based catalysis. After joining Gui's group, I'm also amazed by his remarkable ability to recognize critical challenges and devise innovative solutions to complex problems, which I have been learning a lot from. He has also been a great mentor and supervisor in terms of sharing his experience in academia, encouraging my growth as a scientist. However, thing become more harder with Gui's decision to move to NUS, Singapore. I believe that I can not

make it to the completion of my Ph.D. program without Prof. Javier Read de Alaniz's help. Upon joining the Read group, I was impressed by his ability to manage a large group of over 20 graduate and post-doctoral researchers. Fortunately, I found myself working alongside a harmonious team, with Javier serving as my co-advisor. As an outstanding organic chemist and wise supervisor, he was always available to help me with any research-related questions, particularly regarding synthesis. His generosity in providing advice and guidance on my career development has been invaluable. I'm lucky to have the opportunity to work closely with Prof. Thuc-Quyen Nguyen, who generously shared her inspiring journey as a successful women scientist and provided me with valuable feedback and guidance on my research projects. Her encouragement to interact with colleagues at conferences and networking events has been instrumental in helping me develop as a scientist. Although I was not in her group, but I literally work closely with her group as part of the member. I would also like to thank my other committee member, Prof. Trevor W. Hayton, who has always offered valuable guidance in my graduate program checking the progress and timeline when I met with him.

I would also like to thank all my mentors who have helped me in grad-school without whom I would not have been able to reach this milestone. When I first joined the Bazan group, Prof. Jaewon Lee took me under the wing and taught me everything I need to learn for completing a scientific research project and led me to the concept of non-fullerene acceptor which is the start and most essential part of my PhD research. I am also deeply grateful to Dr. Martin Seifrid, Dr. Seyeong Song, Dr. Alex Moreland and Dr. Jianfei Huang, who have played crucial roles as collaborators, colleagues, mentors, and friends in my growth as a graduate student and scientist, none of my research projects presented in the following thesis chapters could have been accomplished without them. There are many other people from whom I have learned a

lot and who have made CPOS and UCSB a great place to be over the past five years: Luana Llanes, Elena Nicolae, Bing Wang, Chenyao Nie, Lingyun Zhou, Ming Wang, Cheng Zhang, Samantha McCuskey, Ke Zhao, Yang Li, Zongheng Wang, Hoang Luong, Hengbin Wang, Nora Schopp, Sangcheol Yoon, Sangmin Chae, Tung Nguyen-Dang, Joachim Vollbrecht, Seo-Jin Ko, Viktor Brus, Seojin Oh, and Allison Abdilla. I'm especially thankful for my closes friend, collaborator and significant other Zhifang Du for showing up in my life making the hard long journey exciting and colorful. I would also like to acknowledge the funding agencies of MC-CAM and AFOSR for their financial support om my last five years research projects.

Last but not the least, I would like to express my heartfelt gratitude to my family, especially my enlightened mother, for their unwavering support and encouragement throughout my academic journey. As a first-generation student pursuing higher education and scientific research, I recognize that none of my achievements would have been possible without their selfless guidance and motivation. Their belief in my potential has been an invaluable source of strength and inspiration, and I am truly grateful for all that they have done for me.

Curriculum Vitae

EDUCATION

Doctor of Philosophy in Chemistry, University of California, Santa Barbara, March 2023 (expected)

Bachelor of Science in Chemistry, Wuhan University, Wuhan, China, June 2017

RESEARCH EXPERIENCE

Graduate Student Researcher – Department of Chemistry and Biochemistry, University of California, Santa Barbara (Bazan Lab, Fall 2018 – present).

Teaching Assistant – Department of Chemistry and Biochemistry, University of California, Santa Barbara (2017 – 2018).

Research Internship – University of Calgary, MITACS Program (Baumgartner Lab, Summer 2016).

Undergraduate Student Researcher – Department of Chemistry and Biochemistry, Wuhan University (Zhang Lab, 2014-2017).

PUBLICATIONS

1. **Zhu, Z**., Bazan, G. C. et al., Toluene-Processed Semitransparent Optoelectronic Devices Based on Narrow Bandgap Composition of Donor Polymer and Non-Fullerene Acceptors. (*In Prep*.)
2. **Zhu, Z**., Bazan, G. C. et al., C-O Bridged Fused Ring Narrow Bandgap NFAs for NIR Organic Photodetectors. (*In Prep.*)
3. Zhou, C.; Li, Z.; **Zhu, Z**.; Chia, G. W. N.; Mikhailovsky, A.; Vázquez, R. J.; Chan, S. J. W.; Li, K.; Liu, B.; Bazan, G. C. Conjugated Oligoelectrolytes for Long-Term Tumor Tracking with Incremental NIR-II Emission. *Advanced Materials* 34.20 (**2022**): 2201989.
4. Halaby, S.; Martynowycz, M. W.; **Zhu, Z**.; Tretiak, S.; Zhugayevych, A.; Gonen, T.; Seifrid, M. Microcrystal Electron Diffraction for Molecular Design of Functional Non-Fullerene Acceptor Structures. *Chem. Mater.* **2021**, 33 (3), 966–977.

5. Lee, J.; Song, S.; Huang, J.; Du, Z.; Lee, H.; **Zhu, Z**.; Ko, S.-J.; Nguyen, T.-Q.; Kim, J. Y.; Cho, K.; Bazan, G. C. Bandgap Tailored Nonfullerene Acceptors for Low-Energy-Loss Near-Infrared Organic Photovoltaics. *ACS Materials Lett.* **2020**, *2* (4), 395–402.
6. Huang, J.; Lee, J.; Vollbrecht, J.; Brus, V. V.; Dixon, A. L.; Cao, D. X.; **Zhu, Z**.; Du, Z.; Wang, H.; Cho, K.; Bazan, G. C.; Nguyen, T.-Q. A High-Performance Solution-Processed Organic Photodetector for Near-Infrared Sensing. *Advanced Materials* **2020**, *32* (1), 1906027.
7. Lee, J.; Ko, S.-J.; Lee, H.; Huang, J.; **Zhu, Z**.; Seifrid, M.; Vollbrecht, J.; Brus, V. V.; Karki, A.; Wang, H.; Cho, K.; Nguyen, T.-Q.; Bazan, G. C. Side-Chain Engineering of Nonfullerene Acceptors for Near-Infrared Organic Photodetectors and Photovoltaics. *ACS Energy Lett.* **2019**, *4* (6), 1401–1409.
8. Tan, X.; Wang, G.; **Zhu, Z**.; Ren, C.; Zhou, J.; Lv, H.; Zhang, X.; Chung, L. W.; Zhang, L.; Zhang, X. Hydrogenation of Aldehydes Catalyzed by an Available Ruthenium Complex. *Org. Lett.* **2016**, *18* (7), 1518–1521.
9. Wang, Q.; Tan, X.; **Zhu, Z**.; Dong, X.-Q.; Zhang, X. New Synthetic Strategy for Chiral 2-Oxazolidinones Derivatives via Rhodium-Catalyzed Asymmetric Hydrogenation. *Tetrahedron Letters* **2016**, *57* (6), 658–662.

PATENTS

1. Bazan, G., Lee J., Song, S., **Zhu, Z**., Nguyen, T., Ko, S.J. Compositions and Methods of Fabrication of Near-Infrared Devices. United States provisional patent US62/965,620.
2. Bazan, G., Song, S., **Zhu, Z**., and Wang, H. Ultra Narrow Bandgap Non-Fullerene-Acceptor Based Organic Electronics. UC Case 2021-876.

CONFERENCES AND PRESENTATIONS

08/2022 Z. Zhu, Z. Du, G.C. Bazan, T. Nguyen, “Green Solvent Processed Semitransparent NIR-Photodetector” Poster, SPIE Organic Photonics + Electronics, San Diego

06/2021 Processing of Organic Semiconductors from High Dielectric Media, Poster Presentation, AFOSR Annual Review

01/2021 Molecular Engineering of Non-Fullerene Acceptors for Semi-Transparent Organic Near Infrared Optoelectronics, CPOS Talk, UCSB

04/2020 Molecular Engineering of Non-Fullerene Acceptors for Near-Infrared Optoelectronics Applications, CPOS Talk, UCSB

06/2019 Semi-Transparent Organic Solar Cells: Opportunities and Challenges, CPOS Talk, UCSB

AWARDS

Academic Senate Doctoral Student Travel Grant, UCSB, 2022

Chair's Fellowship from the Department of Chemistry & Biochemistry, UCSB, 2022

"Journal of Materials Chemistry C Poster Prize" for the SPIE conference session, 2022

Chemistry Department Honors, Wuhan University, 2017

Mitacs & China Scholarship Council Scholarship, 2016

First Class Outstanding Scholarship (Top 5%), Wuhan University, 2016

First Class Hongyi Scholarship, Wuhan University, 2015

ACTIVITIES AND INVOLVEMENT

Graduate Volunteer for Scientific Outreach, MRL, UCSB 2022-2022

Committee Member of CDEI, Chemistry Department, UCSB 2020-2022

Abstract

Molecular Design, Simulation and Synthesis of Narrow-Bandgap Organic Semiconductors for Near-Infrared Optoelectronics Applications

by

Ziyue Zhu

The development of near-infrared (NIR) non-fullerene acceptors (NFAs) has led to a surge in research interest in semitransparent organic optoelectronics, such as solar cells and photodetectors. These technologies offer numerous advantages, including ultra-thin film processibility, synthetic flexibility, and low-cost solution-based techniques for potential industrial applications. However, the interaction between solvents and bulk-heterojunction (BHJ) components can significantly impact the film morphology and blends self-assembly. To achieve high efficiency in fullerene-free optoelectronics using halogenated solvents, there is a strong focus on processing the active layer from low-cost and eco-friendly solvents derived from renewable resources. Chlorine-free solvents such as toluene, xylene, tetrahydrofuran (THF), and 2-methyl THF are preferentially chosen for green solvent processed organic optoelectronics.

The first two chapters of this thesis introduce the molecular engineering of narrow bandgap NFAs based on the original structure of published near-infrared absorber COTIC-4F molecule. The impact of side chain modification on the optoelectronic properties of NFAs built on the COTIC-4F conjugated framework has been examined and tested within the applications of corresponding organic solar cells and NIR-OPDs. Via modification on the center donor core,

a set of C-O bridged NFAs CO6ICs have been successfully synthesized and applied into NIR-OPDs achieving high responsivity at NIR-region. Moreover, those set of small molecular NFAs have presented promising processibility in “green solvent” of 2-MeTHF. This leads to the following chapter of this thesis presenting a project investigating molecular engineering of green solvent processable A-D’-D-D’-A structured non-fullerene acceptors (NFAs). These NFAs exhibit high solubilities and potential processability in 2-MeTHF. By using DFT and HSP simulation of the small molecules, and various thin-film characterization techniques (UV-vis, AFM, GIWAXS) on the 2-MeTHF solvent-cast thin-films, a better understanding of the materials' chemical structural influences on NFAs' green solvent processibilities and their corresponding solid-state properties is achieved.

The last chapter of this contribution focus on the molecular design and synthesis of a series of ultra-narrow bandgap NFAs and their efficient NIR-OPDs applications processed from non-halogenated solvent of toluene. Systematic modifications on the end-dye acceptor halogen substituents within the framework were made to investigate the influence of the electron negativity of terminated groups on the materials' optical properties and the corresponding device performance. Semitransparent organic optoelectronic devices were fabricated with the originally designed NFAs and processed using chlorobenzene and toluene as non-halogenated solvents for comparison. Toluene-based devices achieved higher specific detectivity due to the better quality of blend thin-film morphologies and more compacted crystallinity in the photoactive layer. This confirms that this novel series of DaTICs NFAs have satisfying chlorine-free solvent processibilities without sacrificing device performance.

Contents

List of Figures

List of Tables

I. Introduction

I.1 Organic semiconductors, their function in organic electronics, the challenges, and opportunities

Organic semiconductors have revolutionized the field of electronics by offering a range of benefits over traditional inorganic semiconductors. Unlike traditional inorganic semiconductors, which are typically made from silicon, germanium, or other inorganic materials, organic semiconductors are based on carbon-based compounds such as polymers and small molecules.[2] One of the most significant advantages is their flexibility and ability to be processed using low-cost solution-based techniques, which makes them highly attractive for large-scale manufacturing.[3–5] Additionally, organic semiconductors can be fabricated into ultra-thin films, which can be used to create lightweight and flexible devices which lead to variety of applications. Organic light-emitting diodes (OLEDs) are one of the most widely used applications of organic semiconductors. OLEDs are thin-film devices that emit light when an electric current is passed through them. They have several advantages over traditional light sources, such as incandescent bulbs and fluorescent tubes.[6] OLEDs can be made into thin, flexible, and transparent sheets, making them highly versatile for use in various lighting applications, including displays for smartphones, televisions, and even automotive lighting.[7,8] Organic photovoltaics (OPVs) are another promising application of organic semiconductors. OPVs are solar cells made from organic materials that can convert sunlight into electricity. They offer several advantages over traditional silicon-based solar cells, such as their flexibility, lightweight, and low-cost fabrication.[9–11] OPVs have the potential to revolutionize the renewable energy industry by enabling the creation of highly efficient and low-cost solar cells that can be integrated into a range of products, from semi-transparent building incorporated

solar cells to mobile devices.[12] Organic field-effect transistors (OFETs) have the potential to be used in a range of electronic devices, including digital displays, sensors, and memory storage devices and offer several advantages over traditional inorganic transistors, such as their flexibility, low power consumption, and low-cost fabrication.[13,14]

The function of organic semiconductors in organic electronics is to provide an alternative to traditional inorganic semiconductor materials, such as silicon. Organic semiconductors offer several advantages, such as their ability to be processed at lower temperatures and in solution, which can lead to lower manufacturing costs.[15,16] However, organic semiconductors also present potential challenges. One of the main challenges is their relatively low electrical conductivity compared to inorganic semiconductors, which can limit their performance in certain applications.[17–19] Additionally, organic semiconductors can be sensitive to moisture and oxygen, which can degrade their performance over time.[20,21] Despite these challenges, organic semiconductors also present opportunities for new applications in flexible and wearable electronics, as well as in emerging technologies such as organic spintronics and organic neuromorphic computing.[22–25] There is ongoing research and development to improve the performance and stability of organic semiconductors and to explore new applications for these materials in the field of organic electronics.

I.2 Non-Fullerene Acceptors as n-type materials

In organic photovoltaics (OPVs), n-type materials are used as electron acceptors, while p-type materials are used as electron donors.[26] In traditional OPVs, fullerene derivatives, such as PCBM, have been the dominant n-type materials due to their high electron mobility and good stability. However, in recent years, Non-Fullerene acceptors (NFAs) have emerged as a promising alternative to fullerene derivatives.[26–28]

NFAs have several advantages over fullerene derivatives, such as their tunable energy levels, strong absorption in the visible and near-infrared regions, and ability to form highly efficient bulk heterojunctions with p-type materials. NFAs also have high electron mobility and thermal stability, which are important factors for OPV performance and reliability. In addition to OPVs, NFAs are also being investigated for use in other organic electronics applications, such as organic field-effect transistors (OFETs), organic light-emitting diodes (OLEDs) and organic photodetectors (OPDs).[29–31]

However, there are also some challenges associated with the use of NFAs as n-type materials. One challenge is their relatively low solubility, which can make it difficult to process them into thin films with good morphological control.[32] Additionally, the synthesis of NFAs can be complex and costly.[33] Despite these challenges, NFAs are an active area of research in organic electronics and show great potential for improving the performance and stability of OPVs and other organic electronic devices.

Narrow band gap non-fullerene acceptors (NFAs) are a type of organic semiconductor that have a small difference in energy between their highest occupied molecular orbital (HOMO) and lowest unoccupied molecular orbital (LUMO), which allows them to absorb light in the near-infrared (NIR) region of the spectrum.[34] NFAs are often used as electron acceptors in bulk heterojunction (BHJ) organic solar cells, where they are blended with a conjugated polymer electron donor to form a photoactive layer. In contrast to fullerene-based acceptors, NFAs offer several advantages, including a broad absorption spectrum, tunable energy levels, and better thermal and photostability.[35] Additionally, NFAs can be designed to have high electron mobility, which can improve charge transport and increase device efficiency. Semi-transparent organic solar cells are a type of organic photovoltaic (OPV) device that are designed to allow

some light to pass through the photoactive layer, making them suitable for use in windows, skylights, and other transparent surfaces.[36] To achieve semi-transparency, the photoactive layer must be optimized to absorb light in the visible and NIR regions while maintaining a high degree of transparency in the rest of the spectrum.[37] NFAs are particularly well-suited for use in semi-transparent organic solar cells due to their broad absorption spectra and tunable energy levels.[38]

Near-infrared organic photodetectors (NIR-OPDs) are another application of NFAs in organic electronics. These devices are designed to detect light in the NIR region of the spectrum, which is not visible to the human eye. NIR photodetectors have applications in fields such as remote sensing, security, and medical imaging. NFAs can be used as electron acceptors in NIR photodetectors to improve their sensitivity and responsivity in the NIR region. Additionally, NFAs can be processed using low-cost and eco-friendly solvents, which can reduce manufacturing costs and improve the sustainability of these devices.

Overall, narrow band gap non-fullerene acceptors have shown great promise for use in semi-transparent organic solar cells and near-infrared organic photodetectors, and ongoing research is focused on improving their performance and stability for these and other applications.

I.3 Overview and Objectives

Knowing the definition, advantages, chances and challenges that organic non-fullerene acceptors materials have demonstrated, this thesis is targeting at researching on ultra-narrow bandgaps NFAs molecular design and investigating their resulted changes in materials optoelectronic properties which in return modulating semiconductors' device performance. While the mainstream of research efforts have been spent on raising up in the record number

of power conversion efficiency (PCE) for organic photovoltaics systems, this work will further exploring more possibilities of ultra-narrow bandgap NFAs promising potentials in highly efficient green solvent processible systems and semi-transparent devices. The first two chapters of this thesis introduce the molecular engineering of narrow bandgap NFAs based on the original structure of published near-infrared absorber COTIC-4F molecule. The impact of side chain modification on the optoelectronic properties of NFAs built on the COTIC-4F conjugated framework has been examined and tested within the applications of corresponding organic solar cells and NIR-OPDs. Via modification on the center donor core, a set of C-O bridged NFAs CO6ICs have been successfully synthesized and applied into NIR-OPDs achieving high responsivity at NIR-region. Moreover, those set of small molecular NFAs have presented promising processibility in "green solvent" of 2-MeTHF. This leads to the following chapter of this thesis presenting a project investigating molecular engineering of green solvent processable A-D'-D-D'-A structured non-fullerene acceptors (NFAs). These NFAs exhibit high solubilities and potential processability in 2-MeTHF. By using DFT and HSP simulation of the small molecules, and various thin-film characterization techniques (UV-vis, AFM, GIWAXS) on the 2-MeTHF solvent-cast thin-films, a better understanding of the materials' chemical structural influences on NFAs' green solvent processibilities and their corresponding solid-state properties is achieved.

The last chapter of this contribution focus on the molecular design and synthesis of a series of ultra-narrow bandgap NFAs and their efficient NIR-OPDs applications processed from non-halogenated solvent of toluene. Systematic modifications on the end-dye acceptor halogen substituents within the framework were made to investigate the influence of the electron negativity of terminated groups on the materials' optical properties and the corresponding

device performance. Semitransparent organic optoelectronic devices were fabricated with the originally designed NFAs and processed using chlorobenzene and toluene as non-halogenated solvents for comparison. Toluene-based devices achieved higher specific detectivity due to the better quality of blend thin-film morphologies and more compacted crystallinity in the photoactive layer. This confirms that this novel series of DaTICs NFAs have satisfying chlorine-free solvent processibilities without sacrificing device performance.

Chapter 1: Molecular Engineering for Non-Fullerene Acceptors

1.1 Introduction

Organic semiconductors are of intense interest due to their ability to be processed into ultra-thin, flexible, and conformal products through low-cost solution based techniques;[39,40] moreover, their structural versatility allows tuning of optical gaps for specific applications.[41–43] Near-infrared (NIR) responsive organic solar cells (OSCs) may form the basis of future applications such as semitransparent energy producing modules for building-integrated or green house systems.[37,44] With a similar working principle to OSCs, organic photodetectors (OPDs) with NIR responsivity are of relevance to applications that include image sensing, night surveillance, optical communication, and health monitoring.[18,45,46] Considering that the spectral response window of organic semiconductors can be readily tuned by rational molecular design, NIR OPDs have emerged as potentially cost-effective material choices. This flexibility in molecular design can be coupled with extensive know-how of the function, mechanisms and morphological features of bulk heterojunction (BHJ) thin films in order to accelerate the development of NIR OPDs.[47–50]

Narrow bandgap (NBG) non-fullerene acceptors (NFAs) are an emerging class of NIR absorbers that outperform fullerenes in BHJ photodiodes.[51,52] Of note is how their structural flexibility can be used to modulate energy levels and to tailor absorption characteristics toward NIR light.[26,35,53,54] These opportunities are noteworthy given that the vast majority of OPD systems reported to date comprise fullerenes with a NBG donor material that manages the absorption range of the device.[45,46,55,56] However, the main disadvantage of such devices is their relatively low photoresponsivity in the NIR region compared to commercially available inorganic devices.

1.2 Molecular design and synthesis of A-π-D-π-A NFAs

Our group have reported an ultra-NBG NFA, namely COTIC-4F, with an optical bandgap (E_g) of ~1.10 eV.[57] As shown in **Figure 1-1**, the general design strategy of COTIC-4F family of ultra-narrow bandgap NFAs can be summarized as a A−D'−D−D'−A molecular configuration based on an electron rich core comprised of cyclopentadithiophene (CPDT) as the central donor (D) unit and alkoxythienyl units as the flanking donor (D') fragments, followed by capping with the 2-(5,6-difluoro-3-oxo-2,3-dihydro-1H-inden-1-ylidene)malononitrile (IC-2F) end-dye acceptor (A) units. Of note are the responses to NIR light of the BHJ OSCs based on COTIC-4F and PTB7-Th, specifically the high short-circuit current density (J_{SC}) of over 20 mA·cm^{-2} and the low photon energy loss (~ 0.52 eV). These features encouraged us to optimize the device efficiencies of photodiodes by molecular engineering to fine-tune the electronic energy diagram and NIR absorption capabilities. A few strategies can be employed to modulate the intramolecular charge transfer (ICT) and E_g characteristics through structural modification.[42,58,59] One simple way is by introducing different electron-donating side chains such as alkyl, alkoxy, alkylthio or alkylamino groups.[60–64] Another efficient method incorporated in order to modify organic semiconductors absorbing wavelength window is researching on halogen atom substituents on the end-dye acceptors unit.[65,66]

In this contribution, we examine the impact of side chain modification on the optoelectronic properties of NFAs built on the COTIC-4F conjugated framework (**Figure 1a**). Starting with COTIC-4F (A−D'−D−D'−A), we examine CTIC-4F (A−D"−D−D"−A, D" = alkylthienyl) and CO1-4F (A−D'−D−D"−A). Our molecular design rationale is as follows. First, introduction of different side chains, such as alkyl or alkoxy groups, can readily change ICT characteristics of our molecules due to their relative electron-donating strengths.[63,62] By increasing the number of alkoxy groups, we find that one can achieve a smooth progression of E_g and molecular orbital

characteristics that translate into OPDs tailored to match specific spectral responses. Secondly, CPDT as the central donor and IC-2F as the outer acceptor unit have strong electron-donating and electron-withdrawing properties, respectively, resulting in intramolecular charge transfer and optical absorbance in the NIR region (700 nm - 1100 nm).

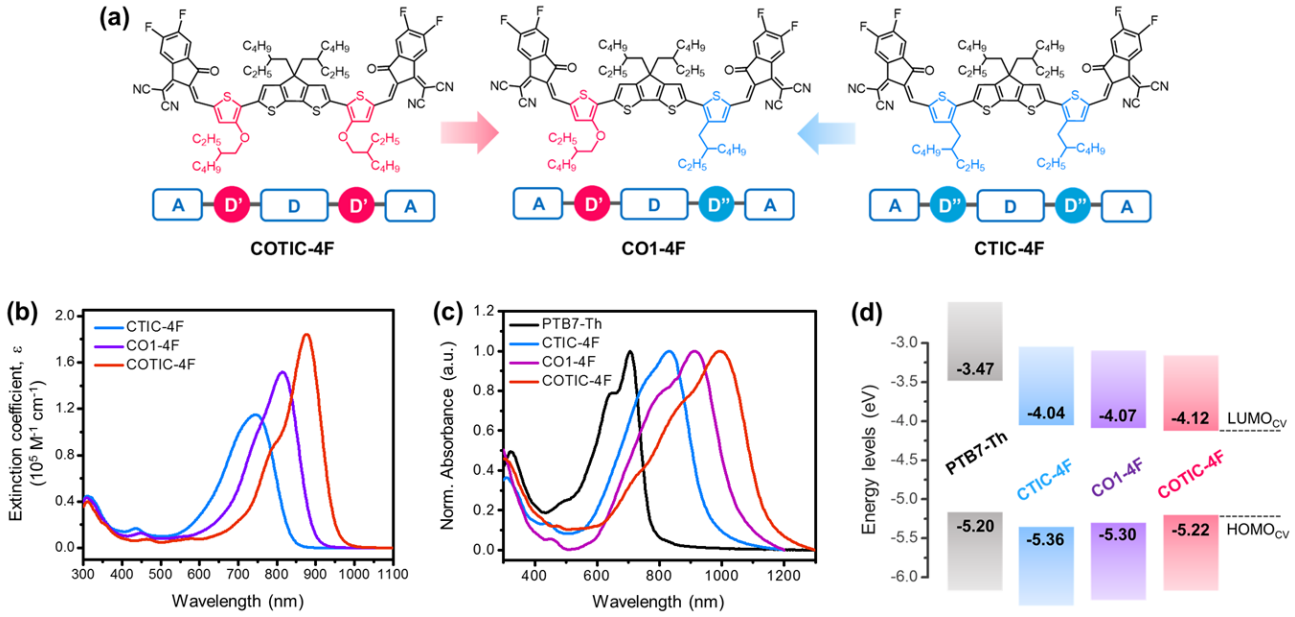

Figure 1-1. (a) Chemical structures of CTIC-4F, CO1-4F, and COTIC-4F. Absorption spectra of (b) solution and (c) thin film. (d) Energy level diagram of active layer components estimated from thin film CV measurements.

Synthetic routes for the new NFAs are depicted in **Figure 1-2**. The symmetric molecule CTIC-4F was synthesized through Stille coupling of compound **2** and 5-bromo-4-(2-ethylhexyl)thiophene-2-carbaldehyde (**3**) in the presence of $Pd(PPh_3)_4$ in anhydrous toluene, followed by Knoevenagel condensation with IC-2F (**5**) in the presence of pyridine in chloroform, yielding CTIC-4F. Stille coupling between (4,4-bis(2-ethylhexyl)-4H-cyclopenta[1,2-b:5,4-b']dithiophen-2-yl)trimethylstannane (**6**) and compound **3** produced monoaldehyde **7**. C-H activated direct arylation of compound **7** and compound **8** produced the key asymmetric

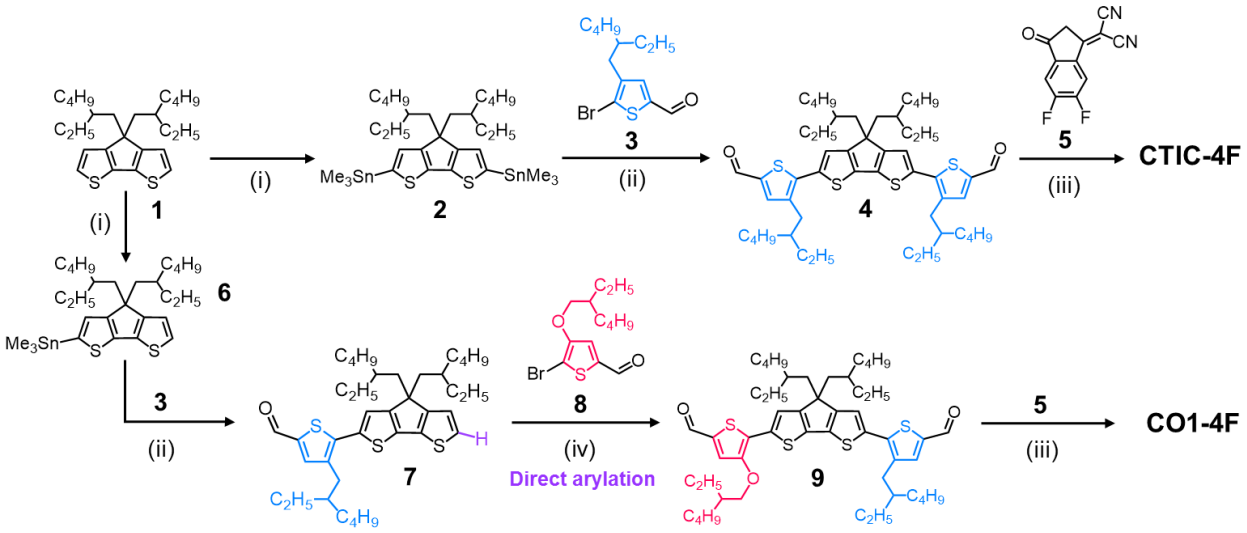

Figure 1-2. Synthetic procedures for CTIC-4F and CO1-4F. (i) n-BuLi, THF, Me_3SnCl, -78 ºC; (ii) $Pd(PPh_3)_4$, Toluene:DMF, 110 ºC; (iii) Chloroform, pyridine, 60 ºC; (iv) $Pd(OAc)_2$, $P^tBu_2Me{\cdot}HBF4$, DMF, K_2CO_3, PivOH, $P^tBu_2Me{\cdot}HBF_4$.

intermediate **9**, followed by Knoevenagel condensation with **7** to obtain the target CO1-4F. The new compounds were characterized by spectroscopic methods and exhibit good solubility in common organic solvents such as dichloromethane, chloroform (CF) and chlorobenzene (CB) at room temperature.

1.3 Results and Discussions

Absorption spectra of solutions of NFAs are shown in **Figure 1-1**. As the number of oxygen atoms in the NFA increases, the absorption maximum (λ_{max}) in CF shifts gradually from 744 nm to 814 nm then 875 nm, accompanied by increasing maximum molar extinction coefficients. The absorbance of the three NFAs red-shifts significantly (~ 100 nm) between the solution and thin film states, as seen in **Figure 1-1c**. Optical transitions of NFAs are located in the NIR region with E_g^{opt} of 1.30 eV, 1.18 eV, and 1.08 eV for CTIC-4F, CO1-4F, and COTIC-4F, respectively. As a result, the absorption edge of the CO1-4F occurs between those of CTIC-4F and COTIC-4F. Using cyclic voltammetry (CV) measurements, the highest occupied molecular orbital (HOMO) and

lowest unoccupied molecular orbital (LUMO) levels were deduced from the onsets of oxidation and reduction, respectively. The HOMO/LUMO energy levels of CTIC-4F, CO1-4F, and COTIC-4F were determined to be −5.36/−4.04, −5.30/−4.07, and −5.22/−4.12 eV, respectively (**Figure 1-1d**). Incorporation of alkoxy side chains into the π-bridging thienyl unit increases the density of π-electrons (D'−D−D' > D'−D−D" > D"−D−D") on the conjugated backbone and thus gradually upshifts the HOMO energy levels of the molecules.[51,62] Our previous study revealed that PTB7-Th:COTIC-4F-based solar cells generate large photocurrents in the NIR despite a very small HOMO−HOMO energetic offset between PTB7-Th and COTIC-4F. Since CTIC-4F and CO1-4F possess lower HOMO energy levels relative to COTIC-4F, it is anticipated that both NIR-absorbing NFAs will efficiently generate charge when blended with PTB7-Th.

Table 1. Optical and electrochemical properties of CTIC-4F, CO1-4F, and COTIC-4F.

compound	$\lambda_{s,max}$ (nm)[a]	$\lambda_{f,max}$ (nm)[b]	E_g^{opt} (eV)[c]	HOMO (eV)[d]	LUMO (eV)[e]	E_g^{CV} (eV)[f]
CTIC-4F	744	830	1.30	−5.36	−4.04	1.32
CO1-4F	814	920	1.18	−5.30	−4.07	1.23
COTIC-4F	875	995	1.08	−5.22	−4.12	1.10

[a]Absorption maximum in solution. [b]Absorption maximum in thin film. [c]Optical bandgap calculated from the absorption edge of the thin film. [d]HOMO energy level estimated from the oxidation onset potential. [e]LUMO energy level estimated from the potential of the reduction onset. [f]HOMO−LUMO gap estimated from cyclic voltammetry.

Solar cells with the architecture ITO/ZnO/PTB7-Th:NFA/MoO_3/Ag were fabricated in order to test the performance of COTIC-4F, CTIC-4F and CO1-4F. Optimal photovoltaic performances were obtained with a blend ratio of PTB7-Th:NFA of 1:1.5 (wt%) using CB as the solvent and 1-chloronaphthalene (CN) as the processing additive. **Figure 1-3a** and **Table 2** show the *J-V* characteristics and a summary of device parameters, respectively. Devices with CTIC-4F, CO1-4F, and COTIC-4F show PCEs of 10.50%, 10.24% and 7.34% with open-circuit (V_{OC}) values of 0.70 V, 0.64V, and 0.57 V, respectively. These V_{OC} values are in good agreement with expectations from the LUMO

energy level difference. Remarkable values for J_{SC} of 23.36 mA·cm^{-2}, 24.80 mA·cm^{-2}, and 20.4 mA·cm^{-2} were obtained for devices with CTIC-4F, CO1-4F, and COTIC-4F, respectively, which are relevant to high external quantum efficiency (EQE) responses in the NIR region. These J_{SC} values match well with values calculated from EQE measurements, as shown in **Figure 1-3b** and **Table 2**.

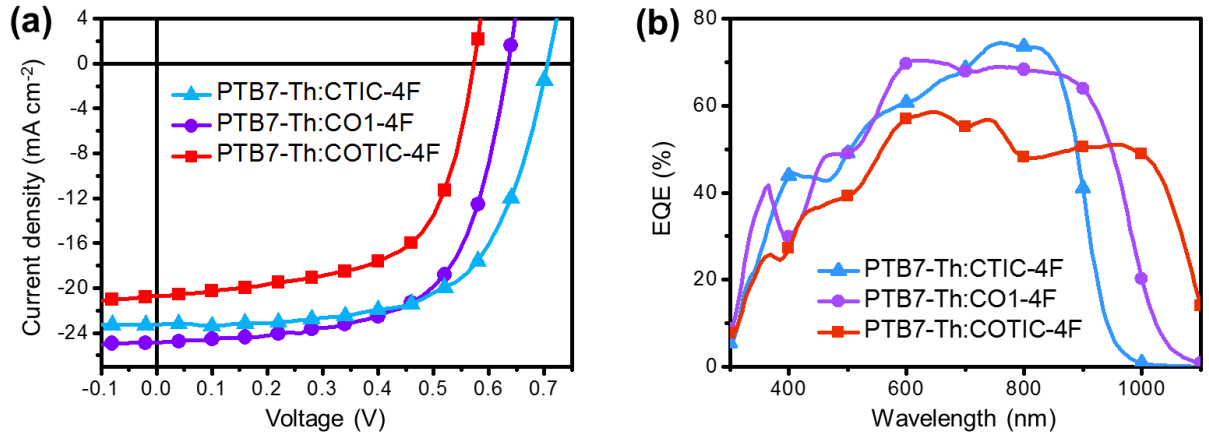

Figure 1-3. (a) *J*−*V* characteristics and (b) EQE spectra of the optimized OSC devices under AM 1.5 G illumination at 100 mW cm^{-2}. (c) J_{ph} versus V_{eff} characteristics, and (d) J_{sc} versus light intensity of the optimized devices.

Table 2. Photovoltaic performances of the OSC devices based on PTB7-Th and three acceptors measured at simulated 100 mW cm^{-2} AM 1.5G illumination.

Acceptor[a]	V_{OC} (V)	J_{SC} (mA cm^{-2})	FF	PCE$_{max}$ (%)[b]	Cal. J_{SC} (mA cm^{-2})
CTIC-4F	0.70 (0.70±0.002)	23.36 (22.90±0.55)	0.64 (0.62±0.02)	10.50 (9.99±0.37)	22.6
CO1-4F	0.64 (0.63±0.006)	24.80 (24.97±0.42)	0.64 (0.63±0.01)	10.24 (9.99±0.27)	24.0
COTIC-4F	0.57 (0.56±0.010)	20.73 (20.92±0.51)	0.61 (0.58±0.02)	7.34 (6.90±0.28)	20.4

[a]PTB7-Th:acceptor blend ratios are 1:1.5 (w/w). 2vol% CN was used as a processing solvent additive. [c]Average values from 18 devices.

In view of the performance of PTB7-Th:NFA blends within in solar cell configurations, we examine their function within NIR organic photodetectors. Responsivity (*R*), the ratio of the photocurrent to the incident light intensity, is an important parameter to evaluate the optical

response of a photodetector. It is calculated from the EQE according to the following equation:[55]

$$R = \frac{J_{ph}}{I_{light}} = \frac{EQE\ \lambda}{1240}$$

where J_{ph} is the photocurrent density in $A \cdot cm^{-2}$, I_{light} is the incident light intensity in $W \cdot cm^{-2}$, λ is the wavelength. **Figure 1-4(a-c)** shows the spectral responsivity of BHJ photodiodes based on CTIC-4F, CO1-4F and COTIC-4F, respectively. Maximum responsivities under short-circuit conditions of 0.49 A/W, 0.46 A/W and 0.37 A/W were determined at 830 nm, 920 nm, and 995 nm for devices with CTIC-4F, CO1-4F and COTIC-4F, respectively. When operated under reverse bias, photodetector responsivity increases as a result of more efficient charge collection under an external electric field. PTB7-Th:CO1-4F devices have a responsivity of 0.52 A/W under an applied bias of -3 V. To the best of our knowledge, this is the highest reported organic photodetector responsivity in the 900 nm range without a gain mechanism. Another critical figure of merit for photodetectors is the specific detectivity (*D**), which evaluates the sensitivity to weak optical signals. The shot noise-limited specific detectivity can be calculated from the responsivity and dark *J-V* characteristics.[67] The *D** of the three types of photodetectors is shown in Figure 3d-3f. At 0 V, specific detectivities of 7.0×10^{11}, 1.5×10^{12} and 1.7×10^{11} Jones are obtained for CTIC-4F, CO1-4F and COTIC-4F based devices. As the reverse bias increases, *D** decreases for all three NFAs based photodetectors. At – 3 V, the corresponding values are 1.2×10^{10}, 2.6×10^{10} and 5.9×10^{9} jones, respectively. Thus, while increasing the reverse bias can enhance the responsivity, the dramatic increase in the dark current, along with the shot noise that accompanies it, has a negative dominating effect on the specific detectivity. This suggests the limiting factor of detectivity is mainly the dark current. Engineering of the interface should minimize the dark current under reverse bias, resulting in larger *D**.

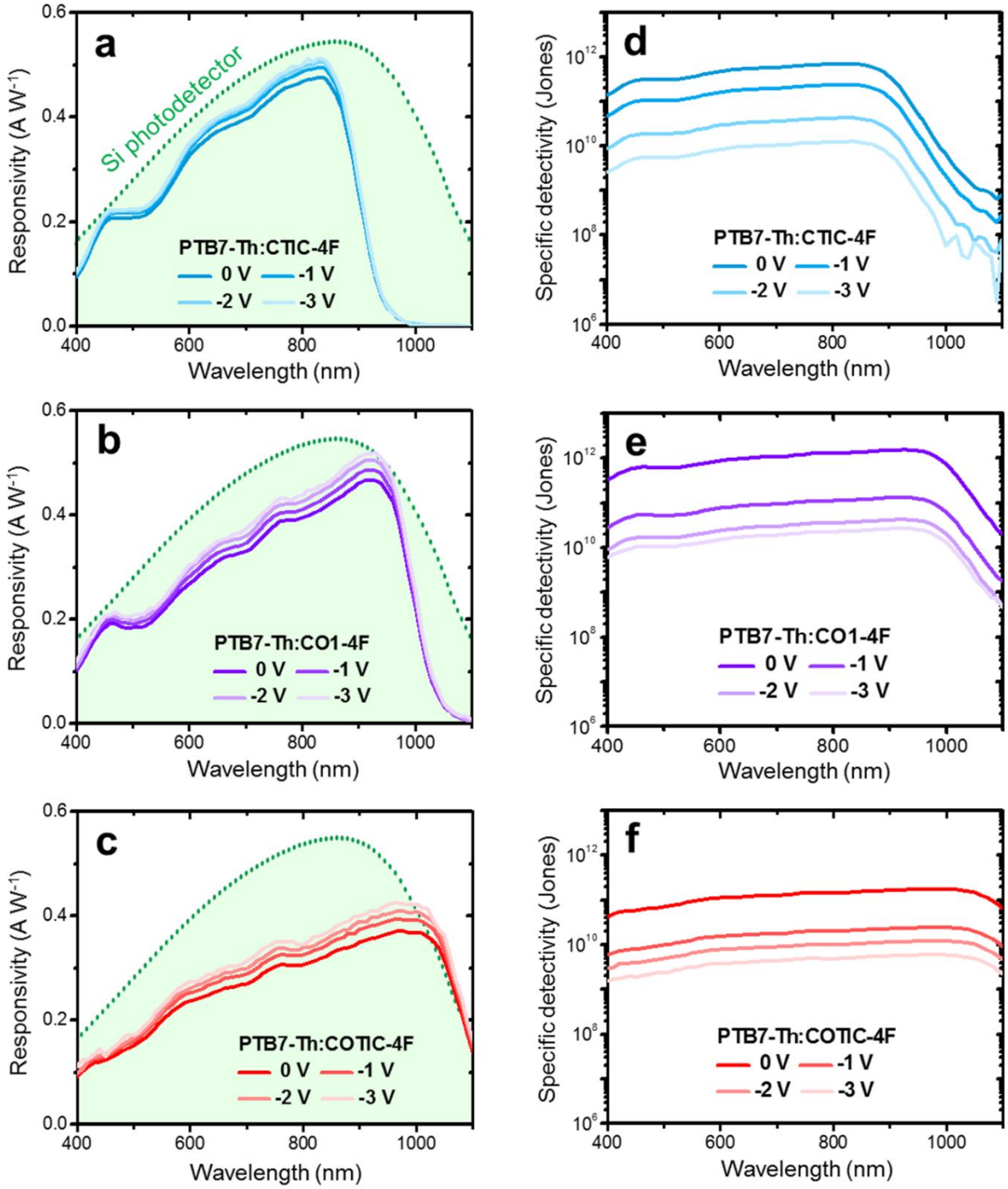

Figure 1-4. (a-c) Responsivity and (d-f) specific detectivity of photodetector devices using PTB7-Th:NFA blends.

How side chain modification of π-bridge impacts molecular order within pure NFA and blend films was investigated by using grazing incidence wide-angle X-ray scattering (GIWAXS). Two-dimensional (2D) GIWAXS patterns of neat and blend films processed with under the same conditions as the optimized OSC devices are shown in **Figure 1-5**. To investigate how processing additives affect the blend components, we compared neat films prepared with and without CN additive. Examination of the results shows that with CN dramatically changes the manner of molecular packing of CTIC-4F in the neat film. The CN-processed CTIC-4F film shows a sharp and intense (100) diffraction peak at q_z = 0.50 Å^{-1} (*d*-spacing: 12.5 Å), as well as an abundance of diffraction spots which cannot be attributed to specific features at this time. These features imply that CTIC-4F molecules have a tendency to crystallize in ordered 3D structures with the complicated diffraction pattern suggesting the presence of multiple polymorphs.[68,69] Replacing D" with the D' π-bridge results in diffraction along the q_z and q_{xy} axes, but few off-axis scattering features. CO1-4F shows a typical edge-on orientation with a strong (100) diffraction peak at q_z = 0.41 Å^{-1} (*d*-spacing: 15.3 Å), noticeably larger than for CTIC-4F, and a π–π stacking peak at q_{xy} = 1.79 Å^{-1} (*d*-spacing: 3.51 Å) whereas COTIC-4F tends to adopt a bimodal texture with a coexistence of face-on and edge-on orientations. The molecular ordering of PTB7-Th within a neat film show a preferential face-on orientation. The 2D GIWAXS diffraction pattern of the PTB7-Th:CTIC-4F blend (Figure 4d) maintains scattering features from both neat materials, suggesting that one component does not perturb crystallization of the other.[51,70] Although the well-defined diffraction spots of CTIC-4F are lost in the blend with PTB7-Th, many remain, albeit with increased orientational disorder.

The diffraction patterns of blends of PTB7-Th:COTIC-4F (**Figure 1-5e**) and PTB7-Th:CO1-4F (**Figure 1-5f**) display broad lamellar (100) packing in the in-plane direction and broad π-π (010)

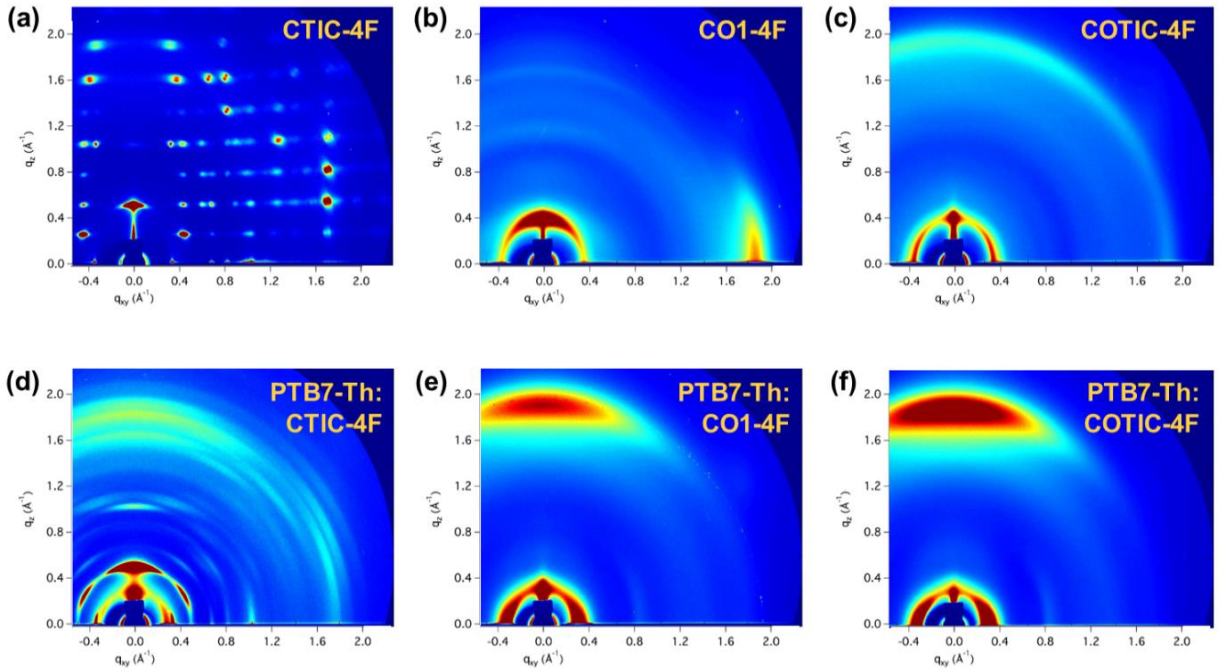

Figure 1-5. 2D GIWAXS images of (a) CTIC-4F, (b) CO1-4F, and (c) COTIC-4F neat films, and (d) PTB7-Th:CTIC-4F, (e) PTB7-Th:CO1-4F, and (f) PTB7-Th:COTIC-4F blend films processed with CB:CN (98:2 vol%).

packing in the out-of-plane direction. We suspect that the diffraction features originate from the PTB7-Th and NFA crystals, as well as part of the components being reorganized into intermixed phases. One observes PTB7-Th is relatively insensitive to the blending with NFA component and orients face-on relative to the substrate as seen in the neat film. However, orientation of the NFA crystallites in the blend is sensitive to the presence of PTB7-Th. As mentioned above, the high degree of intracrystalline and orientational order observed for neat CTIC-4F is disturbed upon blending with PTB7-Th, while crystallites of COTIC-4F adopt a face-on orientation in contrast to the previous edge-on orientation in the neat COTIC-4F film. During spin-coating with PTB7-Th, COTIC-4F crystallites may be kinetically trapped in a metastable face-on state,[71] favorable to out-of-plane charge transport necessary in diodes. A similar result is observed when blending CO1-4F with PTB7-Th, although it is difficult to draw similar conclusions due to the disorder observed in the GIWAXS diffraction pattern of neat CO1-4F.

1.4 Conclusions

In summary, we successfully synthesized NFAs that have narrow optical bandgaps, absorbing in the 700 – 1100 nm range. The subtle structural modification of NFAs via side chain engineering led to a dramatic change in the spectral window of devices when incorporated in OSCs and OPDs. Newly designed NFAs, CTIC-4F and CO1-4F, showed decent photovoltaic properties with PCEs over 10% and remarkable J_{SC} of ~25 mA·cm^{-2}. The efficient OPDs were demonstrated by using new materials and the devices feature high responsivities of 0.51 A W^{-1} at 830 nm and 0.52 A W^{-1} at 920 nm for CTIC-4F and CO1-4F, respectively. Notably, CO1-4F is one of the very few electron acceptor materials featuring narrow bandgap (<1.3 eV) and high photo-responses to the NIR. With consideration of wide range of possible structural modifications, this design strategy suggests that a wide range of additional NFAs can be further designed with the simplicity of preparation.

1.5 Experimental Methods

Materials All reagents and chemicals were purchased from commercial sources and used without further purification. All anhydrous organic solvents for the synthesis, characterization, and device fabrication steps were purchased from Sigma-Aldrich and TCI. Compound 1, 2, 3, 4, 5, 7, and 8 were prepared *via* a modified synthetic condition from literature.[52,57,62,72]

Characterizations of compounds ^{1}H and ^{13}C NMR spectra of intermediate monomers were recorded on a Varian Unity Inova 500 MHz spectrometer in deuterated chloroform solution ($CDCl_3$) with 0.003%TMS as internal reference. Mass spectra were obtained from Bruker Microflex Matrix-Assisted LASER Desorption Ionization - Time of Flight Mass Spectrometer (MALDI-TOF) using 1,8-Dihydroxy-9(10H)-anthracenone (Dithranol) as a matrix recorded in a (+)-reflector mode. Ultraviolet-Visible-Near-infrared (UV-Vis-NIR) absorption spectra were

recorded on a Perkin Elmer Lambda 750 spectrophotometer. For the measurements of thin films, materials were spun coated onto precleaned glass substrates from chloroform solutions (10 mg mL^{-1}). Optical band gap (Eg^{opt}) was determined from the absorption onset of thin film sample.

Electrochemical characterization The electrochemical cyclic voltammetry (CV) was conducted on a CHI-730B electrochemistry workstation with glassy carbon disk, Pt wire, and Ag/Ag+ electrode as the working electrode, counter electrode, and reference electrode, respectively in a 0.1 M tetrabutylammonium hexafluorophosphate (n-Bu_4NPF_6)-anhydrous acetonitrile solution at a potential scan rate of 50 mV s^{-1}. Thin films of samples were deposited onto the glassy carbon working electrode from a 1.5 mg mL^{-1} chloroform solution. The electrochemical onsets were determined at the position where the current starts to differ from the baseline. The potential of Ag/AgCl reference electrode was internally calibrated by using the ferrocene/ferrocenium redox couple (Fc/Fc^+).

Grazing incidence wide angle X-ray scattering (GIWAXS) analysis 2D GIWAXS measurements were performed using Beamline 9A at the Pohang Accelerator Laboratory (PAL). The photon energy is 11.055 keV (λ = 1.1214 Å). The angle between the film surface and the incident beam was fixed at 0.12° for all of the samples. The measurements were obtained at scanning intervals of 2θ between 3° and 25°. The 2D GIWAXS images from the films were analyzed according to the relationship between the scattering vector q and the d spacing, $q = 2\pi/d$. The GIWAXS images shown are normalized with respect to exposure time.

Fabrication and characterization of solar cell and photodetector devices The solar cell devices were fabricated followed by these procedures. First, the ITO-coated glass substrates were cleaned with detergents, then sonicated in acetone and isopropyl alcohol and dried in an

oven at 130 °C. The zinc oxide (ZnO) solution was prepared using mixture of diethyl zinc and tetrahydrofuran (THF) (1:2, v/v %) and the ZnO film (35 nm) was prepared from spin-casting at 4000 rpm for 15 s and annealing at 110 °C for 15 min.[4,5] For deposition of the active layer, blend solutions of PTB7-Th (1 wt%):NFAs (1.5 wt%) dissolved in CB (with 2 vol% 1-chloronaphthalene) were spin-coated on top of the ZnO layer in a nitrogen-filled glove box. The device was pumped down in vacuum (< 10–6 torr; 1 torr ~133Pa), and a 7 nm thick MoO_3/100 nm thick Ag electrode for our device architecture were deposited on top of the active layer by thermal evaporation. The photodetector devices were fabricated similar to the solar cell devices with the only exception that another shadow mask was used during thermal evaporation to yield a smaller device area of ~4.51 mm^2. The deposited MoO_3/Ag electrode defined the active area as 20 mm^2. Photovoltaic characteristics measurements were carried out inside the glove box using a high quality optical fiber to guide the light from the solar simulator equipped with a Keithley 2635A source measurement unit. *J-V* curves were measured under AM 1.5G illumination at 100 mW cm^{-2} using an aperture (9.4 mm^2) to define the illuminated area. EQE measurements were conducted in nitrogen-filled glove box using an EQE system. The monochromatic light intensity was calibrated using a Si photodiode and chopped at 100 Hz.

1.6 Material Synthesis

5,5'-(4,4-bis(2-ethylhexyl)-4H-cyclopenta[1,2-b:5,4-b']dithiophene-2,6-diyl)bis(4-(2-ethylhexyl)thiophene-2-carbaldehyde) (compound 4): A mixture of 4,4-bis(2-ethylhexyl)-4H-cyclopenta[1,2-b:5,4-b']dithiophene-2,6-diyl)bis(trimethylstannane), compound 2, (900 mg, 1.24 mmol), 5-bromo-4-(2-ethylhexyl)thiophene-2-carbaldehyde, compound 3, (937 mg,

3.09 mmol), ($Pd(PPh_3)_4$) (71 mg), and dry toluene (20 mL) was added into a flame-dried and nitrogen-filled one-neck round-bottom flask (50 mL). The flask was purged with N_2 for 10 min and the reactant was heated to 120 °C for 36 h. After the mixture cooled to room temperature, DI water was added, and the mixture was extracted with dichloromethane two times (50 ml×3). The organic layer was dried over $MgSO_4$ and concentrated in vacuum. The residue was purified by silica gel column chromatography (*n*-hexane/ethyl acetate, 1/9) to afford the product as a sticky red solid (754 mg, 72%).

^{1}H NMR (500MHz, CDCl3, ppm): δ 9.83 (s, 2H), 7.56 (s, 2H), 7.16 (t, 2H), 2.77 (d, 4H), 1.89–1.98 (m, 4H), 1.71 (br, 2H), 1.25 – 1.30 (m, 16H), 0.84 – 1.05 (m, 28H), 0.60 – 0.74 (m, 12H).

2,2'-((2Z,2'Z)-((5,5'-(4,4-bis(2-ethylhexyl)-4H-cyclopenta[1,2-b:5,4-b']dithiophene-2,6-diyl)bis(4-(2-ethylhexyl)thiophene-5,2-diyl))bis(methanylylidene))bis(5,6-difluoro-3-oxo-2,3-dihydro-1H-indene-2,1-diylidene))dimalononitrile (CTIC-4F): A mixture of compound 4 (384 mg, 0.45 mmol) and 2-(5,6-difluoro-3-oxo-2,3-dihydro-1H-inden-1-ylidene)malononitrile, compound 5, (334 mg, 1.45 mmol), dry chloroform (20 mL), and pyridine (0.5 mL) was added into to a flame-dried and nitrogen-filled one-neck round-bottom flask (50 mL). The flask was purged with N2 for 20 min and the reactant was heated to 60 ℃ for 16 h. After the mixture cooled to room temperature, the reaction mixture was concentrated in vacuum. The residue was purified by silica gel column chromatography (*n*-hexane/dichloromethane, 2/8) to afford the product as a dark brown solid (443 mg, 76%).

^{1}H NMR (500MHz, CDCl3, ppm): δ 8.77 (s, 2H), 8.53 (q, 2H), 7.69 (t, 2H), 7.64 (s, 2H), 7.48 (t, 2H), 2.84 (d, 4H), 1.94 – 2.05 (m, 4H), 1.78 (br, 2H), 1.23 – 1.46 (m, 16H), 0.85 – 1.15 (m, 28H), 0.63 – 0.70 (m, 12H).

MS (MALDI-TOF): calculated *m/z* 1271.70; found *m/z* 1271.46.

5-(4,4-bis(2-ethylhexyl)-4H-cyclopenta[1,2-b:5,4-b']dithiophen-2-yl)-4-(2-ethylhexyl)thiophene-2-carbaldehyde (compound 7): A mixture of compound 6 (565.5 mg, 1 mmol), compound 3 (394 mg, 1.3 mmol), ($Pd(PPh_3)_4$) (58 mg), and dry toluene (20 mL) was added into to a flame-dried and nitrogen-filled one-neck round-bottom flask (50 mL). The flask was purged with N_2 for 20 min and the reactant was heated to 120 °C for 36 h. After the mixture cooled to room temperature, DI water was added, and the mixture was extracted with dichloromethane for two times (50 ml×3). The organic layer was dried over $MgSO_4$ and concentrated in vacuum. The residue was purified by silica gel column chromatography (*n*-hexane/ethyl acetate, 1/9) to afford the product as a sticky orange solid (525 mg, 84%).

^1H NMR (500MHz, $CDCl_3$, ppm): δ 9.82 (s, 1H), 7.55 (s, 1H), 7.21 (d, 1H), 7.14 (t, 1H), 6.95 (m, 1H), 2.77 (d, 2H), 1.84 – 1.96 (m, 4H), 1.71 (br, 2H), 1.21 – 1.40 (m, 10H), 0.83 – 1.05 (m, 22H), 0.57 – 0.78 (m, 12H)

5-(4,4-bis(2-ethylhexyl)-6-(3-((2-ethylhexyl)oxy)-5-formylthiophen-2-yl)-4H-cyclopenta[1,2-b:5,4-b']dithiophen-2-yl)-4-(2-ethylhexyl)thiophene-2-carbaldehyde (compound 9): A mixture of compound 7 (250 mg, 0.4 mmol), compound 8 (147 mg, 0.46 mmol), $Pd(OAc)_2$ (10.8 mg, 0.05 mmol), $P^tBu_2Me{\cdot}HBF_4$ (19.8 mg, 0.08 mmol), pivalic acid (40.8 mg, 0.4 mmol), potassium carbonate (165.8 mg, 1.2 mmol), and dry toluene (4 mL) was added into to a flame-dried and nitrogen-filled one-neck round-bottom flask (25 mL). The resulting mixture was purged with N_2 for 20 min and was heated to 120 °C for 16 h. After TLC analysis showed completion of the reaction, the resulting mixture was cooled to room temperature. DI water was added and the mixture was extracted with dichloromethane for two times (50 ml×3). The organic layer was dried over $MgSO_4$ and concentrated in vacuum. The

residue was purified by silica gel column chromatography (*n*-hexane/ethyl acetate, 1/9) to afford the product as a sticky orange solid (210 mg, 72%).

^{1}H NMR (500MHz, $CDCl_3$, ppm): δ 9.82 (s, 1H), 9.75 (s, 1H), 7.56 (s, 1H), 7.47 (s, 1H), 7.32 (s, 1H), 7.15 (t, 1H), 4.10 (d, 2H), 2.77 (d, 2H), 1.81 – 1.97 (m, 5H), 1.72 (br, 1H), 1.18 – 1.66 (m, 18H), 0.80 – 1.10 (m, 28H), 0.59 – 0.75 (m, 12H).

2-((Z)-2-((5-(6-(5-((Z)-(1-(dicyanomethylene)-5,6-difluoro-3-oxo-1H-inden-2(3H)-ylidene)methyl)-3-((2-ethylhexyl)oxy)thiophen-2-yl)-4,4-bis(2-ethylhexyl)-4H-cyclopenta[1,2-b:5,4-b']dithiophen-2-yl)-4-(2-ethylhexyl)thiophen-2-yl)methylene)-5,6-difluoro-3-oxo-2,3-dihydro-1H-inden-1-ylidene)malononitrile (CO1-4F): A mixture of compound 9 (389 mg, 0.45 mmol) and 2-(5,6-difluoro-3-oxo-2,3-dihydro-1H-inden-1-ylidene)malononitrile, compound 5, (334 mg, 1.45 mmol), dry chloroform (20 mL), and pyridine (0.5 mL) was added into to a flame-dried and nitrogen-filled one-neck round-bottom flask (50 mL). The flask was purged with N_2 for 20 min and the reactant was heated to 60 °C for 5 h. After the mixture cooled to room temperature, the reaction mixture was concentrated in vacuum. The residue was purified by silica gel column chromatography (*n*- hexane/dichloromethane, 2/8) to afford the product as a dark green solid (400 mg, 69%).

^{1}H NMR (500MHz, $CDCl_3$, ppm): δ 8.77 (s, 1H), 8.70 (s, 1H), 8.49 – 8.56 (m, 2H), 7.61 – 7.72 (m, 4H), 7.44 – 7.53 (m, 2H), 4.17 (d, 2H), 2.85 (d, 2H), 1.94 – 2.05 (m, 4H), 1.87 – 1.94 (m, 1H), 1.79 (br, 1H), 1.50 – 1.70 (m, 4H), 1.23 – 1.46 (m, 14H), 0.85 – 1.15 (m, 28H), 0.63 – 0.70 (m, 12H).

MS (MALDI-TOF): calculated *m/z* 1287.70; found *m/z* 1287.57.

Chapter 2: Materials Development for Ultra-Narrow Bandgap Non-Fullerene Acceptors (UNBG-NFAs)

2.1 Introduction

The active materials in organic optoelectronic devices have rapidly developed to achieve high performance as well as to obtain high-transmittance for next-generation integrating application.[57,73–75] In particular, non-fullerene acceptors (NFAs) with the capability to absorb until near-infrared wavelength region have received considerable attention, recently, due to their promising potential of various applications in thin-film-transistors, organic solar cells, sensors, and etc. Furthermore, the optical absorption range of NFAs can be selectively tuned by adjusting the bandgap of the materials.[76–79] Considerable research has been dedicated to the investigation of high-performance Semi-Transparent Organic Photovoltaics (ST-OPV). Particularly, there is significant interest and need in developing ultra-narrow band gap materials with superior absorbing selectivity, as these have potentially absorbing selectivity in infrared region detecting beyond the detective limits of traditional opaque Si-based inorganic NIR-OPDs as well as improving important evaluation parameter of average visible transmittance (AVT) of ST-OPV devices.[79–81] Uses of transparent light sensors will be for the Internet-of-Things (IoT) generation such as vehicle windows, building smart exteriors, e-skin, wearable health devices and etc.[26,82] This section describes our approach to designing ultra-narrow bandgap non-fullerene acceptors using molecular design strategies inspired by the worked summarized in the first chapter with the aid of theoretical simulation. A pair of A−D−D'−D−A structured ultra-narrow bandgap NFAs with optical bandgap within 1.0eV (BCIC-4F and TCIC-4F) have been designed, synthesized, and fabricated into photodetectors.

Photodetectors are an essential component in electronic devices that are used for a wide range of applications, including image sensors, health monitoring devices, solar cells and so on. Conventional photodetectors are based on crystalline inorganic semiconductor materials such as silicon and epitaxial semiconductors grown on planar and rigid substrates (wafers).[83,84] The increasing demand for unobtrusive photodetectors that can be used for human body or small electronic chips has led to a growing interest in state-of-the-art solutions. Organic semiconductors, such as π-conjugated molecules and polymers, are particularly attractive due to their high extinction coefficients, which result from strong light absorption in thin films arising from large wavefunction overlap between the electronic ground state and lowest excited state.[85–87] NIR non-fullerene acceptor is one of strategy key to achieve high-transparent device and high-detectivity in range of NIR wavelength (over 780 nm). Since most of the organic photodetectors are based on a donor:acceptor heterojunction, which can separate excitons and generate charges.[88] In this work, the PM2 donor polymers with 1.41 eV optical band gap (Eg^{opt}) was selected to fabricate device with new designed ultra-narrow bandgap NFAs. Two compositions of PM2:BCIC-4F and PM2:TCIC-4F are demonstrated in this section for NIR photon detecting devices. NIR materials including PM2 donor and two newly synthesized NFAs exhibit NIR absorption (thin-film state) with narrow optical bandgaps of 1.41 eV (PM2), 0.86 eV (BCIC-4F) and 0.98 eV (TCIC-4F), respectively. Consequently, the best estimated value of specific detectivity was 6.51×10^{12} at 1050 nm in the PM2:TCIC-4F based device.

2.2 Molecular design, simulation, and synthesis of ultra-narrow bandgap Non-Fullerene Acceptors (NFAs)

This section presents the newly designed non-fullerene acceptors (NFAs) materials utilizing the A-D-A’-D-A molecular structure to promote the enhanced intra-molecular charge transfer

(ICT) effect and thus achieves the ultra-narrow bandgap of <1.0eV NIR absorbers. With the purpose to efficiently explore more possible combinations of different electron efficient motifs (D) and electron deficient motifs (A and A') incorporated within the NFAs frameworks, DFT simulation for potential combinations of A-D-A'-D-A structured molecules have been utilized and the calculation results have been summarized in **Figure 2-1**.

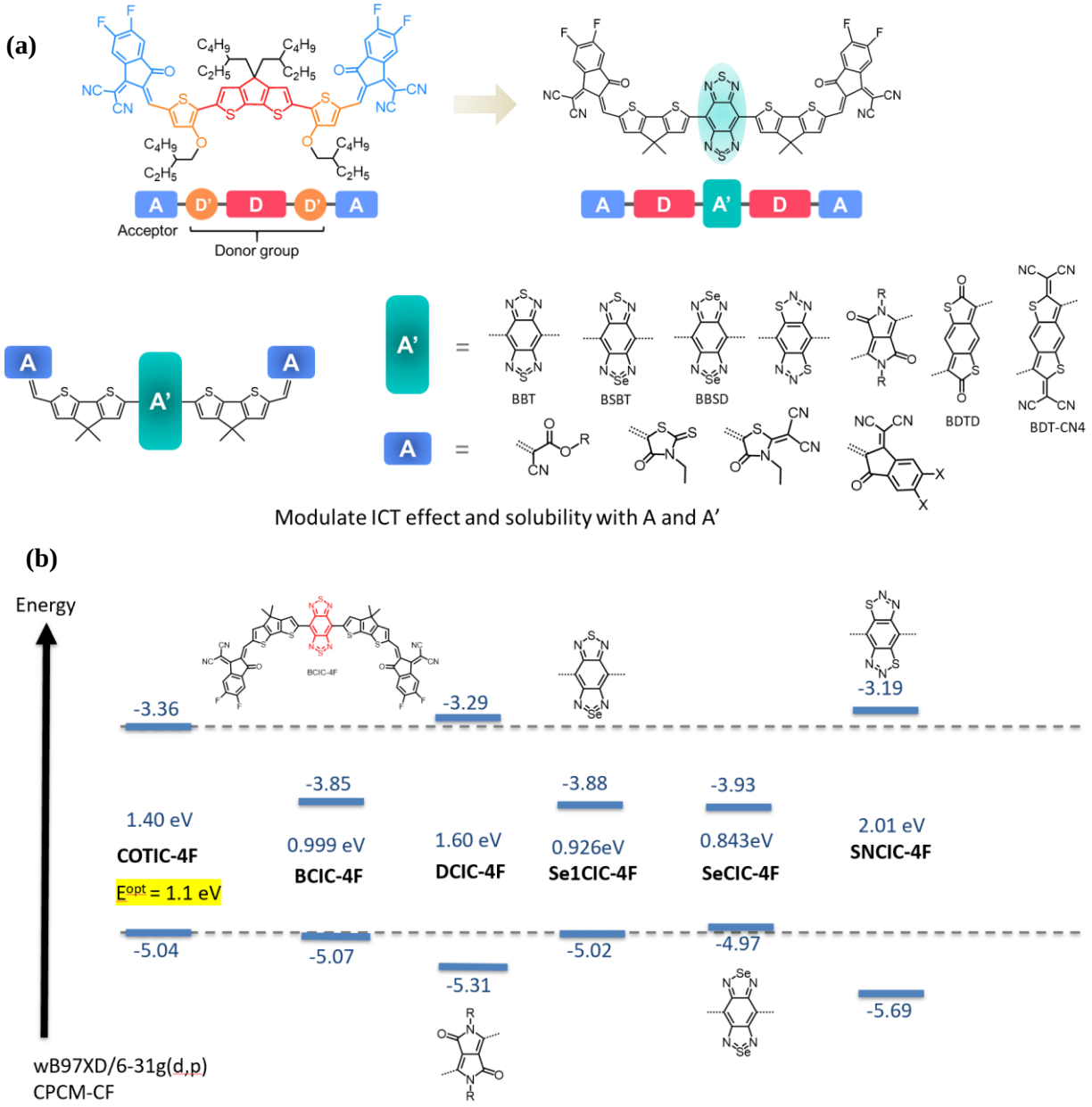

Figure 2-1. (a) Structural variations and (b) TD-DFT calculated bandgap of UNBG-NFAs.

New strategy for designing ultra-narrow bandgap NFAs (as shown in this **Figure 2-1**) have been utilized to push forward to further narrowed bandgap with the purpose of achieving efficient NIR-OPD device at 1200nm wavelength in infrared region. By integrating various electron donor and acceptor fragments within the molecular structure, ICT effect and corresponding materials' processibility could be easily tuned accordingly. Moreover, DFT calculation has been applied to prediction on molecular properties (frontier energy level of HOMO, LUMO, optical gap, oscillator strength etc.) for those newly structured NFAs that are designed based on A-D-A'-D-A strategy. These calculation results are summarized in **Figure 2-1b** compared with the standard structure of COTIC-4F that has been well-examined in our group previous published paper.[57] After the concept of "optimal tuning" and second geometry optimization have been fulfilled, time-dependent density functional theory (TD-DFT) is applied to study the excited states of our large molecular systems. As shown in the calculation summary figure, the BBT centered acceptor presents potentially narrowest bandgap that might be lower than 1.0eV and therefore achieve higher OPD response within Infrared detecting range. The molecular structures and synthesis efforts towards the two targeted molecules is demonstrated in **Figure 2-2**.

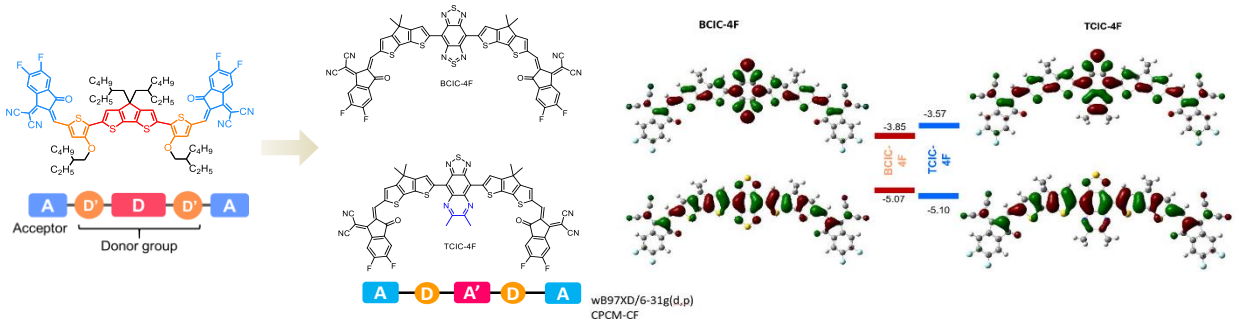

Figure 2-2. (a) Principles for designing new ultra-narrow bandgap NFAs (left) and Calculation (wB97XD/6-31g(d,p), solvation: CPCM CF) results for new NFAs (right).

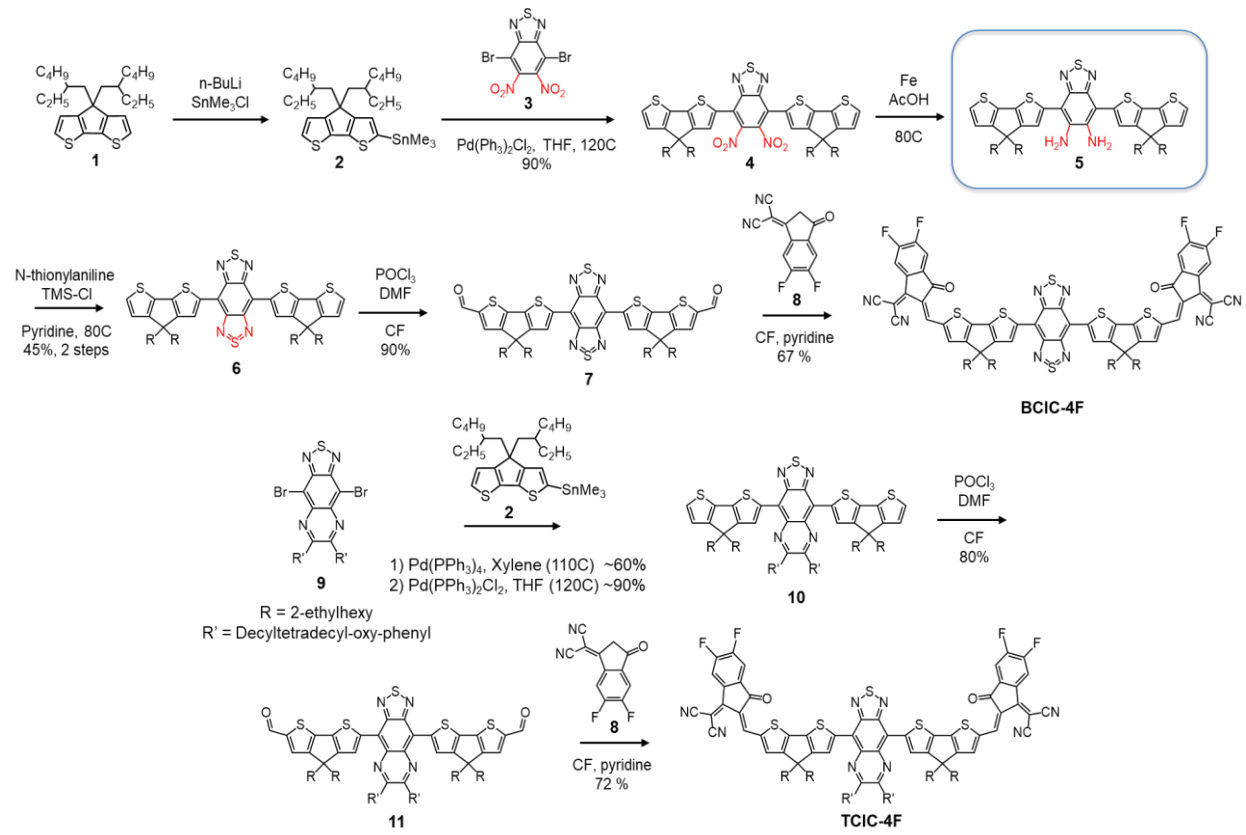

Figure 2-3. (b) Synthetic routes for UNBG-NFAs of BCIC-4F and TCIC-4F.

The synthesis route for two targeted molecules are summarized in **Figure 2-3**. The target molecule of BCIC-4F was synthesized through Stille coupling of compound 2 and 4,7-dibromo-5,6-dinitrobenzo[c][1,2,5]thiadiazole, after the reduction of the nitro-group and cyclization of Benzo[1,2-c:4,5-c']bis[1,2,5]thiadiazole (BBT) unit, Vilsmeier reaction and Knoevenagel condensation reaction were applied and targeted compound of BCIC-4F was obtained. The other NIR-NFA of TCIC-4F was prepared using the similar methods as shown in **Figure 2-3**.

To further examine the materials' optical properties, BCIC-4F and TCIC-4F chloroform (CF) solutions and thin-films casted from NFAs' 10mg/mL CF solutions at 1000 rpm were measured by the UV-Vis-NIR Spectroscopy. According to the absorption profile (**Figure 2-4**), TCIC-4F has as solution absorption peak at 928nm where BCIC-4F has the peak at 1032nm. In the thin-film UV-Vis spectra, BCIC-4F have two main absorption peaks where the second peak lies around 1200nm,

and the TCIC-4F has the solid-state absorption peak at 1086nm. With the onset absorption wavelength obtained from the absorption profile, the optical gaps for TCIC-4F and BCIC-4F were estimated as 1.0eV and 0.88eV, respectively. Cyclic Voltammetry (CV) experiment was conducted on a CHI-730B electrochemistry workstation with the three-electrodes system consisting of glassy carbon disk, Pt wire, and Ag wire electrode which serve as the working electrode, counter electrode, and pseudo reference electrode, respectively. The measurement was performed in 0.1M tetrabutylammonium hexafluorophosphate (n-Bu_4NPF_6)-anhydrous acetonitrile solution at the potential scan rate of 100 mV s^{-1}. Thin films of samples were deposited onto the glassy carbon working electrode from its 5 mg mL^{-1} chloroform solution. The electrochemical onsets were determined at the position where the current starts to differ from the baseline. The potential of Ag pseudo reference electrode was internally calibrated relative to Fc/Fc+ couple (−4.88 eV vs. vacuum). The HOMO level measured by CV for BCIC-4F is -5.4eV and the calculated LUMO level is -4.5eV. The HOMO level measured by CV for TCIC-4F is -5.6eV and the calculated LUMO level is -4.6eV (summarized in **Table 2-1**).

Table 2-1. Optical and electrochemical properties of BCIC-4F, TCIC-4F

NFA	**E_g^{opt} (eV)[a]**	**E_{HOMO} (eV)[b]**	**E_{LUMO} (eV)[c]**
BCIC-4F	0.86	-5.40	-4.50
TCIC-4F	0.98	-5.60	-4.60

[a]Optical band gap calculated from the absorption edge of thin film. [b]HOMO energy level estimated from the onset oxidation potential. [c]LUMO energy level estimated from the CV measured HOMO level and optical gap.

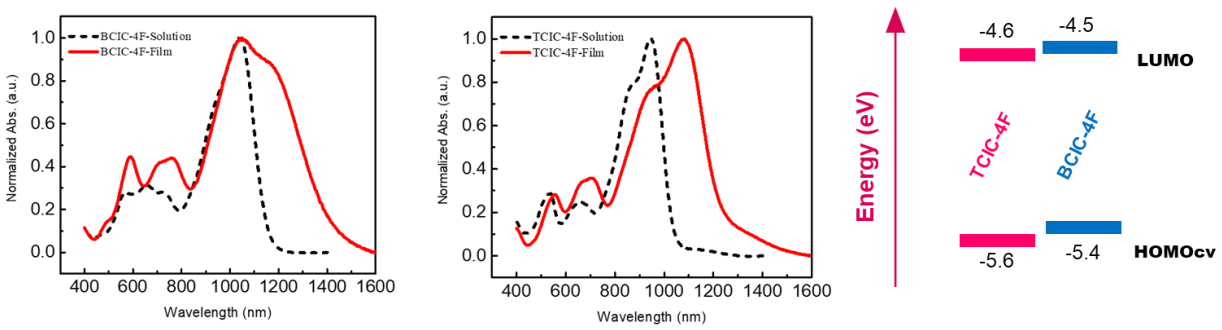

Figure 2-4. Optical and electrochemical characterizations of BCIC-4F and TCIC-4F.

2.3 Application in Near-Infrared organic photodetectors (NIR-OPDs)

To test the performance of originally designed and synthesized UNBG-NFAs of BCIC-4F and TCIC-4F with the help of DFT simulation, NIR-OPD devices have been fabricated with the structures presented in **Figure 2-5**. The molecular structures of donor and acceptors for comprising bulk hetero junction organic photodetectors, named PM2, BCIC-4F and TCIC-4F, are illustrated in **Figure 2-5b** and their device architecture and band diagram are depicted in **Figure 2-5 (b-c)**. PM2 polymer was chosen as a narrow bandgap donor material to blend with above NFAs. Because the compositions consist of only narrow bandgap materials (D:A blend), strong absorption of photons in the NIR region by devices could be expected.

The devices based on blends of PM2:BCIC-4F and PM2:TCIC-4F were fabricated in an inverted device structure of indium-tin-oxide (ITO)/zinc oxide (ZnO)/NIR D:A/MoO_3/Ag. The procedures of device fabrication were as follows. Firstly, the ITO-coated glass substrates were cleaned with detergent, then ultra-sonicated in acetone and isopropyl alcohol, and subsequently dried in an oven at 100 °C. Then, the cleaned ITO substrates were ultraviolet- ozone treated for 15 min to remove tiny organic residues. The zinc oxide (ZnO) solution was prepared using mixture of diethyl zinc solution in toluene and tetrahydrofuran (THF) (1:5, v/v %)

and the ZnO film (ca. 30 nm thick) was spin-coated at 3000 rpm for 20 s and annealed at 110 °C for 10 min. The blend solution of PM2:NFAs were dissolved in chlorobenzene, which are with and without processing additives such as 1,8-diiodooctane or 1-chloronaphthalene, wherein the ratio of Donor:Acceptor were 1:1.5 (D:A w/w) and the concentration of active solution were 25 mg/ml. These solutions are spin-coated at 2000 to 5000 rpm for film optimization in a nitrogen-filled glove box. The device was pumped down in vacuum (< 10^{-6} torr), and the MoO_3/Ag (5 nm/90 nm thick) electrode were deposited by thermal evaporation. Light-detecting characteristics measurements were carried out at the glove box by the solar simulator equipped with a Keithley 2635A source measurement unit. *J-V* curves were measured under AM 1.5G illumination at 100 mW cm^{-2}. EQE measurements were conducted in ambient air condition using an EQE system.

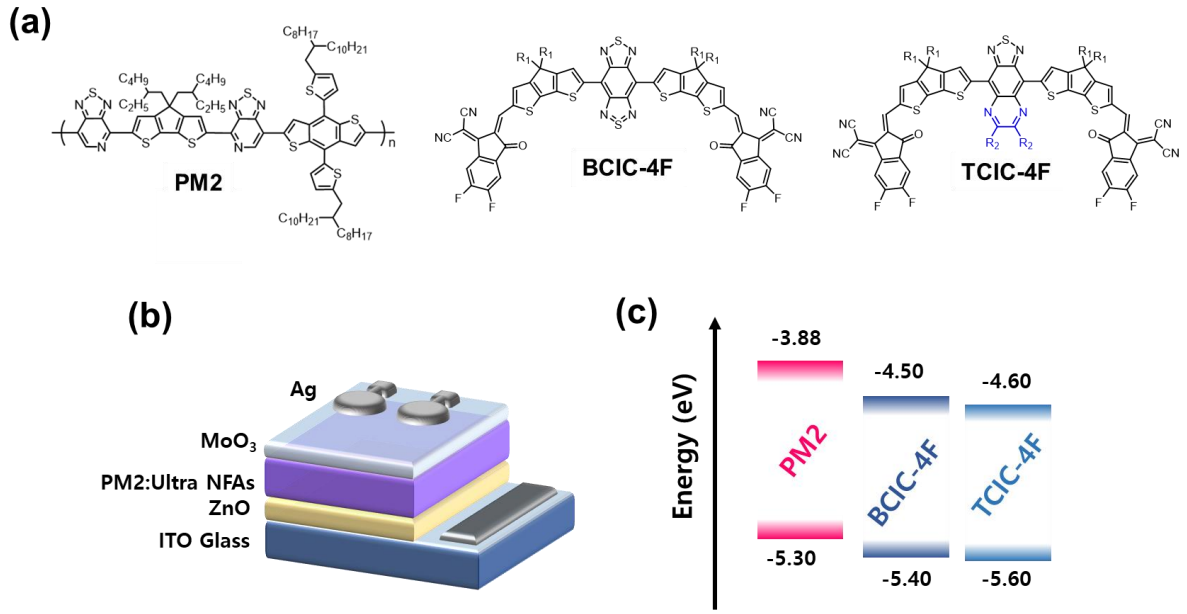

Figure 2-5. (a) Chemical structure of BCIC-4F, TCIC-4F and donor polymer, PM2 for optoelectronic devices (b) device architecture and (c) frontier energy levels.

The performance both OPVs and OPDs are listed in **Table 2-2** and corresponded J-V curve, EQE spectra, spectra of responsivity and specific detectivity, and dark current of devices are shown in **Figure 2-6**. PM2:BCIC-4F-based organic solar cells showed less than 1 mA/cm^2 of short circuit current (Jsc) under 1 sun irradiation and EQE of un-reached the expected 1400 nm wavelength. While, photodiode of PM2:TCIC-4F blend system without additives showed Jsc of 1.51 mA/cm^2, the higher value of Jsc (2.26 mA/cm^2) are obtained from blend with 2% (v/v) 1-Chloronaphthalene processing additive. Hence, PM2:TCIC-4F based device demonstrated two dominant peaks at around 720-730 nm and around 1040-1050 nm as shown in EQE spectra, which arise from maximum absorption of PM2 and TCIC-4F, respectively. Here, PM2:BCIC-4F based device showed maximum EQE peak at around 810 nm compared to PM2:TCIC-4F based device is due to the combined effect of different secondary absorption of NFAs. Maximum responsivities under photovoltaic mode (@ 0V) of 0.009 and 0.042/0.039 were determined for PM2:BCIC-4F, and PM2:TCIC-4F based devices at 810 nm and 730 nm / 1050 nm, respectively. In addition, The maximum specific detectivity (D*, Jones) measured for PM2:BCIC-4F is 6.51×10^{11} Jones at the 810 nm wavelength, while PM2:TCIC-4F showed 1.82×10^{12}, and 6.51×10^{12} Jones at each maximum wavelength.

**** Information of device characterization (OPDs)**

External quantum efficiency (EQE), the ratio of the number of charge carriers collected by the device to the number of photons from incident light, were measured at 0 V bias. Dark current of OPD devices based on PM2:BCIC-4F and PM2:TCIC-4F blends were measured to calculate photodetector characterization. Generally, Responsivity and specific detectivity (D*) were well-known as figure of merit for photodetector. Here, Responsivity defined photocurrent per incident

unit optical power, other words, electrical output of photon input, which can be obtained from the equation (1).

$$R = \eta \frac{q\lambda}{hv} \qquad (1)$$

Specific detectivity (D*) means sensitivity to monochromatic radiation at which its performance is best. Larger D* means detecting week signal which compete with the detector noise. Calculation of D* is from equation (2).

$$D* = \frac{R}{\sqrt{2qJ_D}} \qquad (2)$$

(Here, hv = photon energy, q = elementary charge, η = quantum efficiency, λ = Wavelength, J_D=the dark current density)

Table 2-2. Photovoltaic performances of devices based on PM2:NFAs measured under simulated 100 mW cm^{-2} AM 1.5G illumination and Photodetector performances estimated from dark current and external quantum efficiency (EQE).

NFAs	Additives	J_{SC} @ 0V (mA/cm²)	V_{OC} (V)	FF (%)	PCE (%)	EQE	Responsivity @λ_{max}[a]	Responsivity @λ_{max}[b]	Specific Detectivity* (Jones @0 V)[a]	Specific Detectivity* (Jones @0 V)[b]
BCIC-4F	None	0.40	0.21	0.30	0.0253	0.33	0.009@810	-	6.51×10^{11}	-
	CN	0.13	0.12	0.27	0.0041	-	-	-	-	-
	DIO	0.22	0.19	0.31	0.0129	0.13	0.004@810	-	1.47×10^{11}	-
TCIC-4F	None	1.51	0.47	0.34	0.24	1.34	0.024@720	0.024@1040	7.26×10^{11}	7.48×10^{11}
	CN	2.26	0.49	0.40	0.44	2.31	0.042@730	0.039@1050	1.82×10^{12}	6.51×10^{12}
	DIO	1.05	0.42	0.32	0.14	-	-	-	-	-

a: Estimated value in relatively shorter wavelength. b: Estimated value in NIR region

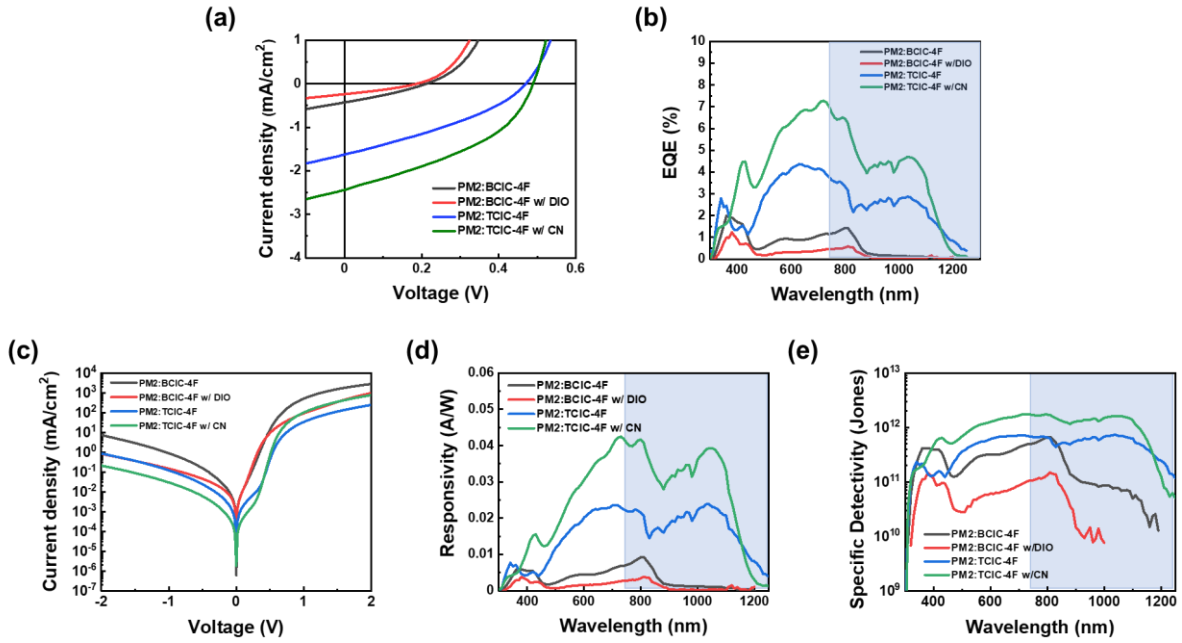

Figure 2-6. Device characterization: (a) *J-V* curve, (b) EQE spectra, (c) dark current, (d) responsivity and (e) specific detectivity.

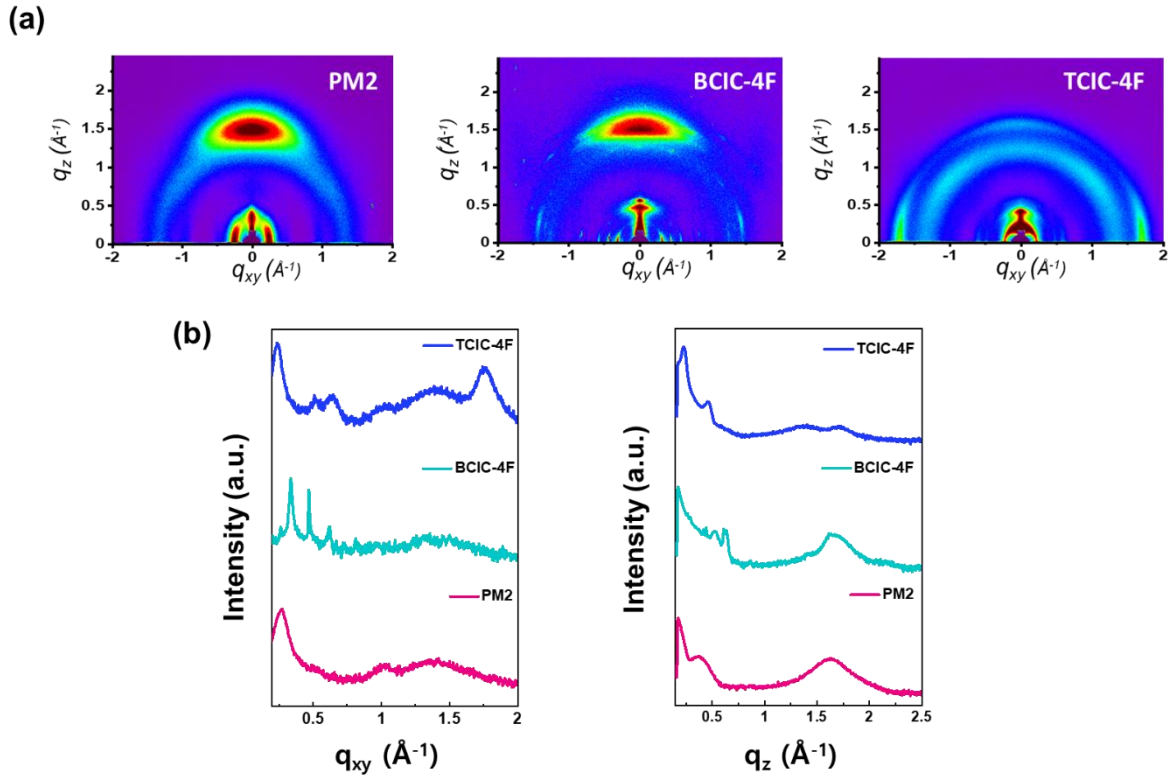

Figure 2-7. 2D image of GIWAXS and plotted line of scattering vector in q_{xy} and in q_z direction.

Grazing-incidence wide-angle X-ray scattering (GIWAXS) is sensitive to the crystalline parts and enables the determination of the orientation of structure, therefore, it is used to better understand organic film optimization approaches. To investigate the molecular packing in PM2, BCIC-4F and TCIC-4F pristine thin-films, we carried out GIWAXS as shown in **Figure 2-7**. PM2 donor polymer exhibits a strong peak along q_z axis with scattering vector of 1.62 $Å^{-1}$, indicating a vertical π-π stacking as a face-on orientation. Pure BCIC-4F film also exhibited face-on orientation with the multi-ordered lamellar stacking on q_{xy} direction. In contrast, pure TCIC-4F film showed strong π-π stacking peak along q_{xy} axis with scattering vector of 1.75 $Å^{-1}$, which indicate that the horizontal streak (edge-on) was observed.

2.4 Additional data for donor polymer optimization

In previous subsections of this chapter, TCIC-4F and BCIC-4F were designed and synthesized achieving ultra-narrow optical bandgap of less than 1 eV. TCIC-4F has HOMO energy level of -5.60 eV and LUMO energy level of -4.60 eV, absorbing up to 1200 nm in thin-film state. Consequently, TCIC-4F showed the maximum absorption peaks of around 1100 nm in NIR region. To test their performance in range of NIR wavelength, the NIR-OPD devices were fabricated with configuration of ITO/ZnO/Active layer/MoO3/Ag. Wherein the active layers were based on 1:1.5 (w/w) ratio of D:A dissolved in chlorobenzene. However, there's challenging task in the device optimization process regarding the choice of composite donor polymer while TCIC-4F material presents relatively deep-lied HOMO level. Therefore, PBDTTT-C-T, PTB7, PM2 donor polymers were selected for suitable energy level in align with TCIC-4F NFA and device study were conducted with the purpose to examine the relationship between energy offset (ΔLUMO or ΔHOMO) and corresponding OPD performance (**Figure 2-8**).

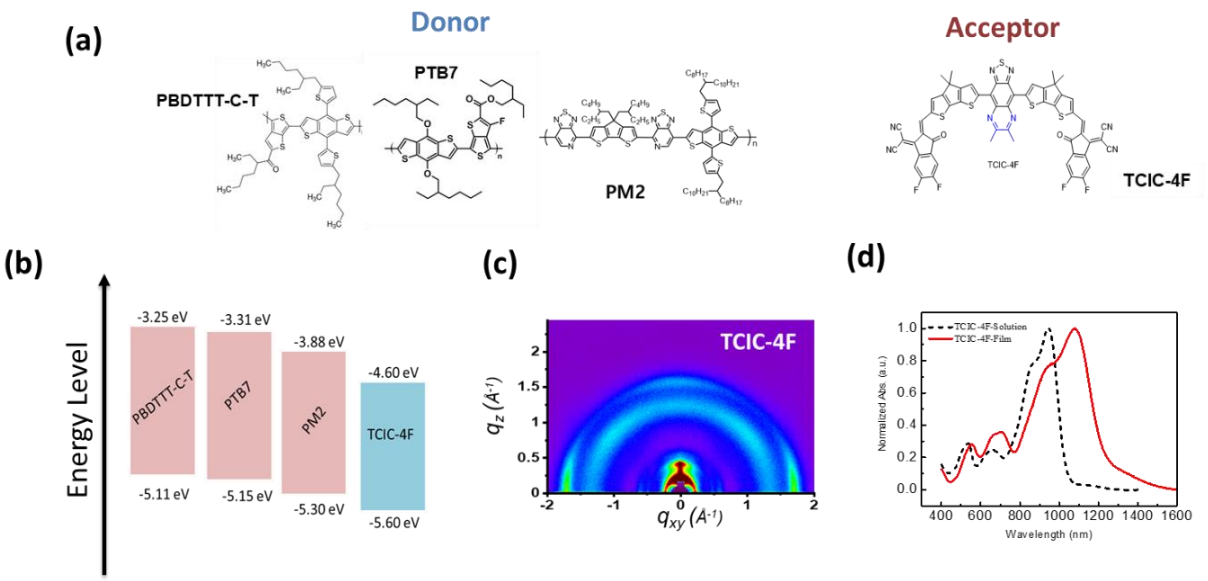

Figure 2-8. (a) chemical structure of donors and ultra-narrow bandgap NFA, TCIC-4F (b) band diagram of materials (c) 2D GIWAXS images of pure TCIC-4F film and (d) absorption spectra of TCIC-4F solution and TCIC-4F film.

Table 2-3. Performances of OPDs based on TCIC-4F NFA measured under simulated 100 mWcm^{-2} AM 1.5G illumination and estimated from dark current and external quantum efficiency (EQE).

Donor	Additives	J_{SC} @0V (mA/cm^2)	J_{SC} @-1V (mA/cm^2)	EQE 0V/-1V (mA/cm^2)	Responsivity[a] @λ_{max} (A/W @0V, @1050 nm)	Responsivity[b] @λ_{max} (@-1V, @ 1050 nm)	Specific Detectivity*[a] (Jones @0 V, @ 1050 nm)	Specific Detectivity*[b] (Jones @-1 V, @ 1050 nm)
PTB7	None	4.18		3.86	0.049	0.095	2.41×10^{12}	3.88×10^{11}
PBDTTT-CT	2% CN	2.67	4.73	1.92/3.74	0.032	0.063	1.11×10^{12}	1.03×10^{11}

a. Estimated value at zero bias, b. Estimated value at longer -1V.

PTB7:TCIC-4F and PBDTTT-C-T:TCIC-4F based OPDs will be reported as a self-power mode OPDs (performance at zero bias) and operation in reverse bias (performance at -1V). As shown in **Figure 2-8b**, PTB7 donor polymer has -5.12 eV HOMO energy level and -3.31 eV energy level, while PBDTTT-C-T donor polymer has -5.11 eV HOMO energy level and -3.25 eV energy level. The summarized performance of the PTB7:TCIC-4F OPDs and PBDTTT-C-T:TCIC-4F OPD devices were listed in **Table 2-3**. Maximum responsivities at 1050 nm under self-power mode (0 V) were calculated by 0.049 A/W and 0.32 A/W for PTB7:TCIC-4F, and PBDTTT-C-T:TCIC-

4F-based best devices (so far), respectively, and it also showed responsivities of 0.095 A/W (PTB7:TCIC-4F) and 0.063 A/W (PBDTTT-C-T:TCIC-4F) at -1V. **Figure 2-9** showed J-V curve, spectra of EQE, responsivities and specific detectivities. It is observed that the value at shorter wavelength related with maximum absorption of donors and the performance at longer wavelength (1050 nm) also related with photocurrent from maximum absorption of TCIC-4F NFA. As shown in **Figure 2-9**, spectra of EQE, responsivity and specific detectivity showed significant two high peaks corresponding to the effect of donors and acceptor. On the other hand, the maximum D* of the best PTB7:TCIC-4F device are 2.41 × 1012 (1050 nm) Jones at 0V and 3.88 × 1011 (1050 nm) Jones at -1V while, PBDTTT-C-T:TCIC-4F device showed the D* of 1.11×1012 (1050 nm) Jones at 0V and 1.03 × 1011 (1050 nm) Jones at -1V.

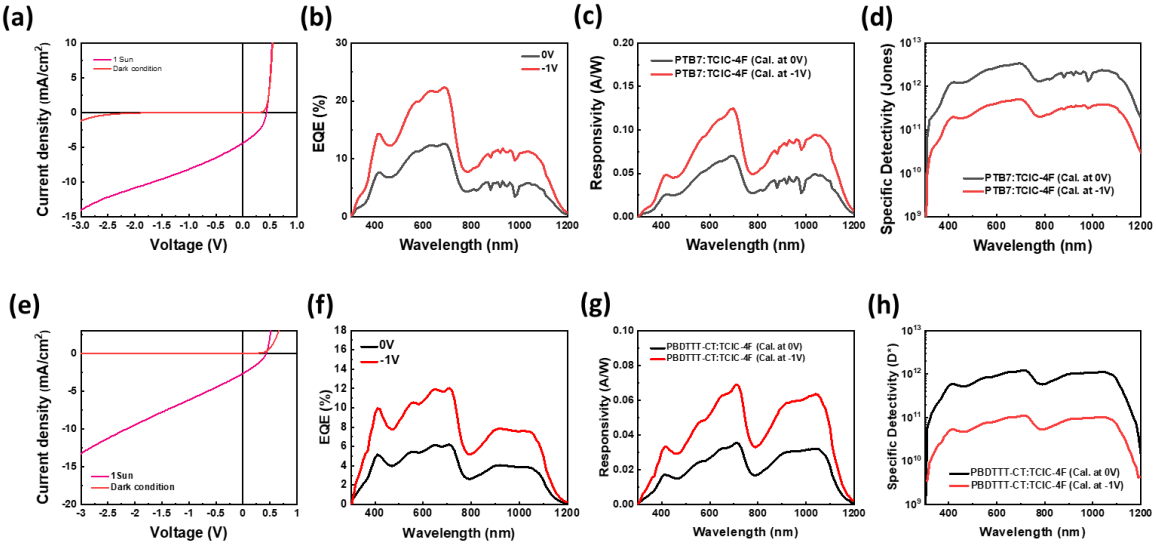

Figure 2-9. (a, e) J-V characteristics, (b,f) EQE spectra at 0V and -1V, (c,g) spectra of responsivity and (d,h) spectra of specific detectivity. Upper characteristics are PTB7:TCIC-4F based devices and bottom figures are based on PBDTTT-C-T:TCIC-4F OPDs.

To investigate the estimate charge transfer state in bulk heterojunction (BHJ) active film, photoluminescence for PTB7:TCIC-4F, PTB7, PBDTTT-D-T:TCIC-4F and PBDTTT-CT were measured. basically, all generated excitons in donor material showed radiative recombination. And, in case of blend system, the generated exciton dissociated at a donor-acceptor interface because of

the driving force of acceptor. That leads to a strong quenching of the photoluminescence of donor as a kind of non-radiative recombination process. **Figure 2-9** showed spectra of PL intensity for PTB7-based films and PBDTTT-C-T-based films, respectively. The excitation wavelength were 550 nm and 630 nm for PBT7-based films and PBDTTT-C-T-based films. PTB7 case showed 89% reduced intensity comparing to PBDTTTCT of 81%, which indicate that PTB7 blends-based device might have more sufficient charge transport than PBDTTT-CT. Which might related to the higher performance of PTB7:TCIC-4F based OPDs.

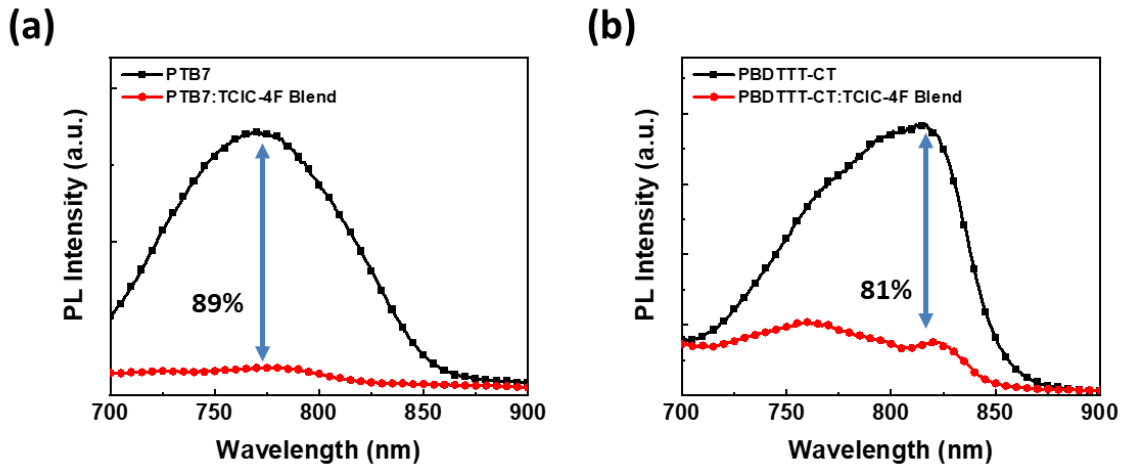

Figure 2-10. Photoluminescence of PBT7-based films and PBDTTT-C-T-based films

External quantum efficiency (EQE) is defined as the number of electrons provided to the external circuit per photon incident on the device, while IQE defined as the ratio of the number of electron-hole (e-h) pairs or charge carriers generated to the number of photons absorbed, within the active layer in device. To obtain IQE from EQE spectra, we measured reflectance of the films and calculated using follow equation.

$$IQE = \frac{EQE}{1 - R}$$

From the IQE measurement, it is available to account the recombination loss. Typically, for a superior quality material or blend film with low dislocation density and defects, IQE could be close

to 100%. Therefore, by comparison between IQE and EQE spectra (commonly, the EQE is lower than the IQE), we can note the losses at the BHJ interface, charge extraction in device in this work. EQE of PTB7:TCIC-4F-based OPD showed closer to the IQE spectra values compared to the PBDTTT-C-T:TCIC-4F device, which provide the reason why the PTB7:TCIC-4F-based OPDs has higher performance.

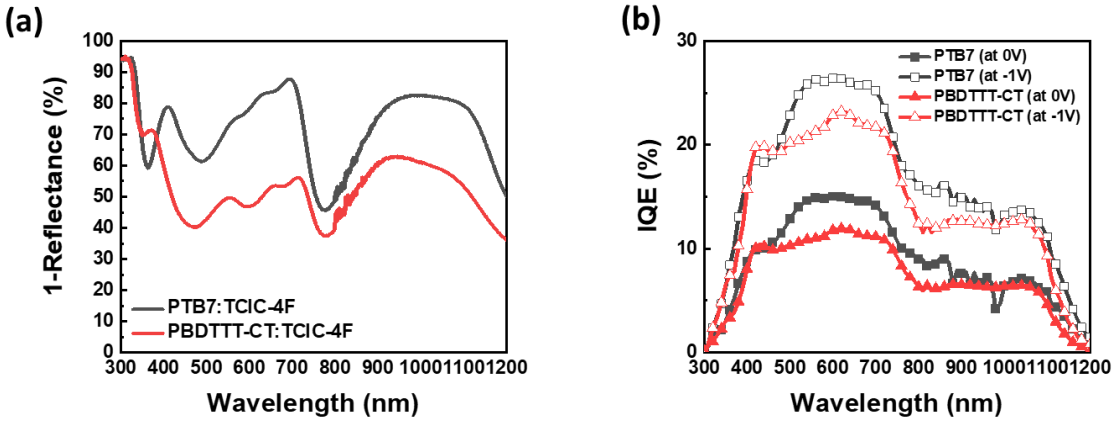

Figure 2-11 (a) 1-R (%) and (b) calculated IQE spectra.

To demonstrate the film morphologies, optimal blend films both PTB7:TCIC-4F and PBDTTT-CT:TCIC-4F were measured by tapping mode Atomic force microscope (AFM). PTB7:TCIC-4F films displayed the smooth surface with 0.703 nm roughness, in contrast, PBDTTT-C-T:TCIC-4F films showed large clusters with higher roughness of 1.99 nm. This smoothness of films have effect on charge extraction in devices.

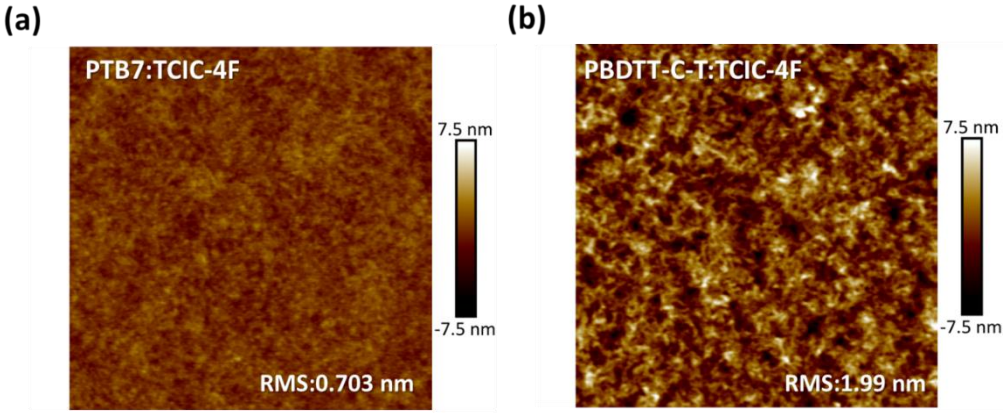

Figure 2-12. Surface morphology of (a) PTB7:TCIC-4F film and (b) PBDTTT-C-T:TCIC-4F film. The size is 4×4 (μm^2).

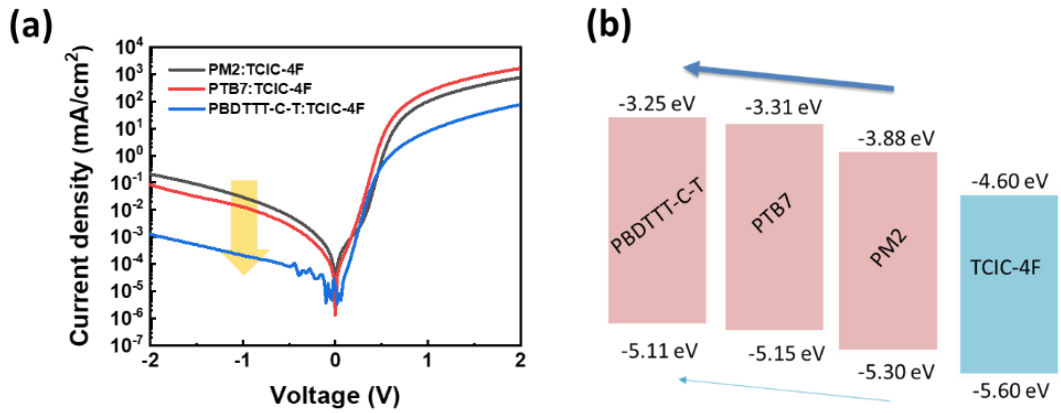

Figure 2-13. (a) Dark current characteristic and (b) energy level of materials studied

In this work, we have discovered a worth-noting point for discussion. **Figure 2-13** showed the dark current of three blend system (PM2:TCIC-4F, PTB7:TCIC-4F and PBDTTT-C-T:TCIC-4F) devices and energy levels. PM2:TCIC-4F based information was already reported in previous subsection of this chapter. Although PBDTTT-C-T:TCIC-4F OPDs resulted in lower current density under 1 sun illumination, it showed lower leakage current at reverse bias in dark condition. Here, we hypothesized that huge difference of off-set leads bigger separation of the energy band (other words, it makes bigger electrostatic potential barrier and extend transition region width in perspective of pn-junction). Therefore, charge flows are quite minimized at reverse bias, resulting in lower dark current. In other words, increasing off-set difference of LUMOD-LUMOA and HOMOD-HOMOA can lead to higher photocurrent and enhancement of OPD performance.

2.5 Conclusions and potential improvements

As optoelectronic devices absorbing visible light have been continuously developed, it is necessary to extend the spectrum of utilization with development of NIR absorbing materials. Since the introduced compositions have relative strong absorption in near-infrared region, the NIR organic optoelectronics might contribute to unobtrusive application like devices to be used in healthcare by continuous detection of physiological signals. Thus, the realization of lightweight

and conformal image sensors with color or infrared sensitivity would open numerous opportunities not only in wearable electronics but also in prosthetics, robotics, and automotives.

In this contribution, NIR absorbing donor (PM2) and ultra-narrow bandgap NIR-non fullerene acceptors (BCIC-4F and TCIC-4F) were synthesized and introduced for organic solar cells and organic photodetectors in this work. Since PM2 polymer has narrow energy bandgap of ~1.41 eV and absorbs the sunlight until wavelength of ~900 nm, compositions with NIR non-fullerene acceptors can exhibit broaden NIR light absorption and high transparency to human's naked eyes with superior performance in NIR range. This chapter concludes the description of molecular design strategy synthesis route, the optical and electrical properties of UNBG-NFAs absorbers as well as the device structure and methods of the corresponding all narrow bandgap materials composited device fabrication, with photovoltaic and photodetector performances.

Related non-fullerene acceptor materials can be designed and synthesized with different chemical structures to tune chemical properties for narrower bandgaps and higher device performance. In addition, the device performance can be improved through further morphology control of active layer. Further device optimization includes but not limited to donor/acceptor ratio, solvent, solution concentration, processing additive type and amount, film deposition method (spin coating, blade coating, drop casting etc.), film deposition temperature, film thickness, buffer layers (electron transporting layer, hole transporting layer). In addition, the above systems can be applied to various organic electronic devices including organic solar cells, organic field effect transistor and organic sensor. organic photodetectors (OPDs) with NIR responsivity have plenty of applications such as image sensing, night surveillance, optical communication, and health monitoring. The recent impressive improvement in organic electronic devices is expected to be of relevance with the advent of highly efficient NIR NFA materials.

2.6 Experimental methods

Materials All reagents and chemicals were purchased from commercial sources and used without further purification. All anhydrous organic solvents for the synthesis, characterization, and device fabrication steps were purchased from Sigma-Aldrich and TCI. Compounds **3**, **8**, **9** were purchased from SunaTech Inc. Compound **1** and **2** were prepared *via* a modified synthetic condition from literature.[89]

Calculation methods The optimized structures, energy levels, and HOMO and LUMO orbital distributions were calculated the density functional (DFT) level of theory, using the semi-empirically tuned wB97XD/6-31G(d,p) functional and basis set. The simulated absorption peak wavelength pf designed molecules were calculated via time-dependent DFT simulation method. To simplify calculations, the alkyl chains were replaced with methyl or ethyl chains. The HOMO and LUMO levels were calculated by determining the difference in energy from the optimized ground state geometry of the cation and anion, respectively.[90]

Characterizations of compounds ^{1}H and ^{13}C NMR spectra of intermediate monomers were recorded on a **Varian Unity Inova 500 MHz spectrometer** in deuterated chloroform solution ($CDCl_3$) with 0.003%TMS as internal reference. Ultraviolet-Visible-Near-infrared (UV-Vis-NIR) absorption spectra were recorded on a Perkin Elmer Lambda 750 spectrophotometer. For the measurements of thin films, materials were spun coated onto precleaned glass substrates from chloroform solutions (10 mg mL^{-1}). Optical band gap was determined from the absorption onset of thin film sample.

Electrochemical characterization The electrochemical cyclic voltammetry (CV) was conducted on a CHI-730B electrochemistry workstation with glassy carbon disk, Pt wire, and Ag/Ag+

electrode as the working electrode, counter electrode, and reference electrode, respectively in a 0.1 M tetrabutylammonium hexafluorophosphate (*n*-Bu_4NPF_6) anhydrous acetonitrile solution at a potential scan rate of 40 mV s^{-1}. Thin films of samples were deposited onto the glassy carbon working electrode from a 3 mg mL^{-1} chloroform solution. The electrochemical onsets were determined at the position where the current starts to differ from the baseline. The potential of Ag/AgCl reference electrode was internally calibrated by using the ferrocene/ferrocenium redox couple (Fc/Fc^+).

Grazing incidence wide angle X-ray scattering (GIWAXS) analysis 2D GIWAXS measurements were performed using Beamline 9A at the Pohang Accelerator Laboratory (PAL). The photon energy is 11.055 keV (λ = 1.1214 Å). The angle between the film surface and the incident beam was fixed at 0.12° for all of the samples. The measurements were obtained at scanning intervals of 2θ between 3° and 25°. The 2D GIWAXS images from the films were analyzed according to the relationship between the scattering vector q and the d spacing, $q = 2\pi/d$. The GIWAXS images shown are normalized with respect to exposure time.

Material Synthesis[62,91,92]

Compound **4**: A mixture of compound **3** (768mg, 2 mmol), compound **2** (2.7g, 4.8 mmol), $Pd(PPh_3)_4$ (47 mg) and anhydrous THF (20 mL) was added into a flame-dried and nitrogen-filled microwave tube in glovebox. The reactant was heated to 120 °C for 24 h. After the mixture cooled to room temperature, DI water was added, and the mixture was extracted with dichloromethane (50 ml x 3). The organic layer was dried over Na_2SO_4 and concentrated in vacuum. The crude product was purified by silica gel column chromatography (*n*-hexane:DCM, 9:1) to afford **4** as a deep blue solid (1.85g, 90%). MS (MALDI-TOF): calculated m/z 1027.53; found m/z 1027.8.

^{1}H NMR for compound **4** (500MHz, $CDCl_3$, ppm): δ 7.40 (t, 2H), 7.30 (d, 2H), 6.99 (m, 2H), 1.88–1.99 (m, 8H), 0.86-1.05 (m, 36H), 0.76-0.78 (m, 4H), 0.71–0.75 (m, 8H), 0.60–0.65 (m, 12H).

Compound **5**: Compound **4** (740 mg, 0.72 mmol), Fe powder (504 mg, 9 mmol) and 20mL Acetic Acid were added into a N_2 purged 50mL round bottom flask. The reaction was heated to 80 °C overnight then cooled to room temperature and diluted with 100mL DI water. The mixture was extracted with dichloromethane (50 ml x 3), dried over K_2CO_3 and concentrated in vacuum to afford **5** as a yellow brown solid that was relatively pure by ^{1}H NMR and MALDI-TOF and used for the next step without further purification.

^{1}H NMR for compound **5** (500MHz, $CDCl_3$, ppm): δ 7.15-7.28 (m, 2H), 7.17 (d, 2H), 6.97 (m, 2H), 4.48 (br, 4H), 1.90–1.99 (m, 8H), 1.00-1.10 (m, 36H), 0.85-0.90 (m, 4H), 0.71–0.80 (m, 8H), 0.62–0.68 (m, 12H). MS (MALDI-TOF): calculated m/z 966.48; found m/z 966.9.

Compound **6**: Compound **5** (450 mg, 0.46mmol) was dissolved in 5mL anhydrous pyridine in a microwave tube, N-thionylalanie (131 mg, 0.94mmol) and TMSCl (290mg, 2.66 mmol) were added in the glovebox. The reaction was heated to 80 °C and stirred for 24h. After cooling to room temperature, the reaction was diluted with DI water, extracted with dichloromethane (50 ml x 3), dried over Na_2SO_4 and concentrated in vacuum. The crude product was purified by silica gel column chromatography (n-hexane:DCM, 6:1) to afford **6** as a yellow solid (260mg, 56% for 2 steps).

^{1}H NMR for compound **6** (500MHz, $CDCl_3$, ppm): δ 9.16 (m, 2H), 7.33 (d, 2H), 7.03 (m, 2H), 4.48 (br, 4H), 1.95–2.16 (m, 8H), 0.98-1.04 (m, 36H), 0.93-0.95 (m, 4H), 0.74–0.77 (m, 8H), 0.62–0.68 (m, 12H). MS (MALDI-TOF): calculated m/z 994.42; found m/z 995.6.

Compound **10**: A mixture of compound **9** (240mg, 0.2 mmol), compound **2** (284mg, 0.5 mmol), $Pd(PPh_3)_4$ (11 mg) and anhydrous THF (10 mL) was added into a flame-dried and nitrogen-filled microwave tube in glovebox. The reactant was heated to 120 °C overnight. After the mixture cooled to room temperature, DI water was added, and the mixture was extracted with dichloromethane (50 ml x 3). The organic layer was dried over Na_2SO_4 and concentrated in vacuum. The crude product was purified by silica gel column chromatography (*n*-hexane:DCM, 8:1) to afford **10** as a deep green solid (332mg, 90%).

^1H NMR for compound **10** (500MHz, $CDCl_3$, ppm): δ 9.17 (d, 2H), 7.83 (d, 4H), 7.22 (d, 2H), 7.01 (m, 4H), 6.99 (s, 2H), 3.94 (d, 4H) 1.93-2.09 (m, 8H), 1.82-1.87 (m, 6H), 1.2-1.44 (br, 74H), 0.93-1.06 (m, 32H), 0.74-0.89 (m, 26H), 0.60-0.65 (m, 16H). MS (MALDI-TOF): calculated m/z 1845.27; found m/z 1846.3.

The general procedure for the synthesis of bisaldehyde intermediate **7** and **11** is described as follows. To a flame-dried and nitrogen-filled one-neck round-bottom flask, $POCl_3$ and DMF were added in anhydrous Chloroform (CF) solvent at 0 °C. The solution was reacted at 0 °C for 30min, then a solution of compound **6** (or **10**) in CF was added. The reactants were heated to reflux overnight, giving a read solution. The reaction was quenched by DI water and stirred for 30min at room temperature. The mixture was extracted with ether (50 ml x 3), washed by DI water. The organic layer was dried over Na_2SO_4 and concentrated in vacuum. The residue was purified by silica gel column chromatography.

Compound **7:** Compound **6** (260 mg, 0.26 mmol), $POCl_3$ (0.50mL), DMF (4.01mL) and 10mL of CF solvent were used for the reaction. The crude product was purified by using silica gel column chromatography (*n*-hexane:DCM, 6:4) to afford **7** as a deep yellow solid (260mg, 94%).

^{1}H NMR for compound **7** (500MHz, $CDCl_3$, ppm): δ 9.91 (s, 2H), 9.21 (m, 2H), 7.66 (t, 2H), 2.02–2.22 (m, 8H), 0.96-1.06 (m, 36H), 0.75-0.78 (m, 8H), 0.61–0.69 (m, 20H).

Compound **11:** Compound **10** (266 mg, 0.144 mmol), $POCl_3$ (0.333mL), DMF (2.2mL) and 10mL of CF solvent were used for the reaction. The crude product was purified by using silica gel column chromatography (*n*-hexane:DCM, 6:4) to afford **11** as a deep yellow solid (222mg, 80%).

^{1}H NMR for compound **11** (500MHz, $CDCl_3$, ppm): δ 9.88 (s, 2H), 9.25 (d, 2H), 7.82 (m, 4H), 7.62 (d, 2H), 6.01 (m, 4H), 3.95 (d, 4H) 1.99-2.15 (m, 8H), 1.83-1.87 (m, 6H), 1.26-1.34 (br, 74H), 0.92-1.06 (m, 32H), 0.74-0.89 (m, 26H), 0.55-0.66 (m, 16H).

The general procedure for the synthesis of final products (**BCIC-4F** and **TCIC-4F**) is described as follows. A mixture of bisaldehyde intermediate **7** (or **11**), 2-(5,6-difluoro-3-oxo-2,3-dihydro-1H-inden-1-ylidene)malononitrile (compound **8**), dry chloroform (20 mL), and pyridine was added into to a flame-dried and nitrogen-filled one-neck round-bottom flask The flask was purged with N_2 for 20 min and the reactant was heated to 60 °C for 12 h. After the mixture cooled to room temperature, the reaction mixture was concentrated in vacuum. The residue was purified by silica gel column chromatography.

BCIC-4F: Compound **7** (170 mg, 0.162 mmol), compound **8** (124mg, 0.54mmol), pyridine (0.2mL) and 30mL of anhydrous CF solvent were used for the reaction. The crude product was purified by using silica gel column chromatography (*n*-hexane:DCM, 1:1) to afford **BCIC-4F** as a deep blue solid (160mg, 67%).

^{1}H NMR for **BCIC-4F** (500MHz, $CDCl_3$, ppm): δ 9.12 (s, 2H), 8.96 (s, 2H), 8.50 (m, 2H), 7.68 (m, 4H) 2.03–2.21 (m, 8H), 1.25 (s, 6H), 1.05 (br, m, 30H), 0.62–0.77 (m, 24H). MS (MALDI-TOF): calculated m/z 1475.93; found m/z 1475.48.

TCIC-4F: Compound **11** (200 mg, 0.103 mmol), compound **8** (80mg, 0.35mmol), pyridine (0.2mL) and 40mL of anhydrous CF solvent were used for the reaction. The crude product was purified by using silica gel column chromatography (*n*-hexane:DCM, 1:1) to afford **TCIC-4F** as a deep purple solid (175mg, 72%).

^{1}H NMR for **TCIC-4F** (500MHz, $CDCl_3$, ppm): 9.37 (t, 2H), 8.94 (s, 2H), 8.56 (q, 2H), 7.85 (t, 2H), 7.84 (t,2H), 7.59 (t, 4H), 7.11 (m, 4H), 4.02 (d, 4H), 2.05-2.22 (m, 8H), 1.88-1.93 (m, 6H), 1.27-1.38 (br, 74H), 0.97-1.09 (m, 32H), 0.82-0.90 (m, 16H), 0.59-0.78 (m, 24H). MS (MALDI-TOF): calculated m/z 2325.3; found m/z 2326.3.

Chapter 3: Green Solvent Processable Organic Semiconductors

3.1 Introduction

Organic semiconductors have gained widespread attention and applications in the past few decades due to their unique properties such as lightweight, flexibility, and excellent industry potential for high throughput solution processing and roll-to-roll printing technologies. Organic solar cells (OSCs), wearable electronics, and organic photodetectors (OPDs) are some of the applications where these semiconductors are extensively used.[19,85,93,94] Despite their advantages, the use of traditional solvents in OPV processing is a major concern as they are commonly highly toxic halogenated organic solvents like chlorobenzene (CB), o-dichlorobenzene (O-DCB), tri-chlorobenzene (TCB), and chloroform (CF). These solvents not only pose a risk to human health upon exposure, threatening long-term negative effects on the ecosystem but also cost more fiscally regarding the solvent waste disposal expenses. Therefore, there is a need for research and development of halogen-free/"green solvent" (**Figure 3-1**) processable organic semiconductors to make organic photovoltaics a viable option for real-life applications. The use of green solvents would not only make the processing of these semiconductors safer for human health and the environment, but it would also reduce the cost of production, making them more accessible to people. The development of halogen-free/green solvent processable organic semiconductors is essential for the advancement and wider use of organic photovoltaics, and it represents a significant step towards sustainable and environmentally friendly technologies.[95,96] While the use of green solvents is a promising approach towards safer and more sustainable organic photovoltaics, there are limited research works on green solvent processable organic semiconductors. Some recent studies have focused on designing new light-harvesting materials by introducing solvation sidechains that enhance the materials' solubility in polar processing solvents.[97–100] However, the

development of high-performance semiconductors that can be processed by high dielectric constant green solvents is still a challenge. Additionally, fundamental studies such as film morphology, optical and charge transport properties as well as device performance of materials processed by green solvents remain to be further explored.

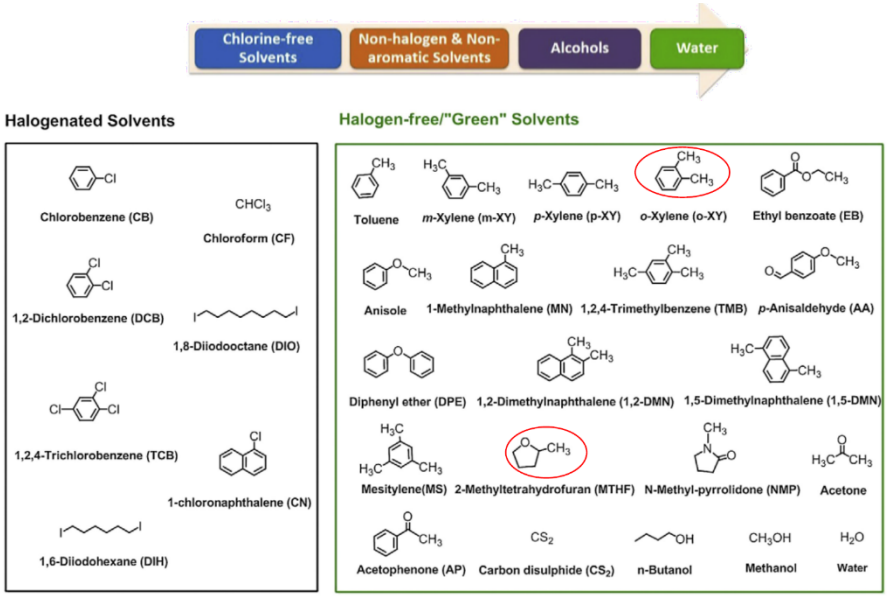

Figure 3-1: Chemical structures of commonly used solvents for OPV fabrication: halogenated solvents (left), halogen-free or 'green' solvents (right).

In this chapter, A series of small molecular non-fullerene acceptors (NFAs) with A-D-A and A-D'-D-D'-A structural frameworks have been synthesized in order to develop semiconductors with molecular structures tailored for solubility in polar media and efficient transport of charge carriers in the solid state. After characterized by solution NMR, MALDI-TOF mass spectra and Cyclic Voltammetry, NFAs' corresponding solubility in the chosen green solvent of 2Me-THF has been measured by UV-vis Spectroscopy. With the interest of comparing different conditions processed materials' neat films, Grazing-Incidence Wide-Angle X-ray Scattering (GIWAXS) and Atomic Force Microscope (AFM) has been applied to those synthesized new materials' pristine solid-state systems processed by different solvents. These studies use a family of molecules that allows for systematic dissection of structural components. To understand how molecular

conformation and dipole moment, calculated by computational simulation, affect the solubility in green solvents. And develop processing conditions to control molecular self-assembly in solution and thin film. We seek to understand the effects of molecular structures on their solubilities and furthermore establish structure-function-property-performance relationships for OSCs processed from green solvents.

3.2 Design and synthesis of NFAs probing structure-property relationships

Intrigued by the D-A co-polymers, non-fullerene acceptors (NFAs) have emerged as the next generation of electron acceptors in organic photovoltaics systems with 1) its higher light absorption compared with fullerene derivatives 2) well-defined optical and electrochemical properties 3) flexible synthetic procedures and structural frameworks leading to tunable solubility. Recently our group have developed narrow bandgap NFA of COTIC-4F, incorporating cyclopentadithiophene (CPDT), unit as the central donor (D) fragment, which is flanked by two alkoxythienyl units (D′) to form an electron rich D′-D-D′ central core. The D′-D-D′ units are end-capped with the electron deficient (A) unit 2-(5,6-difluoro-3-oxo-2,3-dihydro-1H-inden-1-ylidene) malononitrile, ultimately providing a A-D′-D-D′-A molecular configuration with the proper attributes to achieve the target intramolecular charge transfer (ICT) effect.[57]

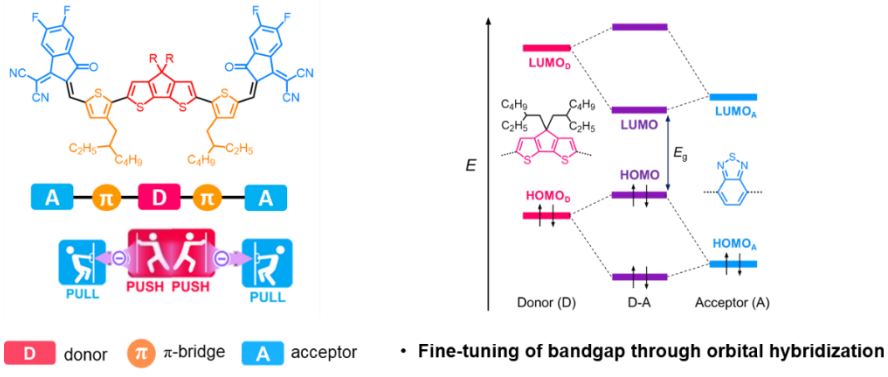

Figure 3-2: Molecular Design Strategy.

In this part of work, we have designed synthesized and characterized a family of A-D'-D-D'-A structured non-fullerene acceptors (NFAs) (**Figure 3-3**) utilizing the molecular design method (**Figure 3-2**) intrigued via the ultra-narrow bandgap NFA of COTIC-4F published by our group. With the modulation of center donor units with varied sidechains and the end-dye acceptors' halogenation substituents, these series newly designed NFAs present tailored solubilities and potential processability with 2-MeTHF.

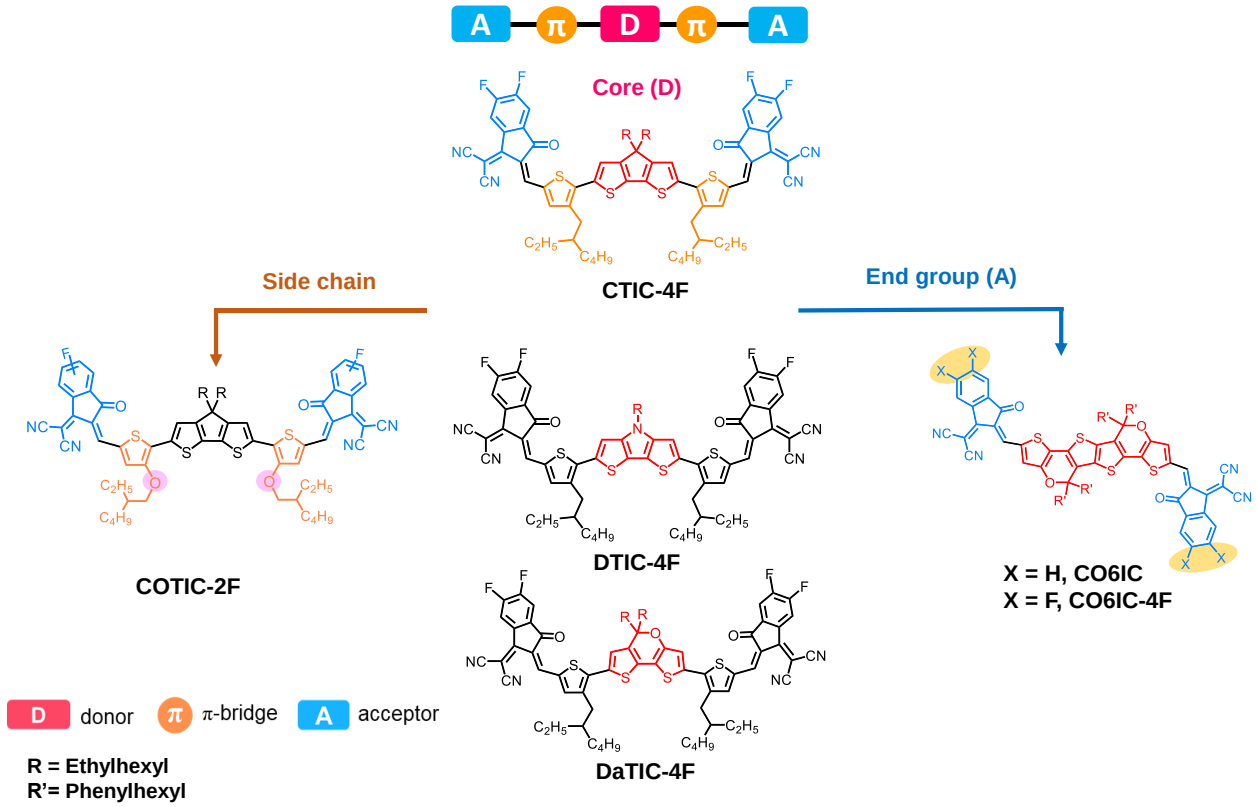

Figure 3-3: Chemical structures of A-D'-D-D'-A structured NFAs.

These series of NFAs are designed with the interest of comparing and investigating the core donor modification (CTIC-4F, DTIC-4F and DaTIC-4F), thiophene π-bridge (CTIC-4F and COTIC-2F) and end-dye acceptor motif (CO6IC and CO6IC-4F) effect on molecular properties thus resulting in different solubility and morphological properties.

3.3 Results and discussion

As shown in **Figure 3-4**, the synthetic routes of four central donor core units corresponding to CTIC-4F, DTIC-4F, DaTIC-4F, CO6IC and CO6IC-4F is presented (more detailed synthetic route is attached in section 3-5 of this chapter). After sidechain modifications by either nucleophilic substitution/ Pd(BINAP)-Catalyzed Amination/ Grignard reaction, center core donor units were obtained and then stannylated by n-BuLi and trimethyltin, followed by the Stille coupling reaction between corresponding stannylated donor core with 5-bromo-4-((2-ethylhexyl)oxy)thiophene-2-carbaldehyde (COTIC-2F) or 5-bromo-4-(2-ethylhexyl)thiophene-2-carbaldehyde (CTIC-4F, DTIC-4F and DaTIC-4F) in the presence of catalytic Pd(PPh3)4 in anhydrous toluene producing dialdehyde intermediates. Subsequently, Knoevenagel condensation reaction between dialdehyde intermediates and 2-(5,6-difluoro-3-oxo-2,3-dihydro-1H-inden-1-ylidene)malononitrile (CTIC-4F, DTIC-4F, DaTIC-4F and CO6IC-4F) or 2-(3-oxo-2,3-dihydro-1H-inden-1-ylidene)malononitrile (CO6IC) with a final yield around 70% within 6 substrates scope.

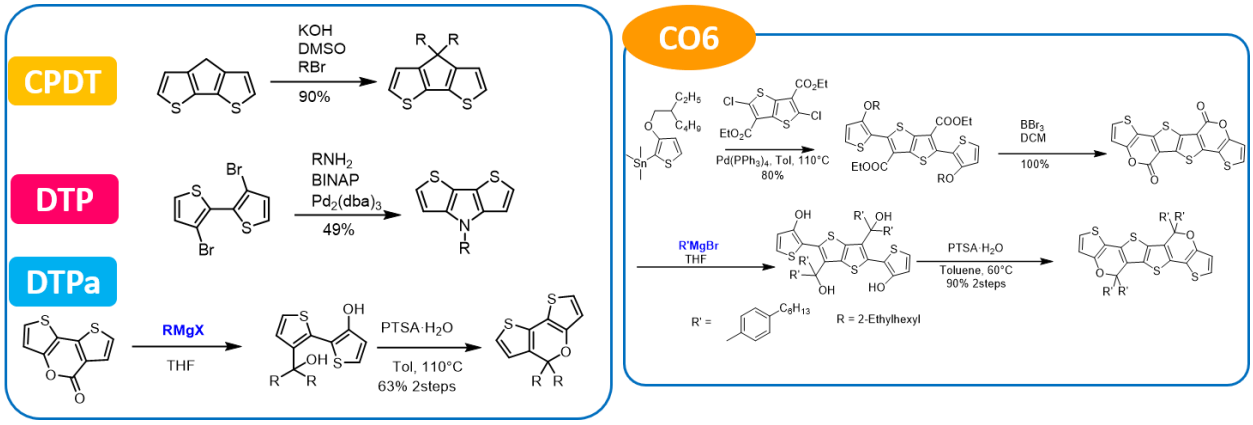

Figure 3-4: Synthetic Routes for Centre Donor of NFAs.

Cyclic voltammetry (CV) measurements were carried out in order to estimate molecular frontier orbital energy levels. The LUMO levels were deduced from the onsets of the reduction peaks and HOMO levels were calculated by the following equation: $E^{HOMO} = E^{HOMO} - E_g^{opt}$, where optical

bandgaps were measured by UV-vis spectroscopy and estimated by material's film absorption onsets.

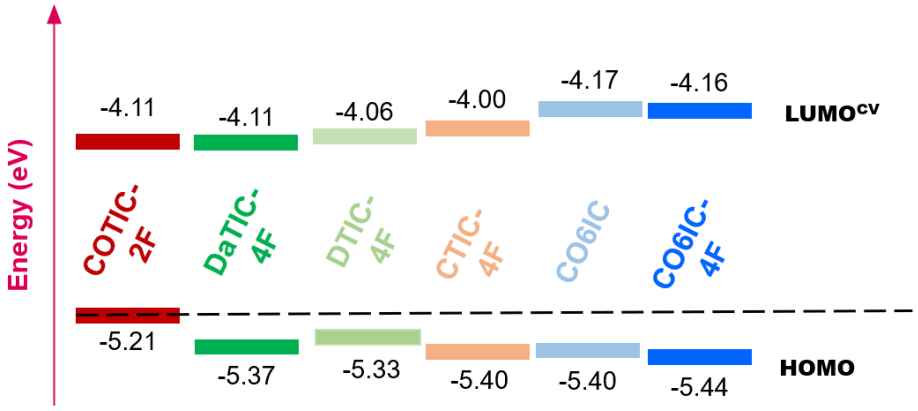

Figure 3-5: Energy Levels Diagrams for 6 NFAs estimated by CV and Optical Gap.

To experimentally quantify different materials' solubilities in the green solvent of 2-MeTHF, saturated solutions were prepared by stirring at 50℃ overnight, after filtering out un-dissolved material when solution was back to dissolving balance at room temperature, saturated solutions were with 100 to 10000 volumes of the same solvent to achieve an optical density suitable for absorption measurement.[101]Solubility value were calculated by measuring the optical density of the diluted solution and plugging measured absorbance to fitted calibration equation obtained by standard curves with known concentrations. The absorption curves are summarized in **Figure 2-6** and the solubility results are reported in **Table 3-1**.

Table 3-1: Solubilities and Calculated Dipole Moments summary

Acceptor	Solubility in 2-MeTHF	Theoretical Calculated Dipole Moment (Debye)
DaTIC-4F	37 mg/mL	4.568050
CO6IC-4F	23 mg/mL	1.567600
CTIC-4F	14 mg/mL	1.012300
COTIC-2F	15 mg/mL	2.084828
DTIC-4F	< 2mg/mL	1.685661
CO6IC	< 2mg/mL	1.567600

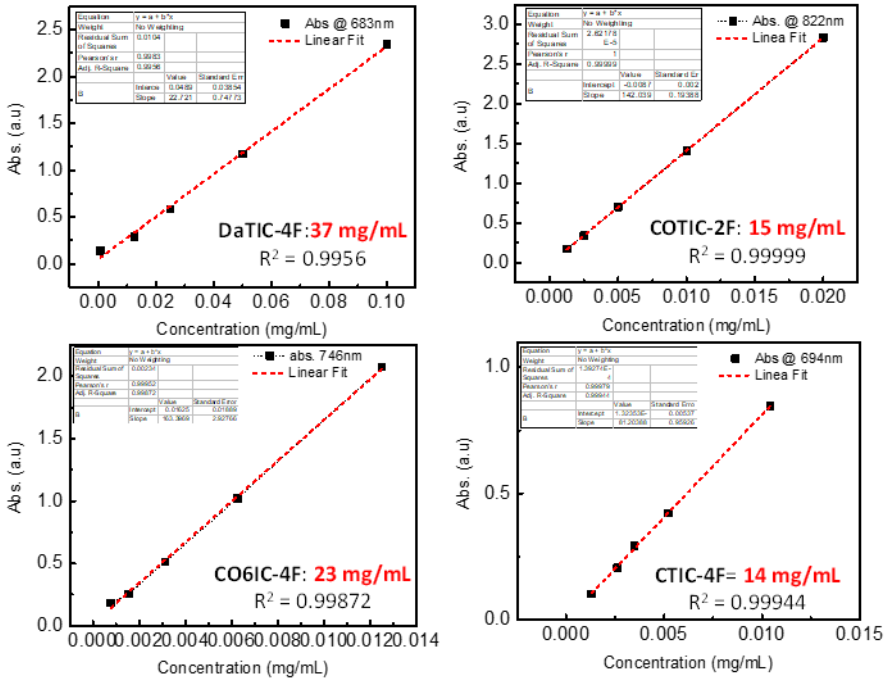

Figure 3-6: Calibration spectra used to calculate solubility number.

To obtain a deeper understanding of the observed trends of 6 NFAs' solubilities in 2-MeTHF, theoretical calculations were performed at the density functional (DFT) level of theory with the semi-empirically tuned LC-ωPBE/6-31G (d,p) functional and basis set to obtain the optimized molecular conformations and calculated dipole moment.[102]First geometry optimizations for newly designed A-D-A'-D-A ultra-narrow bandgap NFAs are done with the method of B3LYP/6-31G(d,p). Then the optimal ω values were determined based on the LC-ωPBE functional with the 6-31G(d,p) basis set. For the optimization of the range-separation parameter ω, all the single-point calculations were carried out for the N and N ± 1 systems using the default SCF convergence criteria in the Gaussian 09 code. After the concept of "optimal tuning" has been fulfilled, 2nd geometry optimization and time-dependent density functional theory (TDDFT) is applied to study the excited states of our large molecular systems.

Summarizing the solubility results for the organic semiconductors series, solubilities in 2-MeTHF increase with number of sidechains on center D units (CTIC-4F ~14mg/mL and DTIC-4F < 2mg/mL), furan-like core units (DaTIC-4F ~37mg/mL and CTIC-4F ~14mg/mL) and halogen substituents on the end-A units (CO6IC-4F ~23mg/mL and CO6IC < 2mg/mL). Moreover, For NFAs with center donor core modification (DaTIC-4F, CO6IC-4F and CTIC-4F), the experimental measured solubility in 2-MeTHF follows the same trend with calculated dipole moments, which could be accounted by single molecular dipole moments' positive relationship with corresponding materials' polarities. However, more factors need to be taken in to account for rationalizing the observed solubility results. For example, the halogen substituents atom on the End-dye acceptor units (CO6IC and CO6IC-4F) have apparent effect on material's solubility when NFAs share similar polarity, which could be accounted by molecular aggregation tendency's difference.

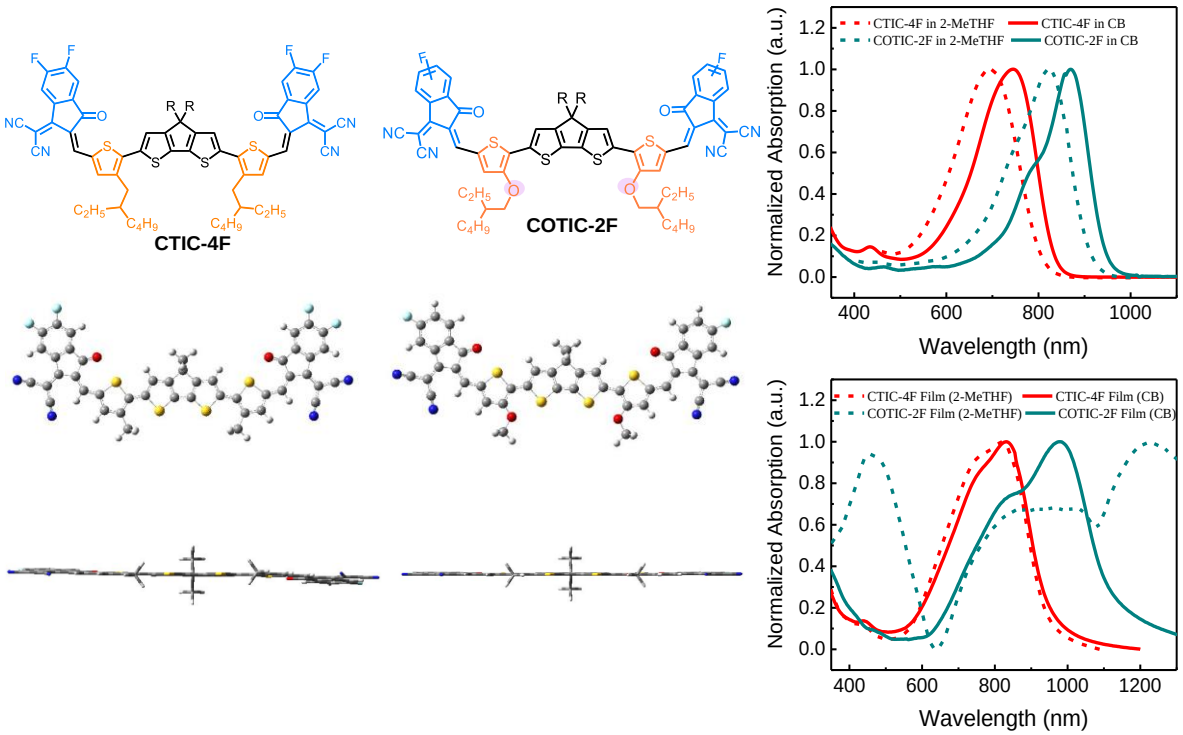

Figure 3-7: CTIC-4F and COTIC-2F chemical structures (top left); top and side-view of optimized geometries (bottom left) and normalized UV-vis Spectra of solutions (top right) and films processed by CB and 2-MeTHF (bottom right).

With the purpose of digging deeper into molecular structures' profound impacts on molecular optical, aggregation and morphological properties at the solid-state, characterizations of UV-vis Spectroscopy, GIWAS and AFM have been applied to three systems processed by a pair of solvents of CB and 2-MeTHF for comparison. And results discussion will be divided into three parts of 1) substituents effects 2) thiophene π-bridge and 3) central donor modifications. As shown in **Figure 3-7**, introducing the alkoxyl thiophene into the A-D'-D-D'-A system, COTIC-2F → CTIC-4F, leads to a red shift in the absorption maximum (λmax) from 744 to 875 nm in solution UV-vis in CB and also around 100nm redshift when changing solvent to 2-MeTHF. For the lack of conformational "locks" via S···O interactions involving proximate alkoxy groups and thienyl S atoms to favor coplanarity of the overall π - conjugated system,[50,103] CTIC-4F presents less planarity than COTIC-2F and blue-shifted absorption in film-state UV-vis spectra. The presence of COTIC-2F's secondary shoulder peak around 800nm also assists this hypothesis. There's subtle

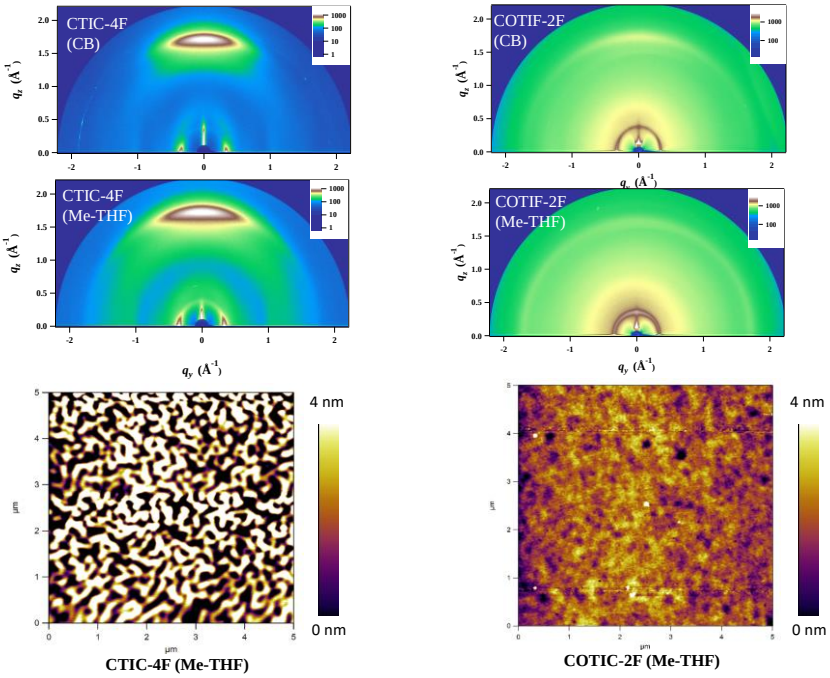

Figure 3-8: GIWAXS results (top) and AFM measurement (bottom) for CTIC-4F and COTIC-2F.

difference between CTIC-4F's film-state absorption spectra processed by two solvents, however, a new peak arises around 1200nm for COTIC-2F which might result from potential super molecular assembly when NFA is present in 2-MeTHF solution before drop-casting the film. Further characterizations on those NFAs films are summarized in **Figure 3-8** including GIWAXS and AFM measurement. CTIC-4F crystallites orient face-on relative to the substrate in both solvents processed films, while COTIC-2F presents relatively amorphous pattern in 2D-GIWAXS image. This result agrees with AFM imaging (**Figure 3-8**) where CTIC-4F has highly ordered networks akin to a metropolitan road network which is potential to efficient green solvent processed OSC system.[104] Future work to renationalize the COTIC-2F's large red-shift when processed by 2-MeTHF and understand its aggregation behavior should be planned for concentration and temperature dependent experiments.

A pair of C-O bridged laddered structured NFAs of CO6IC and CO6IC-4F with non-flouro and di-flouro substituents on the end-capping acceptors respectively have been synthesized and the characterizations are shown in **Figure 3-9**. The solution UV-vis spectra demonstrate similar absorption peaks around 800nm for both NFAs which means change on the halogen atoms of CO6 NFAs have few effects on intermolecular charge transfer (ICT) resulting in close optical gap (1.23eV and 1.28 eV for CO6IC-4F and CO6IC). And as expected, the molecular polarity, revealed by calculated dipole moments share no difference for this pair of molecules structural similarity. It has been reported that single methoxy group introduced on the end-group phenyl and varied its substitution position in ITIC derivatives can significantly impact the electron mobility of neat material's films as well as the device performance in BHJ OSCs.[105]The combined effects of the methoxy position on the intermolecular packing densities and electron-transfer rates by theoretical simulation are fully consistent with the experimental evolution of the electron mobilities.[106]

Therefore, the solubility difference between CO6IC-4F and CO6IC molecules could be accounted by the intermolecular packing greatly influenced by flouro-substituent and higher aggregation tendency for CO6IC small molecule.

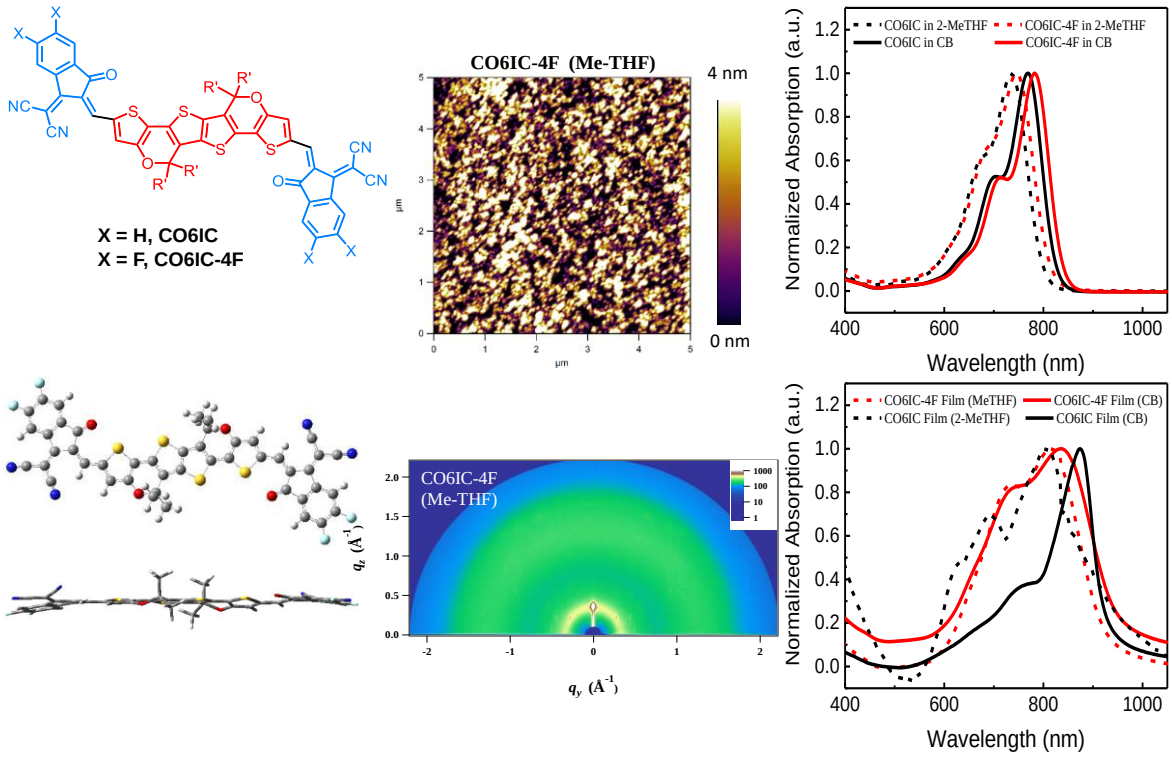

Figure 3-9: CO6IC and CO6IC-4F chemical structures (top left); top and side-view of optimized geometry (bottom left); films characterization of CO6IC-4F processed by 2-MeTHF (center) and normalized UV-vis Spectra in CB and 2-MeTHF (right).

Having investigated the substituent's influence of thiophene π-bridge and end-A fragments, we move forward to examining the center-D units variations by synthesizing and characterizing the three systematically changed NFAs (CTIC-4F, DaTIC-4F and DTIC-4F) which simply differs in the single atom within the central donor units. And we keep the alkyl-substituted thiophene bridge as well as fluorinated IC end groups. As shown in **Figure 3-5** and **Figure 3-10**, modification in the center-D affects barely on the LUMO levels of NFAs, but the red-shifted absorption spectra from CTIC-4F→DTIC-4F→DaTIC-4F and the consequently narrowed bandgap demonstrates the increased electron-donating capability from CPDT→DTP→DTPa. Regarding the lack of

conformational locks via S···O interaction, the rotational single bond connecting the center-D and end-A planar give rise to the broad single absorption peak in two solvents. It is worth noting that because of the asymmetry nature of DTPa core, overall molecular polarity has been enhanced and conformational planarity is obstructed thus presenting a 'banana shape' slightly twisted optimized single molecular geometry for DaTIC-4F. And all factors mentioned above bring about the growing solubility tendency in 2-MeTHF from DTIC-4F→CTIC-4F→DaTIC-4F (**Table 3-1**).

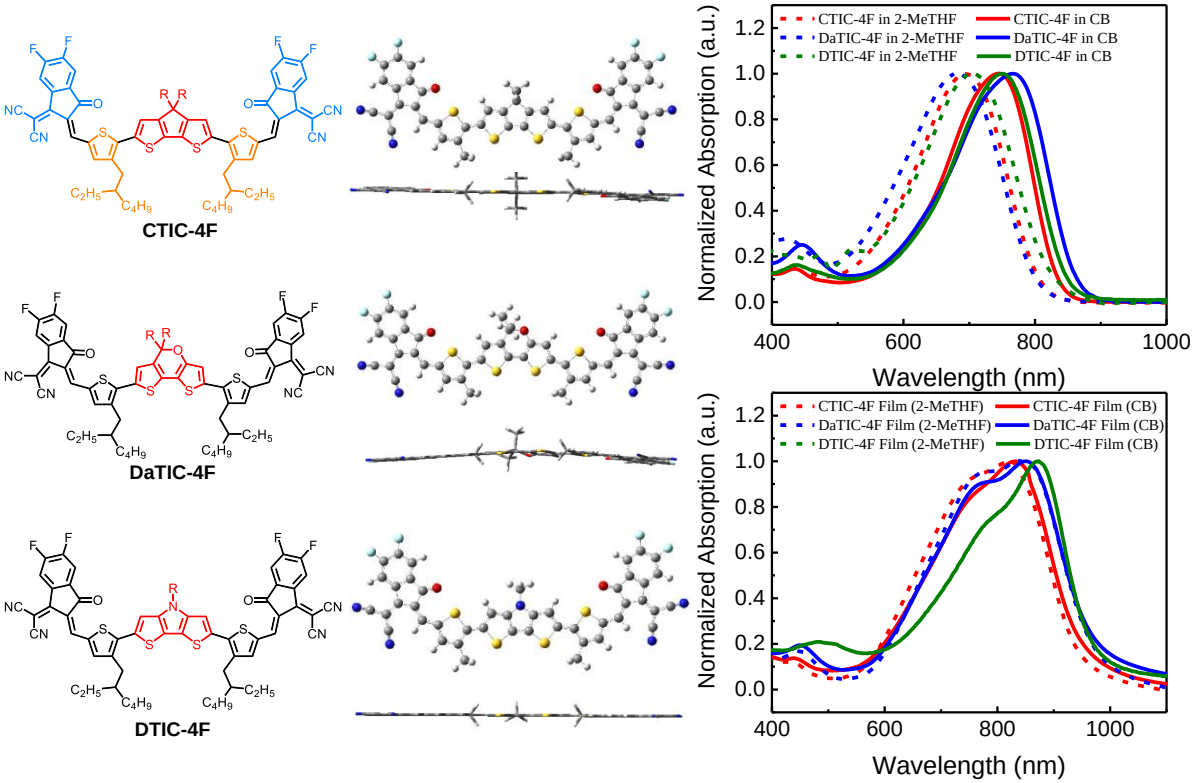

Figure 3-10: CTIC-4F DaTIC-4F and DTIC-4F chemical structures (left); top and side-view of optimized geometries (center) and normalized UV-vis Spectra of solutions (top right) and films processed by CB and 2-MeTHF (bottom right).

The surface topography of three NFAs' neat films prepared by 2-MeTHF were characterized by AFM. As presented in **Figure 3-11b**, the AFM height images indicate that all the CTIC-4F, DTIC-4F and DaTIC-4F films have smooth surface features with decreased root-mean-square (RMS) roughness of 2.48, 1.81, and 1.12 nm, respectively. The 2D GIWAXS patterns of CTIC-

4F and DaTIC-4F are shown in **Figure 3-11a**. As stated earlier in this report, the high intensity peak (010) located at qz = 1.77 $Å^{-1}$ of the CTIC-4F thin film prepared by CB indicated a face-on orientation of backbones on the substrate, whereas OOP (100) diffraction peaks located at qz = 0.35 $Å^{-1}$ of DaTIC-4F's film prepared from CB implies the edge-on orientations. Interestingly, when changing the processing solvent from CB to 2-MeTHF, the intensity of (010) peak in CTIC-4F film was enhanced and a new (010) peak in DaTIC-4F appeared at qz = 1.76 $Å^{-1}$ indicating the enhanced π-π stacking of CTIC-4F and DaTIC-4F at thin-film states.

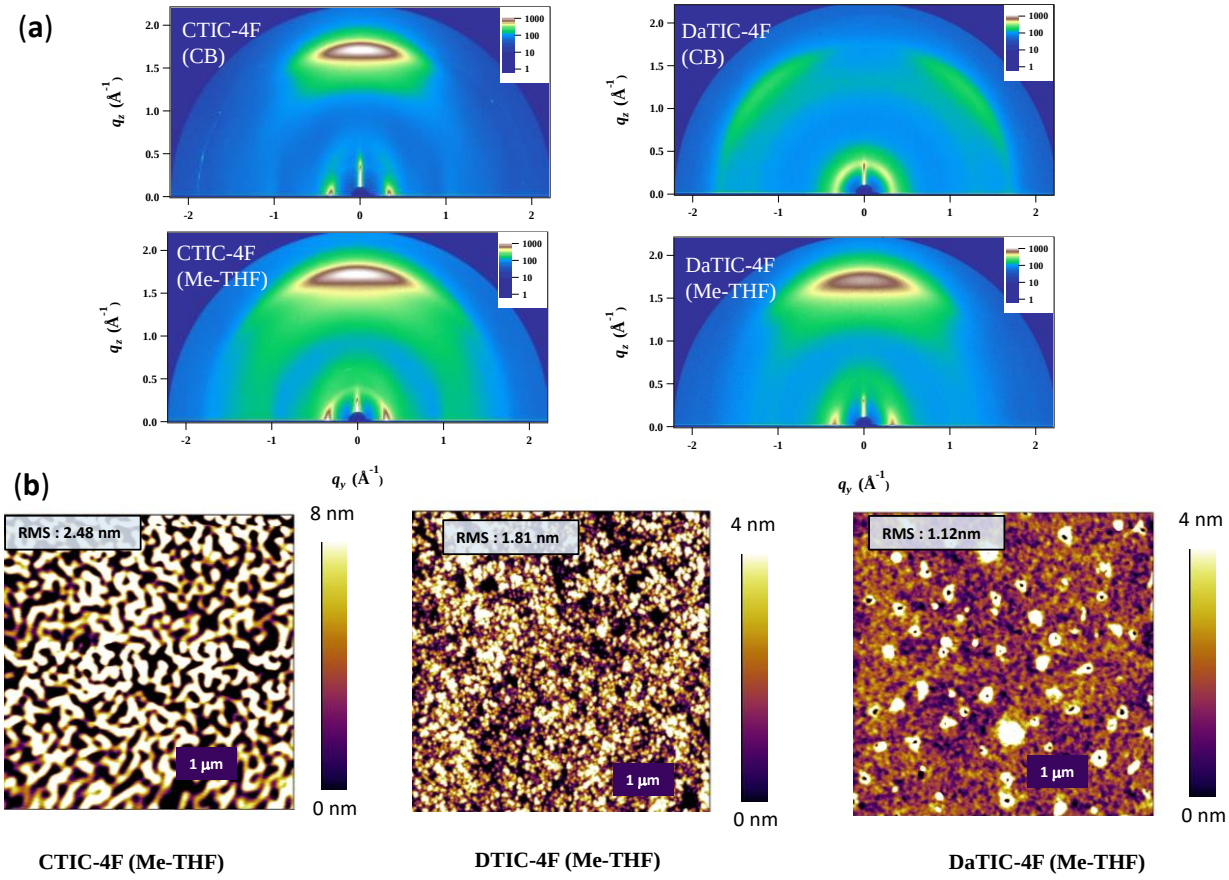

Figure 3-11: a) 2D GIWAXS patterns of DTIC-4F and DaTIC-4F thin films casted from CB and 2-MeTHF b) AFM imaging of CTIC-4F, DTIC-4F and DaTIC-4F.

3.4 Conclusions

A family of A-D'-D-D'-A structured NFAs presenting high solubilities and potential processability with 2-MeTHF have been designed, synthesized, and characterized by UV-vis spectroscopy AFM and GIWAXS. NFAs' solubilities in 2-MeTHF were measured and an increasing trend with number of sidechains, halogen substituents within end-dye acceptors and furan-like constructing units have been observed. The computationally simulated single molecular dipole moments and molecular geometry help with accounting for the solubility trends. Further thin-film characterization of GIWAXS results reveal that π-π stacking of CTIC-4F and DaTIC-4F is enhanced when processed by 2-MeTHF compared to films prepared from CB, which indicates that these 2 NFAs are potential good candidate towards efficient green solvent processed OPV systems. Future direction for this continued work will be investigation into charge transport of films prepared from 2-MeTHF and CB and examination of the molecular size and shape effects on solubility and molecular packing.

3.5 Experimental method

Materials All reagents and chemicals were purchased from commercial sources and used without further purification. All anhydrous organic solvents for the synthesis, characterization, and device fabrication steps were purchased from Sigma-Aldrich and TCI. Compounds **5** was purchased from 1 Materials Inc. Compound **1, 2**, **3**, **M1** and **M2** were prepared *via* a modified synthetic condition from literature.[107] Compound COTIC-2F, CTIC-4F were synthesized via conditions from literature.[50] For synthesis of DaTIC-4F, please refer to chapter 4 of this thesis.

Calculation methods The optimized structures, energy levels, and HOMO and LUMO orbital distributions were calculated the density functional (DFT) level of theory, using the semi-

empirically tuned LC-ωPBE/6-31G(d,p) functional and basis set. The simulated absorption peak wavelength pf designed molecules were calculated via time-dependent DFT simulation method. To simplify calculations, the alkyl chains were replaced with methyl or ethyl chains. The HOMO and LUMO levels were calculated by determining the difference in energy from the optimized ground state geometry of the cation and anion, respectively.[90]

Characterizations of compounds ^{1}H and ^{13}C NMR spectra of intermediate monomers were recorded on a **Varian Unity Inova 500 MHz spectrometer** in deuterated chloroform solution ($CDCl_3$) with 0.003%TMS as internal reference. Ultraviolet-Visible-Near-infrared (UV-Vis-NIR) absorption spectra were recorded on a Perkin Elmer Lambda 750 spectrophotometer. For the measurements of thin films, materials were spun coated onto precleaned glass substrates from chloroform solutions (10 mg mL^{-1}). Optical band gap was determined from the absorption onset of thin film sample.

Electrochemical characterization The electrochemical cyclic voltammetry (CV) was conducted on a CHI-730B electrochemistry workstation with glassy carbon disk, Pt wire, and Ag/Ag+ electrode as the working electrode, counter electrode, and reference electrode, respectively in a 0.1 M tetrabutylammonium hexafluorophosphate (*n*-Bu_4NPF_6) anhydrous acetonitrile solution at a potential scan rate of 40 mV s^{-1}. Thin films of samples were deposited onto the glassy carbon working electrode from a 3 mg mL^{-1} chloroform solution. The electrochemical onsets were determined at the position where the current starts to differ from the baseline. The potential of Ag/AgCl reference electrode was internally calibrated by using the ferrocene/ferrocenium redox couple (Fc/Fc^{+}).

Grazing incidence wide angle X-ray scattering (GIWAXS) analysis 2D GIWAXS measurements were performed using Beamline 9A at the Pohang Accelerator Laboratory (PAL). The photon energy is 11.055 keV (λ = 1.1214 Å). The angle between the film surface and the incident beam was fixed at 0.12° for all of the samples. The measurements were obtained at scanning intervals of 2θ between 3° and 25°. The 2D GIWAXS images from the films were analyzed according to the relationship between the scattering vector *q* and the *d* spacing, $q = 2\pi/d$. The GIWAXS images shown are normalized with respect to exposure time.

Material Synthesis

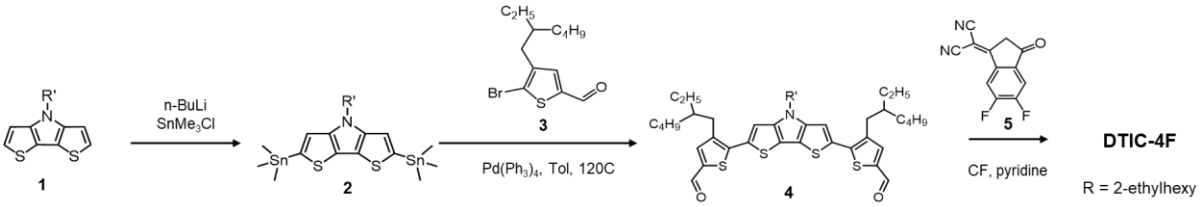

Compound **4**: A mixture of compound **3** (394mg, 1.3 mmol), compound **2** (320mg, 0.52 mmol), $Pd(PPh_3)_4$ (30 mg) and anhydrous toluene (20 mL) was added into a flame-dried and nitrogen-filled microwave tube in glovebox. The reactant was heated to 120 °C for 24 h. After the mixture cooled to room temperature, DI water was added, and the mixture was extracted with dichloromethane (50 ml x 3). The organic layer was dried over Na_2SO_4 and concentrated in vacuum. The crude product was purified by silica gel column chromatography (n-hex:EA=5:1, Rf = 0.5) to afford **4** as a dark red solid (260mg, 71%).

^{1}H NMR for compound **4** (500MHz, $CDCl_3$, ppm): δ 9.80 (s, 2H), 7.57 (s, 2H), 7.17 (s, 2H), 4.16–4.7 (m, 2H), 2.40-2.20 (m, 4H), 1.20-1.40 (m, 6H), 1.18–1.39 (m, 12H), 0.75–0.97 (m, 12H).

Compound **DTIC-4F**: A mixture of bisaldehyde intermediate **4** (90mg, 0.122mmol), 2-(5,6-difluoro-3-oxo-2,3-dihydro-1H-inden-1-ylidene)malononitrile (compound **5**, 96mg, 3.4eq), dry chloroform (20 mL), and pyridine was added into to a flame-dried and nitrogen-filled one-neck round-bottom flask The flask was purged with N_2 for 20 min and the reactant was heated to 60 °C for 12 h. After the mixture cooled to room temperature, the reaction mixture was concentrated in vacuum. The residue was purified by silica gel column chromatography to afford **DTIC-4F** as dark blue solid.

^{1}H NMR for compound **DTIC-4F** (500MHz, $CDCl_3$, ppm): δ 8.72 (s, 2H), 8.5-8.53 (m, 2H), 7.59-7.70 (m, 2H), 7.38 (s, 2H), 4.02–4.20 (br, 2H), 2.80-2.90 (m, 4H), 1.20-1.40 (m, 6H), 1.18–1.39 (m, 12H), 0.75–0.97 (m, 12H).

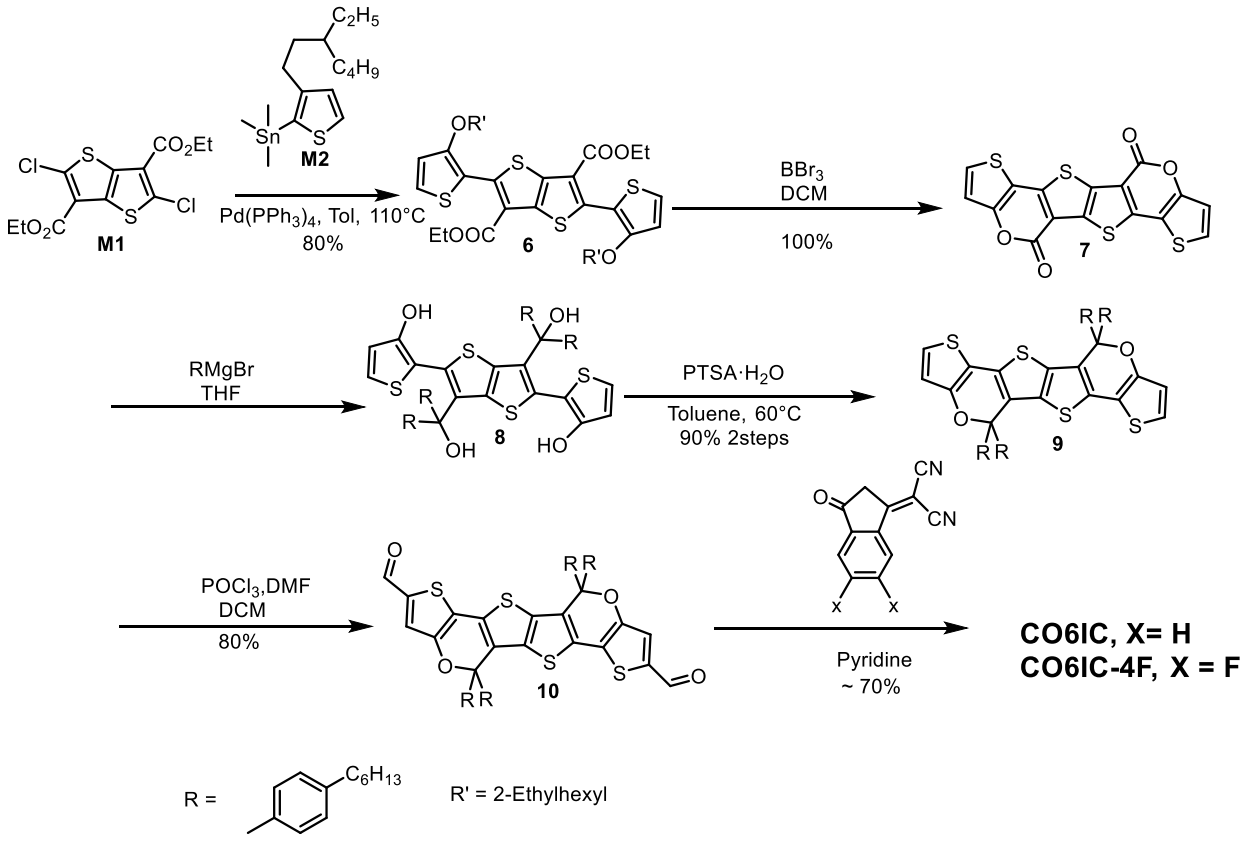

Compound **6**: A mixture of M1 (100mg, 0.28 mmol), compound M2 (378mg, 1 mmol), Pd(PPh3)4 (20 mg) and anhydrous toluene (20 mL) was added into a flame-dried and nitrogen-filled microwave tube in glovebox. The reactant was heated to 120 °C for 24 h. After the mixture cooled to room temperature, DI water was added, and the mixture was extracted with dichloromethane (50 ml x 3). The organic layer was dried over Na_2SO_4 and concentrated in vacuum. The crude product was purified by silica gel column chromatography (n-hex:DCM=1:1, Rf = 0.4) to afford 6 as a pale yellow solid (166mg, 80%).

^{1}H NMR for compound **6** (500MHz, $CDCl_3$, ppm): δ 7.32-7.34 (d, 2H), 6.89 (d, 2H), 4.31-4.37 m, 4H), 3.95(d, 4H), 1.55 (br, 6H), 1.22-1.37 (m, 14H), 0.78–095 (m, 12H).

Compound **7**: To a solution of compound 6 (240mg, 0.3mmol) in dry DCM (10 mL), BBr_3 (1.9mL 6eq) was added at low temperature under protection of inert gas Ar. After reaction warms and and keep stirring at room temperature for 2h, track the reaction. Annulation was conducted directly after deprotection. No information for the ^{1}H NMR since the obtained brownish yellow solid is not soluble in most of the common organic solvent. Compound 7 was directly used for the next step of reaction.[108]

Compound **8**: To completely dried compound 7 (150 mg, 0.38 mmol), (4-hexylphenyl)magnesium bromide (3.8 mmol) was added at room temperature under argon. The mixture was stirred at 60℃ overnight. After cooling to room temperature, the reaction mixture was poured into icy water followed by extraction with DCM for three times and NH_4Cl for one time. Orange red product mixture was dried under vacuum before directly used for the next step.

Compound **9**: The residue od compound 8 was dissolved in anhydrous toluene solvent (20mL), and p-toluenesulfonic acid (148mg) was added. The mixture was stirred at room temperature for

several hours before TLC tracking the completion of reaction. DI water was added, and the mixture was extracted with dichloromethane (50 ml x 3). The organic layer was dried over Na_2SO_4 and concentrated in vacuum. The crude product was purified by silica gel column chromatography using CF to afford 9 as yellow solid (370mg, 73%).

^{1}H NMR for compound **9** (500MHz, $CDCl_3$, ppm): δ 7.32-7.34 (d, 2H), 6.89 (d, 2H), 4.31-4.37 (m, 8H), 3.95(d, 8H), 1.55 (br, 6H), 1.22-1.37 (m, 24H), 0.78–0.95 (m, 12H).

Compound **10**: To a mixture of $POCl_3$(0.71 mL) and DMF (0.35 mL), 20 mL DCM was added after removing H_2O and O_2. Leave reaction stirring at 0° for 30min, then a solution of compound 9 (316 mg, 0.316 mmol) was added in the mixture. The reaction was heated to reflux overnight, giving a red solution. The reaction was quenched via water and stirred for another 30min before extraction with DCM. The crude product was purified by silica gel column chromatography TLC (DCM:Hex=1.5:1) Column (DCM:Hex=1:1) and sticky orange solid was obtained.

^{1}H NMR for compound **9** (500MHz, $CDCl_3$, ppm): δ 9.67 (s, 2H), δ 7.34 (s, 2H), 7.17(m, 8H), 7.27 (m, 8H), 2.63 (t, 8H), 1.62(m, 8H), 1.26-1.35 (m, 24H), 0.84–0.91 (m, 12H).

Compound **CO6IC-4X**: A mixture of bisaldehyde intermediate **9**, 2-(5,6-difluoro-3-oxo-2,3-dihydro-1H-inden-1-ylidene)malononitrile (compound **5**), dry chloroform (20 mL), and pyridine was added into to a flame-dried and nitrogen-filled one-neck round-bottom flask The flask was purged with N_2 for 20 min and the reactant was heated to 60 °C for 12 h. After the mixture cooled to room temperature, the reaction mixture was concentrated in vacuum. The residue was purified by silica gel column chromatography to afford **CO6IC-4x** as dark blue solid.

^{1}H NMR for compound **CO6IC** (500MHz, $CDCl_3$, ppm): δ 8.70 (s, 2H), δ 8.65 (d, 2H), δ 7.85 (d, 2H), δ 7.74 (m, 2H), δ 7.7 (m, 2H), δ 7.52 (m, 2H), δ 7.40 (s, 2H), 7.16-7.72 (br, 16H), 4.26–4.17 (br, 2H), 2.62-2.70 (m, 4H), 1.60-1.70 (m, 6H), 1.22–1.40 (m, 12H), 0.79–0.90 (m, 12H).

^{1}H NMR for compound **CO6IC-4F** (500MHz, $CDCl_3$, ppm): δ 8.67 (s, 2H), δ 8.51 (m, 2H), δ 7.61 (t, 2H), δ 7.42 (s, 2H), δ 7.17-7.27 (m, 16H), 2.67 (m, 8H), 1.54-1.72 (m, 8H), 1.21-1.43 (br,24H), 0.75–0.92 (m, 12H).

Chapter 4: Toluene Processed Semitransparent Optoelectronic Devices Based on Narrow Bandgap Composition

4.1 Introduction

Organic semiconductors have drawn intense research interest because of their ultra-thin film processibility, synthetic flexibility, and potential industry applications through low-cost solution based techniques.[45,109–113] Their structural versatility allows tuning of optical gaps for specific applications. In the area of optoelectronics based on organic semiconductors, the concentration of development has shifted to fullerene-free acceptors since few years ago for further attractive applications not only enhancing device performance.[27,114] The non-fullerene acceptors (NFAs) in bulk heterojunction (BHJ) photoactive films is one of key factors to determine the performance of optoelectronic devices including organic solar cells (OSCs) and organic photodetectors (OPDs).[115,116] Most NFAs reported recently have narrower optical bandgap, which indicates that they can absorb more photons up to in range of Near-infrared (NIR) wavelength. Composition of narrow bandgap NFAs and wide bandgap donors have achieved high performance by 18% power conversion efficiency of OPVs and 1.42×10^{13} Jones of OPDs due to broaden light absorption and increased photocurrent.[117,118] Near-infrared (NIR) responsive organic solar cells (OSCs) can form the basis of future applications such as semitransparent energy producing devices for building-integrated or green house systems, together with developing dichroic semitransparent electrodes.[119–122] With a similar working principle to OSCs, on the other hand, two terminal-based organic photodetectors (OPDs) with NIR responsivity are beneficial to next generation applications that include image sensing, night surveillance, optical communication, health and biomedical monitoring.[123,124] Hence, not only the flexibility in molecular design with the extensive

knowhow on the functions for modulating energy levels and morphological features on heterojunction (BHJ) but also the strategy of material composition is essential to accelerate the development of NIR OPDs.

The interaction of solvents and BHJ components has a significant effect on the film morphology and blend self-assembly.[125,126] Except for achieving high efficiency in fullerene-free optoelectronics with halogenated solvents, there is substantial focus on green solvent processing in device fabrications process for industrial scale of commercial market.[127,128] Typically, the toxicity of common organic halogenated solvent (chlorinated solvents, such as chloroform (CF), chlorobenzene (CB), dichlorobenzene (DCB), and so on) widely used in organic semiconductors processing process are less desirable. Chlorine-free solvents such as toluene and tetrahydrofuran (THF) were preferentially chosen for green solvent-based organic optoelectronics.[129] For toluene-based OSCs, Maojie Zhang's group reported a high performance of 13.1% power conversion efficiency from PM7:IT-4F blend in 2018.[130] For THF solvent-based OSCs, Jianhui Hou's group reported an efficiency of 12.1% with doctor blading processed PBDB-BzT:IT-M blend.[131] Both groups presented higher device performance of green solvents than one of chlorinated solvents resulted from enhanced current density.

In our previous work, we've developed the CTIC-4F NFA with Eg of ~1.30 eV, a A−D'−D−D'−A molecular configuration based on an electron rich core comprising of cyclopentadithiophene (CPDT) as the central donor (D) unit and alkylthienyl units as the flanking donor (D') fragments, followed by capping with the acceptor (A) units of 2-(5,6-difluoro-3-oxo-2,3-dihydro-1H-inden-1-ylidene)malononitrile (IC-2F). CTIC-4F was reported with the specific detectivity (D*) of 7.0×10^{11} Jones with peak around 830 nm at zero-bias and the power conversion efficiency (PCE) of 10.5% by blending with PTB7-Th donor polymer for active layer.[50] In this

contribution, an O-functionalized conjugated core unit was introduced to modify electron donating ability for broadening absorption and bandgap. On the other hand, halogen atoms (F, Cl) on the end group could attribute to the auxochromic effect of molecule and they simultaneously downshift energy levels.[132] In particular, chlorine atom on molecule such as Cl···S and Cl···π interactions showed stronger noncovalent interactions than fluorine atom, since empty 3d orbitals of fluorine atom can accept the electron pairs or π electrons on the molecule, which can improve intermolecular interaction.[111,132–134] Thus, a few strategies can be employed to modulate the electrical and optical characteristics.

In this contribution, we designed and synthesized a series of narrow band gap NFAs, DaTICs, see **Figure 4-2a**. Then, we examined the impact of end-dye acceptors engineering on the optoelectronic properties of NFAs built on the DaTIC conjugated framework. Those originally developed NFAs were furthermore applied into OSCs and OPDs processed by both chlorobenzene and toluene. The incorporated donor was the previously reported polymer PM2, which is promising for implementation of transparent devices due to its broadened absorption up to 900 nm. Toluene solvent-based devices had higher photocurrent and thus output of organic optoelectronic due to the bicontinuous film morphology and the efficient phase separation. Finally, we fabricated the green solvent based semitransparent devices with thin Au top electrode, resulting in accomplishing the high detectivities of 2.75×10^{13} Jones at maximum wavelength at zero bias in PM2:DaTIC-4Cl blend system.

4.2 Results and discussion

4.2.1 Molecular design and characterization

The synthetic routes of the new NFAs are depicted in **Figure 4-1**. The series of molecules DaTIC-4X were synthesized through Stille coupling reaction between compound 3 and 5-bromo-4-(2-ethylhexyl)thiophene-2-carbaldehyde (4) in the presence of $Pd(PPh_3)_4$ in anhydrous toluene, followed by end-capping with IC-2X (6) where X represents hydrogen, fluorine, or chlorine substituents. The synthetic routes of IC-2X and characterization of intermediates have been summarized in the experimental methods section.

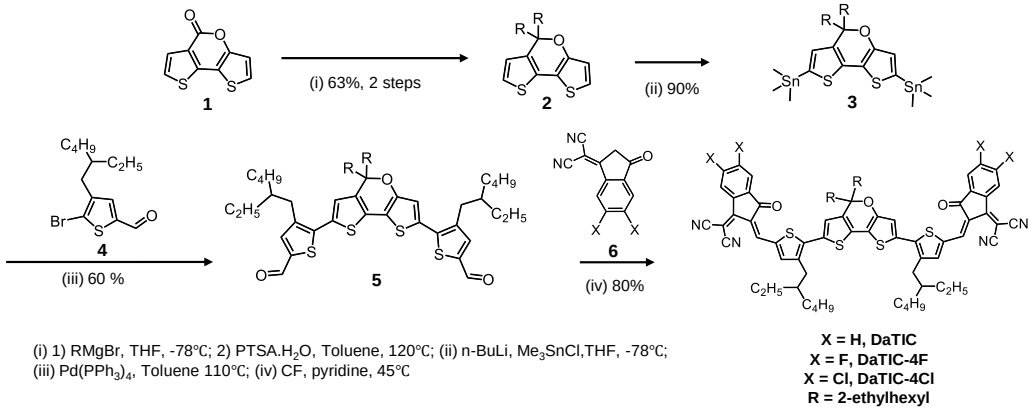

Figure 4-1. Synthetic route for DaTIC derivatives.

Table 4-1. Optical properties and estimates of frontier energy levels of PM2, DaTIC derivatives

compound	$\lambda_{f,max}$ (nm)[a]	E_g^{opt} (eV)[b]	E_g^{CV} (eV)[c]	E_{HOMO} (eV)[d]	E_{LUMO} (eV)[e]
PM2	794	1.41	-	-5.04	-3.63
DaTIC	815	1.33	1.52	-5.50	-3.98
DaTIC-4F	851	1.26	1.26	-5.38	-4.12
DaTIC-4Cl	886	1.18	1.21	-5.37	-4.16

Absorption maximum in thin films[a]. [b]Optical band gap calculated from the absorption edge of thin film. [c]Electrochemical band gap obtained from the CV. [d]HOMO energy level estimated from the onset oxidation potential. [e]LUMO energy level estimated from the onset reduction potential.

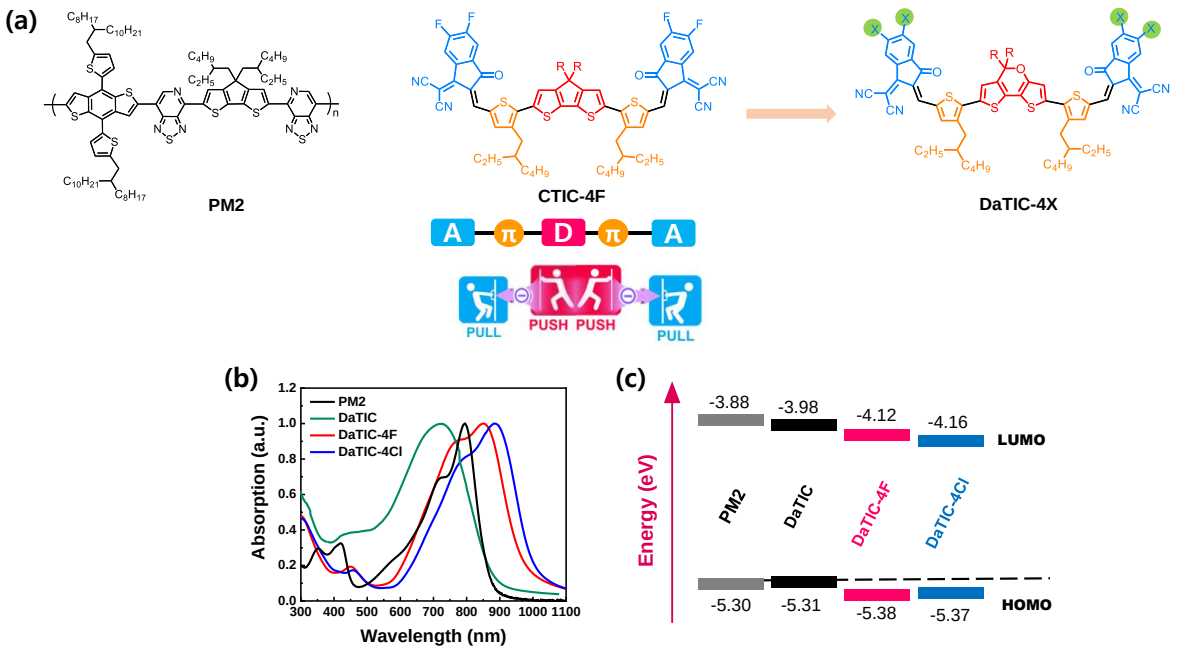

Figure 4-2. (a) Chemical structure of molecules. (b) Neat film UV-vis absorption spectra, (c) energy level diagram of molecules.

Solid state absorption spectra of NFAs are shown in **Figure 4-2b,** and materials' optical and electrochemical properties are summarized in **Table 4-1**. In CF solution, the absorption maximum (λ_{max}) redshifts gradually from 815 to 851 to 886 nm, accompanied by increasing maximum molar extinction coefficients, as the substituents vary from H to Cl. From the solution to the film state, redshifts ~100 nm for three NFAs can be observed. Optical transitions of NFAs are located in the NIR region with Eg^{opt} of 1.30, 1.26, and 1.18 eV for DaTIC, DaTIC-4F, and DaTIC-4Cl, respectively. Cyclic voltammetry (CV) measurements were carried out to estimate orbital energy levels. HOMO and LUMO levels were deduced from the onsets of the oxidation and reduction peaks, respectively. The HOMO/LUMO energy levels of DaTIC, DaTIC-4F, and DaTIC-4Cl were determined to be −5.36/−4.04, −5.38/−4.12, and −5.37/−4.16 eV, respectively (**Figure 4-2c**). Incorporation of chlorine atom at the end-dye acceptor enlarges the density of π-electrons on the conjugated backbone and thus downshifts the HOMO energy levels. Our previous study revealed that PTB7-Th:COTIC-4F-based solar cells generate photocurrents in the NIR region despite a

small HOMO−HOMO energetic offset between PTB7-Th and COTIC-4F. Since DaTIC-4F and DaTIC-4Cl possess lower HOMO energy levels relative to that of COTIC-4F, and the new donor polymer of PM2 has relatively deep HOMO level, it is anticipated that efficient charge generations can occur from both NIR-absorbing NFAs when blending with PM2.

To figure out the influence of the halogenated substituent of end group on the optoelectronic performance in the new designed molecules, the two terminal-based photomultiplication type organic devices were fabricated with architecture configuration of Indium tin oxide (ITO)/zinc oxide (ZnO)/PM2:DaTICs/MoO_3/Ag (see **Figure 4-3a)**, wherein the active solutions were mixed two components as 1:1.5 (D:A) ratio of a PM2 and a DaTIC-2X with 25 mg/ml concentration. To implement semitransparent optoelectronic devices such as organic solar cells and organic photodetectors for next-generation applications, PM2 donor polymer was selected because of its outstanding properties including the narrow optical bandgap of 1.41 eV, absorbance upto around 900 nm and stable high performance. The chemical structure of PM2 polymer are shown in **Figure 4-2a** together with the new designed DaTIC-2X NFAs. The two semiconducting components for binary photoactive films were dissolved in each two solvents, one was chlorobenzene as a chlorinated prevailing organic solvent and the other was toluene as an environmentally benign solvent. Detailed information of device fabrication is described in the experimental section. **Table 4-2** and **Figure 4-3** shows the performance both organic solar cells and organic photodetectors. Since these two devices have similar working mechanism and device structure, two functions of an optoelectronic device can be selectively used depending on the purpose of the device applications. Photovoltaic parameters were derived from the fourth quadrant of *J-V* curve, in this study, while, figures of merit for photodetectors were obtained from characteristic at zero external bias under both illumination and dark condition as a self-powered operation mode.

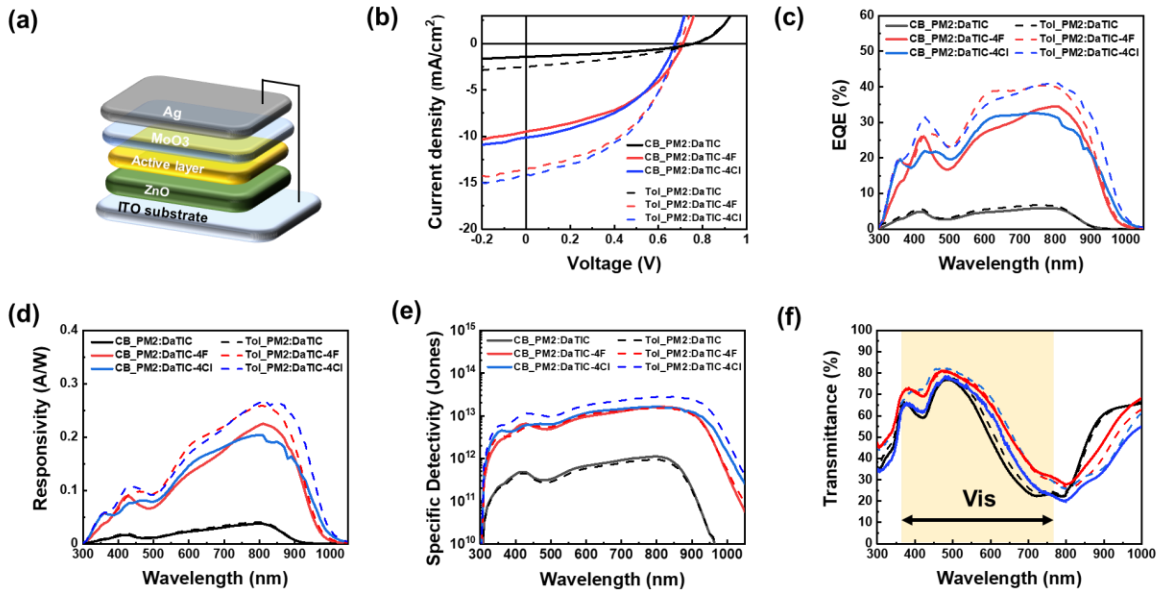

Figure 4-3. (a) device structure, (b) *J-V* curve, (c) EQE spectra of photo devices measured at zero bias, (d) spectra of responsivity and (e) specific detectivity based on the photocurrent measured at short circuit condition and (f) transmittance spectra of films based on ZnO/PM2:DaTICs blends.

Table 4-2. Photovoltaic performances of OSCs based on PM2 and DaTIC NFAs measured under simulated 100 mW cm^{-2} AM 1.5G illumination and Photodetector performances estimated from dark current and external quantum efficiency (EQE).

Donor	**Solvent**	**Acceptor**[a]	**J_{SC} (mA/cm²)**	**V_{OC} (V)**	**FF**	**PCE**[b] **(%)**	**Responsivity @λ_{max}**	**Specific Detectivity* (Jones @0 V)**
PM2	CB	DaTIC	1.95	0.81	0.37	0.58	0.041@800	9.41×10^{11}
		DaTIC-4F	9.49	0.71	0.44	2.98	0.23@810	1.67×10^{13}
		DaTIC-4Cl	10.12	0.67	0.45	3.08	0.20@825	1.64×10^{13}
	Toluene	DaTIC	2.03	0.82	0.37	0.61	0.037@800	1.10×10^{12}
		DaTIC-4F	13.50	0.70	0.44	4.29	0.26@810	1.60×10^{13}
		DaTIC-4Cl	14.11	0.69	0.47	4.50	0.27@825	2.75×10^{13}

[a]PM2:acceptor blend ratios are 1:1.5 (w/w) in chlorobenzene (CB) and toluene (Tol). [b]These are best PCE values.

The performance of solar cells based on the non-halogenated molecule, PM2:DaTIC solar cells processed by both solvents, showed low photocurrent at short circuit condition due to the limitation of shorter range of light absorption by 900 nm as well as weaker light absorption. Which resulted

in significantly lower performance of less than 1% PCE arise from the current density (J_{sc}) of 1.95-2.03 mA/cm^2 and fill factor (FF) of 0.37 in both two solution cases, although open circuit voltages (V_{oc}s) were higher compared to V_{oc} parameters of two halogenated NFAs-based OSCs. In contrast, PM2:DaTIC-4F and PM2:DaTIC-4Cl OSCs exhibits a improved FF values with dramatically enhanced Jscs. In particular, PM2:DaTIC-4Cl OSCs achieved the highest current density and FF among them in each solvent cases, which indicate that the stronger electron withdrawing substituents on molecule related to superior charge transfer and upgrading crystallographic orientation of molecules. In addition, the highest occupied molecular orbital energies (ΔE_{HOMO}) offsets between PM2 and DaTIC NFA was almost negligible (<0.01 eV), which suppressed efficient charge generation in devices. While, adequate difference of $HOMO_D$-$HOMO_A$ offset like PM2:DaTIC-4F and PM2:DaTIC-4Cl devices contributed an sufficient driving force for exciton separation. The V_{oc} decrease along the introduction of halogen substituents can be roughly derived from their downshift LUMO energy levels of NFAs from DaTIC (-3.98 eV) to DaTIC-4F (-4.12 eV) to DaTIC-4Cl (-4.16 eV) corresponding to the energy difference between the HOMO of the polymer donor and LUMO of the acceptor with the other variables. For comparison between toluene and CB solvent, OSCs fabricated by toluene-based solutions for each active blend showed higher performance with slightly improved Voc and FF, in particular, the current density were significantly increased from 9.49 mA/cm^2 to 13.50 mA/cm^2 for OSC of PM2:DaTIC-4F blend and from 10.12 mA/cm^2 to 14.11 mA/cm^2 for device of PM2:DaTIC-4Cl blend, respectively. As expect, the difference of solvent solubility and film drying rate affect on film morphological phase and thus device performance, resulting that PM2:DaTIC-4Cl based OSCs showed the highest PCE of 4.50 % among OSCs fabricated with three NFAs and two different solvents.

Since the compositions with narrow bandgap of a Donor: new NFAs showed outstanding near - infrared photoelectric response, the devices were also explored to photodetection as two terminal photovoltaic mode. The figures of merit for OPD devices in this work were based and plotted under zero bias as a self-power mode. The responsivity (R), defines the conversion ability from light into electrical signals, can be calculated by the ratio of the photocurrent density by the incident optical power, and follows as :[135]

$$R = \frac{EQE \cdot e}{hv} \text{ (A/W)} \qquad (1)$$

In which e is elementary electron charge (1.6×10^{-19} C), h is plank constant, v is photon frequency. **Figure 4-3c** shows the responsivity of the devices of DaTIC, DaTIC-4F and DaTIC-4Cl based active blends. Maximum responsivities of the devices at zero voltage in were 0.037, 0.23 and 0.20 $A \cdot W^{-1}$ for DaTIC, DaTIC-4F and DaTIC-4Cl case fabricated by CB solvent, and 0.041, 0.26 and 0.27 $A \cdot W^{-1}$ for DaTIC, DaTIC-4F and DaTIC-4Cl based blends in toluene solvent, which were from at 800 nm, 810 nm and 825 nm for DaTIC, DaTIC-4F and DaTIC-4Cl, respectively.

In addition, the specific detectivity (D*), the sensitivity of a photodetector to optical signal, were calculated by the following **equation (2)** with assuming that the shot noise was major contribution of total noise under reverse bias.[135,136] here, we note that the equation is for the shot-noise-limited specific detectivity.

$$D^* = \frac{R\sqrt{A}}{\sqrt{2ej_d}} = \frac{R}{\sqrt{2eJ_d}} \quad (2)$$

Where J_d is dark current density, J_d is dark current density. The maximum D* (Jones) calculated for PM2:DaTIC, PM2:DaTIC-4F and PM2:DaTIC-4Cl based devices of toluene solution processing were 9.41×10^{11}, 1.67×10^{13} and 2.75×10^{13} Jones at each maximal wavelength, respectively, as shown in **Figure 4-3d**. Achieving a D* of over 10^{13} Jones of PM2:DaTIC-4Cl

based device in range of NIR (from 780 nm to 940 nm), notably, tentatively presented high potential of a strong NIR photon detection and minimal leakage current.

Furthermore, transmittance of active films composed of narrow bandgap donor and NFAs were measured as shown in **Figure 2e**. the average visible transmittances (AVT, 380 nm - 780 nm) were calculated according to the following **equation (3)**, which is the integration of the transmission spectrum and AM 1.5G photon flux weighted against the photopic response of the human eyes.[137]

$$AVT = \frac{\int T(\lambda)\cdot V(\lambda)\cdot AM1.5G(\lambda)d\lambda}{\int V(\lambda)\cdot AM1.5G(\lambda)d\lambda} \quad (3)$$

$T(\lambda)$ is the transmittance spectra and $V(\lambda)$ is the photopic response. As a result, the photoactive blend film of optimal PM2:DaTIC-4Cl device processed toluene solution showed higher AVT value of 73.65 %, comparing to the other films: (64.42 % of PM2:DaTIC, 72.06 % of PM2:DaTIC-4F), due to the red shifted absorbance of DaTIC-4Cl and less combined absorption of PM2:DaTIC-4Cl in around visible range. In addition, optimal films coated by CF solution case exhibited slightly lower AVT values than toluene-based films (61.12 % of PM2:DaTIC, 71.20 % of PM2:DaTIC-4F, 67.51 % of PM2:DaTIC-4Cl).

4.2.2 Film analysis

Grazing incidence wide-angle X-ray scattering (GIWAXS) measurement is used to characterize the molecular stacking and orientation in the thin organic film. **Figure 4-4** shows two-dimensional (2D) image of blend films and corresponding plotted line along q_z axis. GWIAXS result of neat molecule films and list of crystallographic parameters are shown in **Figure S1** and **Table S1** (see experimental and supplementary information section). Films of PM2:DaTIC, PM2:DaTIC-4F and PM2:DaTIC-4Cl showed (010) scattering pattern on q_z axis, indicating preferential face-on orientation. It was observed that scattering vector of films with halogen atom

on molecule shows shift toward longer, which ascribe that the π-π distance of adjacent molecules gradually reduced in order of hydrogen, fluorine and Chlorine substituents (PM2:DaTIC of 3.65-3.70 Å > PM2:DaTIC-4F of 3.63-3.65 Å > PM2:DaTIC-4Cl of 3.59-3.61 Å) in both solvent process. Additionally, the toluene-based films exhibited slightly reduced π-π distance with higher scattering vector compared to CB films. The tendency proved again that stronger noncovalent interactions between halogen atom and molecule skeleton lead to the planarity of molecule backbones and high-quality crystallization. The more compacted molecular crystallite in the photoactive layer arising from the effect of lower evaporation pressure solvent (CF) contributed to the enhancement of the photocurrent of devices. Morphology of photoactive films is crucial key parameter for device performance.

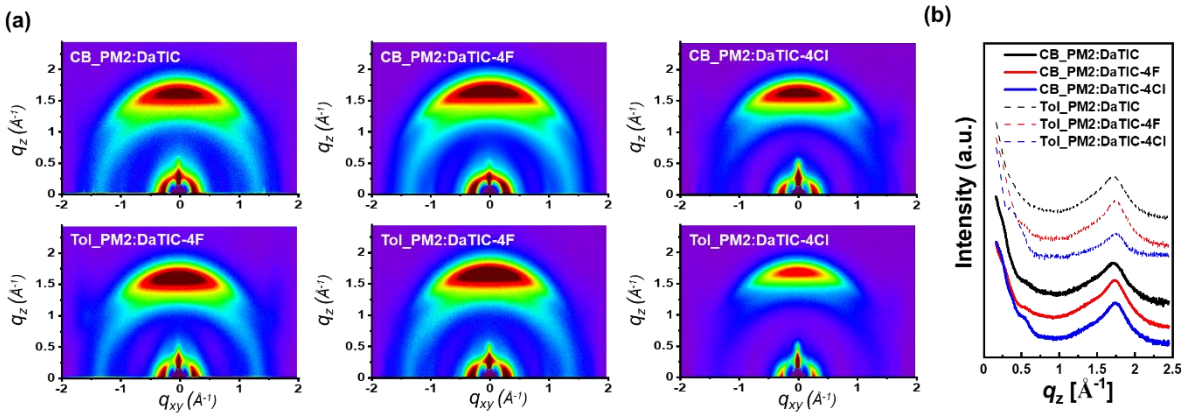

Figure 4-4. 2D GIWAXS images of (a) PM2:DaTIC (CB), PM2:DaTIC-4F (CB), PM2:DaTIC-4Cl (CB), PM2:DaTIC (Tol), PM2:DaTIC-4F (Tol), and PM2:DaTIC-4Cl (Tol)blend films. (b) out-of-plane line-cut profiles; solid lines and dotted lines indicate films deposited by CB-based solution and Tol-based solution, respectively.

To examine nanoscale network of two organic components, the surface morphologies of blended photoactive films processed by two solvents were investigated via atomic force microscopy (AFM). As displayed in **Figure 4-5,** DaTIC based films processed by both solutions, showed partially huge aggregates with low root-mean-square (RMS) roughness around 1.41-1.54 nm, due to lower miscibility of DaTIC NFA in both solvents. On the other hand, the AFM images

of PM2:DaTIC-4F films displayed smaller cluster than PM2:DaTIC films with showing 2.06 nm and 2.27 nm of RMS roughness for chlorobenzene and toluene-based coating cases, respectively. In addition, PM2:DaTIC-4Cl films showed homogeneous features, in particular, the films based on toluene process had no discernible segregation with bicontinuous phase. The finer morphology of PM2:DaTIC-4Cl film of toluene might lead to not only more sufficient exciton dissociation from the enlarged interfacial area but also charge transfer in the films, which is agree with the highest current density at short circuit condition (V=0) in this work.

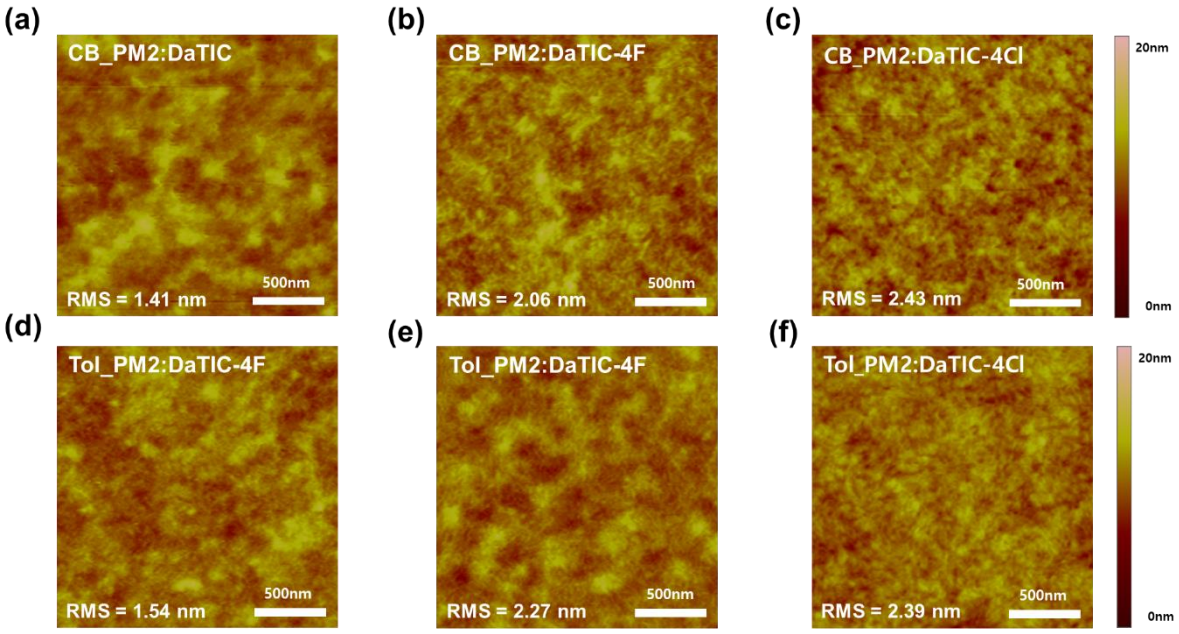

Figure 4-5. (a–d) AFM height images (2×2 μm) of the PM2:DaTIC-4F and PM2:DaTIC-4Cl blend films dissolved in chlorobenzene (CB) and toluene (Tol), respectively.

To further explain the difference in the device performance between a series of NFAs and processing solvents, the losses caused by non-geminate recombination in the organic photovoltaic devices are further investigated via light intensity dependence of *J*–*V* characteristics.[138–140] The short-circuit current J_{sc} vs light intensities dependence is almost linear (**Figure 4-6a,b**), suggesting a negligible effect of bimolecular recombination losses under short-circuit conditions for all systems.[141] The effect of low shunt resistance (R_{sh}) calculated from the dark current is also important for us to understand the nature of charge carrier recombination, and it has been

previously shown by Proctor *et al.* that the V_{OC} considering the effect of R_{sh} can be expressed as follows.[142]

$$V_{oc} = \frac{E_{gap}}{q} - \frac{kT}{q}\ln\left(\frac{(1-P)\gamma N_c^2}{PG - \frac{V_{oc}}{qLR_{sh}}}\right) \quad (4)$$

where E_{gap} is the bandgap, P is the dissociation probability of a bound electron-hole pair, N_c is the effective density of states, and G is the photogeneration rate. In the ideal case where R_{sh} is large enough, the slope of V_{OC} vs. ln$I$ won't be shifted significantly. However, low R_{sh} can increase the slope leading to a slope larger than kT/q even for a system with only bimolecular recombination.[142] Devices based on DaTIC show much smaller shunt resistance (R_{sh} ~ 0.005 MΩ cm^2) than that of devices based on DaTIC-4F and DaTIC-4Cl (R_{sh} > 0.2 MΩ cm^2), which induce large parasitic leakage current (J_{sh}) in the device ($J_{sh} = J_{ph} - J_{rec}$, where J_{ph} is the photogenerated current, J_{rec}

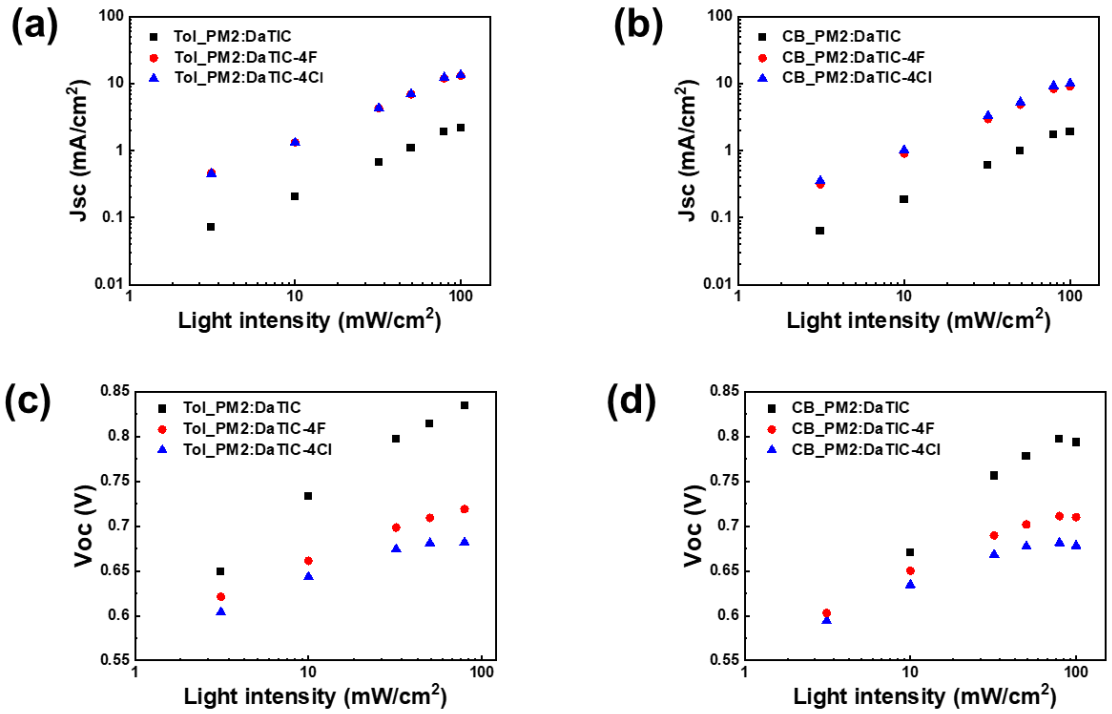

Figure 4-6. (a-b) Measured Jsc of PM2:DaTIC-based devices against light intensity on double-logarithmic scale. (c-d) measured Voc versus the natural logarithm of the light intensity.

is the recombination current). Such high leakage current caused by small shunt resistance can decrease the fill factor, thus further explaining the poor device performance of DaTIC based devices (PCEs < 1%).

Table 4-3. Average photovoltaic performances of OSCs based on PM2:DaTIC-X NFAs processed with CB and toluene under 100 mW·cm^{-2} AM 1.5 G illumination.

Donor	Solvent	Acceptor	J_{SC} (mA/cm^2)	V_{OC} (V)	FF	PCE (%)	s kT/q	R_{sh} MΩ cm2
PM2	CB	DaTIC	1.95	0.81	0.37	0.58	6.81	0.005
		DaTIC-4F	9.49	0.71	0.44	2.98	2.84	0.28
		DaTIC-4Cl	10.12	0.67	0.45	3.08	2.26	2.88
	Toluene	DaTIC	2.03	0.82	0.37	0.61	5.06	0.005
		DaTIC-4F	13.5	0.7	0.44	4.29	2.74	21.26
		DaTIC-4Cl	14.11	0.69	0.47	4.5	2.23	8.92

By analyzing the dependence of open-circuit voltage (V_{OC}) on the light intensity (I), the dominant non-geminate recombination mechanism in the devices can be qualitatively determined.[139,143,144] Generally, if the linear fitting of the V_{OC}–ln$I$ plot indicates a slope of $s = kT/q$ (k is the Boltzmann-constant, T is the absolute temperature, and q is the elementary charge), bimolecular recombination is the dominant loss mechanism in the photovoltaic devices.[139,140] Besides, the presence of trap states can be indicated by the deviations of the slope (bulk traps: $s > kT/q$; surface traps: $s < kT/q$). In all studied devices, the slopes of the V_{OC} vs. ln$I$ are much larger than kT/q (**Figure 4-6b**), which is a sign of the presence of trap-assisted Shockley-Read-Hall (SRH) recombination via deep traps in the bulk. Stronger SRH recombination in the CB cast devices is revealed by a higher value of slope compared to devices processing with toluene for all three systems (e.g., PM2:DaTIC, CB s = 6.81 kT/q, toluene s = 5.06 kT/q), which indicates a higher density of deep traps in the CB cast blends. Furthermore, heavier halogenated atoms (Cl > F) in

DaTIC-4Cl result in a smaller slope (s = 2.74 kT/q) than that of DaTIC-4Cl (s = 2.33 kT/q). The replacement of heavier halogenated atoms may improve the quality of the BHJ morphology by reducing the trap densities at the donor:acceptor interfaces, which further suppress the SRH recombination. It is also worth noting that DaTIC based devices show much larger slopes (s > 5 kT/q) than the other two NFAs with halogen substituents (s < 3 kT/q), which agrees with the small R_{sh} in the studied devices, and further explains the poor performance of this system caused by violent recombination via deep traps in the bulk. Since SRH processes is generally related with interfacial defects of photoactive blends in the devices and/or impurities in materials, we speculate that the tendency showed strong relationship with the morphological phase of blends films in this work.

4.2.3 Semitransparent optoelectronic device

For advanced and practical applications of the NIR optoelectronic devices, we further demonstrated semitransparent optoelectronic devices processed by toluene-based solution. these were fabricated with 15 nm thin Au electrode instead of thick Ag electrode to obtain high transparency in range of visible wavelength. The device architecture was shown in **Figure 4-7a**. In terms of OPVs (see **Figure 4-7b** and **Table 4-4**), the device resulted in 0.46 %, 3.40 % and 3.51 % PCE for PM2:DaTIC, PM2:DaTIC-4F and PM2:DaTIC-4Cl based photoactive film, respectively. The performance trend of improving device output by introducing halogen substituents on NFA, is consistent with the trend of devices with thick Ag electrode. The Voc and FF were quite similar with thick-electrode device, while current densities were decreased by around 30 %. The reduced photocurrent densities were resulted from the less reflected re-absorption of active layer in range of 450 nm – 600 nm relating with transmission of thin Au electrode. On the other hand, Responsivity and specific detectivity for these semitransparent

devices were estimated by following Equation (1) and Equation (2) under zero voltage condition. The dot lines in **Figure 4-7c** exhibit the EQE spectra and the dashed lines show responsivity. And the spectra of specific detectivity were shown in **Figure 4-7d**. As a result, optoelectronic devices based on PM2:DaTIC-4Cl approached 2.55×10^{13} Jones and 0.24 A/W as the best performance among this work. The maximum D* responses of PM2:DaTIC-4Cl blends showing over 10^{13} in over 800 nm wavelength is one of competitive performance among NIR OPDs reported until now. Furthermore, these devices showed high transparency in range of visible wavelength as shown in **Figure 4-7e**. The maximum transmittances of all semitransparent devices were observed at 500 nm and it showed AVT of 23.23 %, 26.51 % and 30.98 % calculated by Equation (3) for DaTIC, DaTIC-4F and DaTIC-4Cl devices, respectively. **Figure 4-7f** is a chart of reported detectivity values of various organic photodetectors, which were working at NIR region and under zero bias. Our work, the semitransparent PM2:DaTIC-4X devices processed by green solvent with narrow bandgap donor polymer, yielded a peak value of exceeding 10^{13} Jones at the wavelength of 825 nm as self-power mode, achieving the highest specific detectivity to date. These semitransparent NIR OPDs with using green solvent and outstanding performance might contribute to unobtrusive application such as self-healthcare devices by continuous detection of physiological signals in near future.

Table 4-4. Photovoltaic performances and photodetector characterization of PM2:DaTIC, PM2:DaTIC-4F and PM2:DATIC-4Cl devices

Donor	Acceptor	Solvent	J_{SC} (mA/cm^2)	V_{OC} (V)	FF	PCE (%)	Responsivity @λ_{max}	Specific Detectivity* (Jones@0 V)	AVT (%)
PM2	DaTIC	Tol	1.48	0.82	0.38	0.46	0.04@790	9.80×10^{11}	23.23
	DaTIC-4F		10.43	0.69	0.47	3.40	0.23@802	1.80×10^{13}	26.51
	DaTIC-4Cl		11.07	0.66	0.48	3.51	0.24@815	2.55×10^{13}	30.98

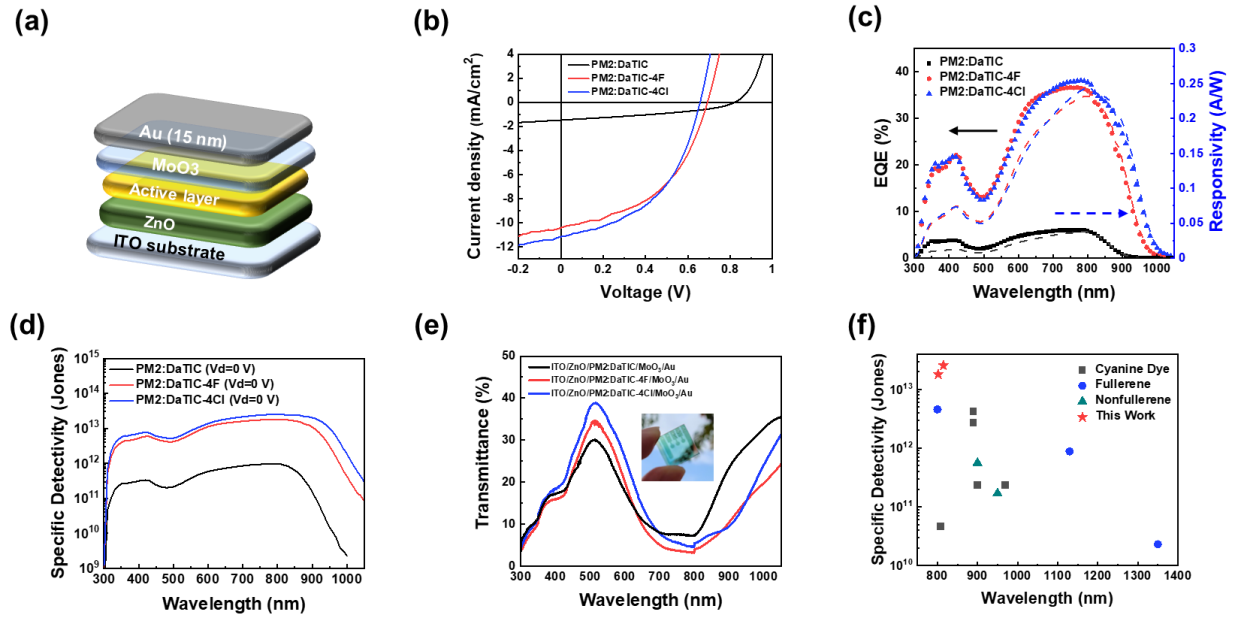

Figure 4-7. (a) device structure of semitransparent photodiode, (b) *J-V* curve (The inset shows the dark J-V curve), (c) EQE and responsivity spectra, (d) specific detectivity spectra calculated with zero voltage, (e) transmittance of entire devices and (f) reported D* of organic OPDs at 0V.

4.3 Conclusions

In summary, we have successfully designed and synthesized new UNBG-NFAs based on A−D'–D−D'–A molecular structure, featuring efficient NIR photovoltaic properties with green solvent processibility. The ICT effect is modulated via simple but efficient method of end-dye substituent modification of UNBG-NFAs enabling tailored of materials' optical bandgaps and energetics to achieve better compromise between AVT and device performance.

With the new NIR NFAs, the organic optoelectronic devices for both of solar cells and photodetectors have been implemented with using a PM2 donor polymer of narrow optical bandgap and green solvent-based fabrication. As a result, PM2:DaTIC-4Cl devices processed by toluene based solution approached photovoltaic performance of 4.50 % PCE as an organic solar cells and 2.75×10^{13} Jones at 825 nm at zero voltage as a NIR photodetector. Which were from higher photocurrent generation from broaden light absorbance and bicontinuous film morphology

leading to sufficient chart transport in the devices. Furthermore, by applying transparent thin Au top electrode to the active blends, we demonstrated and characterized semitransparent organic optoelectronic devices. The PM2:DaTIC-4Cl device showed photovoltaic performance of 3.51 % PCE and higher detectivity of 2.55×10^{13} Jones with the transparency of 31 % in visible wavelength region. In the near future, we anticipate that transparent NIR-OPDs fabricated through a narrow bandgap composition and a green solvent-based solution process could emerge as a highly promising device.

4.4 Experimental and supplementary information

Materials All reagents and chemicals were purchased from commercial sources and used without further purification. All anhydrous organic solvents for the synthesis, characterization, and device fabrication steps were purchased from Sigma-Aldrich and TCI. Compounds **1**, **6** was purchased from 1 Materials Inc. Compound **2**,**3** and **4** was synthesized *via* conditions from literature.[108,145]

Calculation methods The optimized structures, energy levels, and HOMO and LUMO orbital distributions were calculated the density functional (DFT) level of theory, using the semi-empirically tuned ωb97xd/6-31G(d,p) functional and basis set. The simulated absorption peak wavelength pf designed molecules were calculated via time-dependent DFT simulation method. To simplify calculations, the alkyl chains were replaced with methyl or ethyl chains. The HOMO and LUMO levels were calculated by determining the difference in energy from the optimized ground state geometry of the cation and anion, respectively.[90]

Device Fabrication*:* optoelectronic devices were fabricated with an inverted structure of ITO/ZnO (25 nm)/polymer:acceptor BHJ/MoO_3(5 nm) / Ag(90 nm). Patterned ITO glass substrates were cleaned by ultrasonic treatment in detergent, distilled water, acetone and isopropyl alcohol, then

dried in an oven for overnight at 100 °C and treated with UV-ozone for 20 min to remove residues. Zinc oxide (ZnO) was deposited by spincoating a solution of diethylzinc (5 wt%) dissolved in a 1:5 mixture of toluene : tetrahydrofuran (THF) at 3000 rpm for 30 s onto cleaned ITO substrates then dried for 10 min at 110 °C in air. Subsequently, mixed solutions of PM2:NFAs (25 mg/ml) in either chlorobenzene (CB) or toluene (Tol) solvents were spin-casted on top of the ZnO film in a nitrogen (N_2) filled glove box. 5 nm MoO_3 (~0.2 Å/s) layer and 90 nm Ag (~2.0 Å/s) electrode were thermally evaporated at < 1.0×10^{-6} torr using a shadow mask (active area 3.25 mm^2). To fabricate semitransparent device, thin Au electrode (15 nm)were deposited by thermal evaporation with ~1.0 Å/s rate. The current density-voltage (*J-V* curve) characteristics of devices were measured using a Keithley 2635A source Measure unit under AM 1.5G irradiation at 100 mW/cm^2 and/or dark environment. EQE measurements were conducted in ambient air using an EQE system (Model QEX7) by PV measurements Inc.

Characterizations of compounds ^1H and ^{13}C NMR spectra of intermediate monomers were recorded on a **Varian Unity Inova 500 MHz spectrometer** in deuterated chloroform solution ($CDCl_3$) with 0.003%TMS as internal reference. Ultraviolet-Visible-Near-infrared (UV-Vis-NIR) absorption spectra were recorded on a Perkin Elmer Lambda 750 spectrophotometer. For the measurements of thin films, materials were spun coated onto precleaned glass substrates from chloroform solutions (10 mg mL^{-1}). Optical band gap was determined from the absorption onset of thin film sample.

Electrochemical characterization The electrochemical cyclic voltammetry (CV) was conducted on a CHI-730B electrochemistry workstation with glassy carbon disk, Pt wire, and Ag/Ag+ electrode as the working electrode, counter electrode, and reference electrode, respectively in a 0.1

M tetrabutylammonium hexafluorophosphate (n-Bu_4NPF_6) anhydrous acetonitrile solution at a potential scan rate of 40 mV s^{-1}. Thin films of samples were deposited onto the glassy carbon working electrode from a 3 mg mL^{-1} chloroform solution. The electrochemical onsets were determined at the position where the current starts to differ from the baseline. The potential of Ag/AgCl reference electrode was internally calibrated by using the ferrocene/ferrocenium redox couple (Fc/Fc^+).

Film microstructure characterization Transmission electron microscopy (TEM) images were obtained using JEOL JEM-2200FS (with Image Cs-corrector).

Grazing incidence wide angle X-ray scattering (GIWAXS) analysis 2D GIWAXS measurements were performed using Beamline 9A at the Pohang Accelerator Laboratory (PAL). The photon energy is 11.055 keV (λ = 1.1214 Å). The angle between the film surface and the incident beam was fixed at 0.12° for all of the samples. The measurements were obtained at scanning intervals of 2θ between 3° and 25°. The 2D GIWAXS images from the films were analyzed according to the relationship between the scattering vector q and the d spacing, $q = 2\pi/d$. The GIWAXS images shown are normalized with respect to exposure time.

Material Synthesis

Compound **5**: A mixture of compound **3** (300mg, 0.4 mmol), compound **4** (318mg, 1.0 mmol), $Pd(PPh_3)_4$ (24 mg) and anhydrous toluene (30 mL) was added into a flame-dried and nitrogen-filled microwave tube in glovebox. The reactant was heated to 110 °C for 24 h. After the mixture cooled to room temperature, DI water was added, and the mixture was extracted with dichloromethane (50 ml x 3). The organic layer was dried over Na_2SO_4 and concentrated in

vacuum. The crude product was purified by silica gel column chromatography (*n*-hexane:DCM, 1:1) to afford **5** as sticky deep red solid (200 mg, 56%).

^{1}H NMR for compound **5** (500MHz, $CDCl_3$, ppm): δ 9.83 (s, 2H), 7.54 (s, 2H), 6.88 (t, 2H), 6.82 (s, 2H), 2.71-2.78 (m, 4H), 1.79-1.90 (br, 24H), 1.03-1.43 (br, 32H), 0.69–0.95 (m, 24H).

Compound **DaTIC-4X**: A mixture of bisaldehyde intermediate **5**, different halogenated IC-4X compound **4**, dry chloroform (20 mL), and pyridine was added into to a flame-dried and nitrogen-filled one-neck round-bottom flask The flask was purged with N_2 for 20 min and the reactant was heated to 60 °C for 12 h. After the mixture cooled to room temperature, the reaction mixture was concentrated in vacuum. The residue was purified by silica gel column chromatography to afford **DaTIC-4x** as dark blue solid.

^{1}H NMR for compound **DaTIC-4F**: (500MHz, $CDCl_3$, ppm): δ 8.76 (d, 2H), 8.53 (m, 2H), 7.66 (m, 2H), δ 7.18 (t, 2H), δ 7.07 (s, 2H), 2.82 (m, 4H), 1.63-1.99 (br, 24H), 1.17-1.43 (br, 32H), 0.76–0.96 (m, 24H). MS (MALDI-TOF): calculated m/z 1286.49; found m/z 1353.587.

^{1}H NMR for compound **DaTIC-4Cl**: (500MHz, $CDCl_3$, ppm):): δ 8.77 (d, 2H), 7.95 (m, 2H), 7.63 (m, 2H), δ 7.18 (d, 2H), δ 7.07 (s, 2H), 2.81 (m, 4H), 1.52-1.98 (br, 24H), 1.07-1.44 (br, 32H), 0.75–0.95 (m, 24H). MS (MALDI-TOF): calculated m/z 1353.37; found m/z 1287.687.

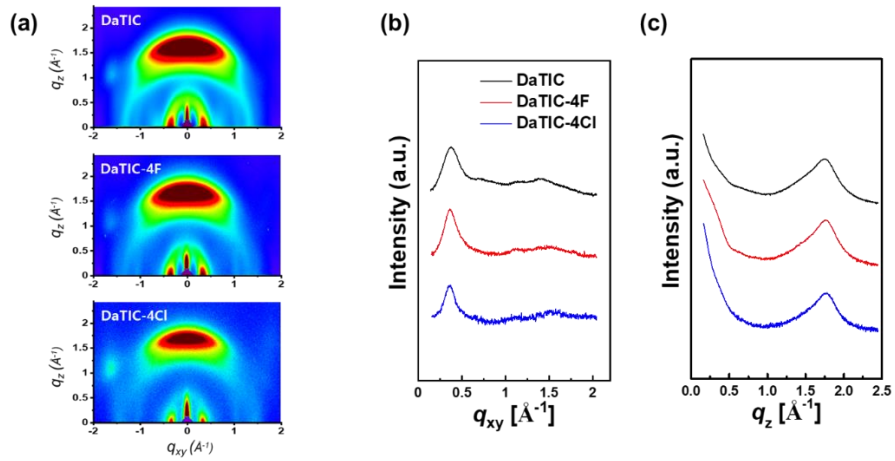

Figure 4-S1. 2D GIWAXS images of (a) neat DaTIC-4F and neat DaTIC-4Cl films deposited by CB-based solution, (b)In-plane and (c) out-of-plane line-cut profiles.

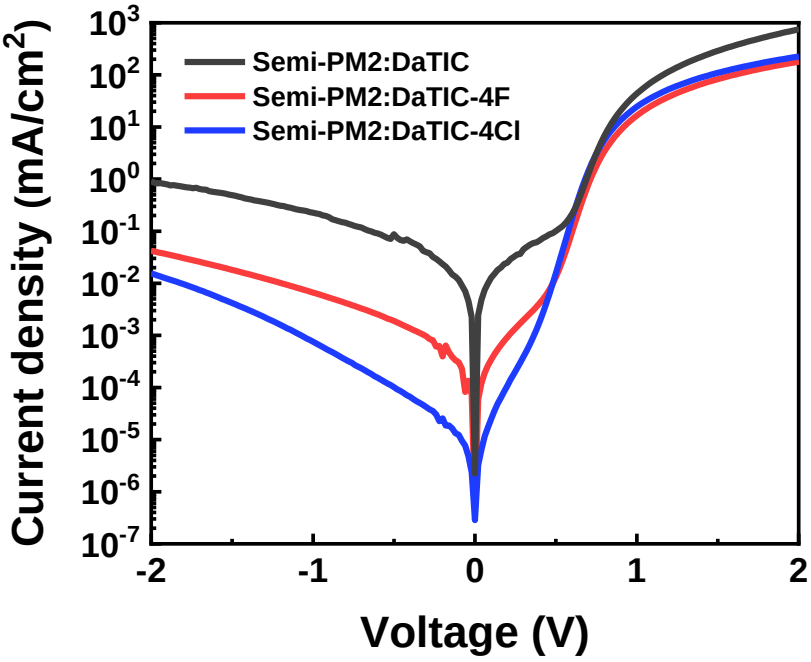

Figure 4-S2. Dark *J-V* curve of the semitransparent devices fabricated by toluene-solution.

Table 4-S1. Crystallographic parameters calculated from GIWAXS profiles of neat NFAs materials films and PM2:DaTICs blend films.

Materials	**Packing Parameters**				
	Axis	π-π stack [Å^{-1}]	d-spacing [Å]	Lamella stack [Å^{-1}]	d-spacing [Å]
DaTIC	q_{xy}	-	-	0.38	16.5
	$q_{vertical}$	1.75	3.59	-	-
DaTIC-4F	q_{xy}	-	-	0.36	17.5
	$q_{vertical}$	1.77	3.55	-	-
DaTIC-4Cl	q_{xy}	-	-	0.36	17.5
	$q_{vertical}$	1.78	3.53	-	-
PM2 : DaTIC, CB	q_{xy}	-	-	0.27	23.3
	$q_{vertical}$	1.70	3.70	-	-
PM2 : DaTIC-4F, CB	q_{xy}	-	-	0.28	22.4
	$q_{vertical}$	1.72	3.65	-	-
PM2 : DaTIC-4Cl, CB	q_{xy}	-	-	0.28	22.4
	$q_{vertical}$	1.74	3.61	-	-
PM2 : DaTIC, Tol	q_{xy}	-	-	0.28	22.4
	$q_{vertical}$	1.72	3.65	-	-
PM2 : DaTIC-4F, Tol	q_{xy}	-	-	0.28	22.4
	$q_{vertical}$	1.73	3.63	-	-
PM2 : DaTIC-4Cl, Tol	q_{xy}	-	-	0.28	22.4
	$q_{vertical}$	1.75	3.59	-	-

Summary and outlook

This dissertation highlights the challenges and opportunities presented by organic semiconductors, including their potential to enable low-cost and eco-friendly large-scale commercial production. Specifically, the dissertation outlines two major directions for advancing the development of n-type semiconducting materials, particularly non-fullerene materials. The first chapter serves as a demonstration of how molecular engineering on different electron-sufficient and electron-deficient composite motifs within NFAs' molecular framework affect materials' solid-state properties and corresponding device physics and performance. By employing this material design strategy shown in chapter 1, DFT calculations have been utilized to facilitate efficient screening of molecular designs during the conceptual stage, with the goal of reducing the need for extensive synthetic efforts. After obtaining simulated optical properties of conceptual molecular structures and considering of the materials' synthetic complexity, two ultra-narrow bandgap NFAs have been synthesized, characterized and applied in NIR-OPD applications. Inspired by the previously demonstrated molecular design strategy, a series of NFAs utilizing A-π-D-π-A structures have been synthesized and with the purpose of designing molecules with tailored solubility in the green solvent of 2-MeTHF. The following studies on how materials' solid state characteristics were effected via molecular structural variation and processing solvents have been carried out thus leading to a better understanding of structure-properties relationship which in return provides guidance for material design for green solvent processable organic semiconductors. The last chapter demonstrates an example of the application of non-halogenated solvent processable NFAs in semi-transparent NIR-OPD devices. However, the system could not be repeated in more "greener" solvent, such as 2-MeTHF and alcoholic solvents, because of the limitation of macromolecule of donor polymer. To advance towards a truly green solvent-

processed and highly efficient OPV system, further materials development will be necessary, particularly for small molecular donors and organic semiconductors that are processable using alcoholic/polar solvents.[146–148]

Bibliography

(1) Xu, H.; Liu, J.; Zhang, J.; Zhou, G.; Luo, N.; Zhao, N. Flexible Organic/Inorganic Hybrid Near-Infrared Photoplethysmogram Sensor for Cardiovascular Monitoring. *Adv. Mater.* **2017**, *29* (31), 1700975. https://doi.org/10.1002/adma.201700975.

(2) Köhler, A.; Bässler, H. *Electronic Processes in Organic Semiconductors: An Introduction*; John Wiley & Sons, 2015.

(3) Wang, Q.; Xie, Y.; Soltani-Kordshuli, F.; Eslamian, M. Progress in Emerging Solution-Processed Thin Film Solar Cells – Part I: Polymer Solar Cells. *Renew. Sustain. Energy Rev.* **2016**, *56*, 347–361. https://doi.org/10.1016/j.rser.2015.11.063.

(4) Orrill, M.; LeBlanc, S. Printed Thermoelectric Materials and Devices: Fabrication Techniques, Advantages, and Challenges. *J. Appl. Polym. Sci.* **2017**, *134* (3). https://doi.org/10.1002/app.44256.

(5) Søndergaard, R. R.; Hösel, M.; Krebs, F. C. Roll-to-Roll Fabrication of Large Area Functional Organic Materials. *J. Polym. Sci. Part B Polym. Phys.* **2013**, *51* (1), 16–34. https://doi.org/10.1002/polb.23192.

(6) Gather, M. C.; Köhnen, A.; Meerholz, K. White Organic Light-Emitting Diodes. *Adv. Mater.* **2011**, *23* (2), 233–248. https://doi.org/10.1002/adma.201002636.

(7) Zou, S.-J.; Shen, Y.; Xie, F.-M.; Chen, J.-D.; Li, Y.-Q.; Tang, J.-X. Recent Advances in Organic Light-Emitting Diodes: Toward Smart Lighting and Displays. *Mater. Chem. Front.* **2020**, *4* (3), 788–820. https://doi.org/10.1039/C9QM00716D.

(8) Kwon, S.; Hwang, Y. H.; Nam, M.; Chae, H.; Lee, H. S.; Jeon, Y.; Lee, S.; Kim, C. Y.; Choi, S.; Jeong, E. G.; Choi, K. C. Recent Progress of Fiber Shaped Lighting Devices for Smart Display Applications—A Fibertronic Perspective. *Adv. Mater.* **2020**, *32* (5), 1903488. https://doi.org/10.1002/adma.201903488.

(9) Seri, M.; Mercuri, F.; Ruani, G.; Feng, Y.; Li, M.; Xu, Z.-X.; Muccini, M. Toward Real Setting Applications of Organic and Perovskite Solar Cells: A Comparative Review. *Energy Technol.* **2021**, *9* (5), 2000901. https://doi.org/10.1002/ente.202000901.

(10) Chen, F.-C. Emerging Organic and Organic/Inorganic Hybrid Photovoltaic Devices for Specialty Applications: Low-Level-Lighting Energy Conversion and Biomedical Treatment. *Adv. Opt. Mater.* **2019**, *7* (1), 1800662. https://doi.org/10.1002/adom.201800662.

(11) Kim, S.; Jahandar, M.; Jeong, J. H.; Lim, D. C. Recent Progress in Solar Cell Technology for Low-Light Indoor Applications. *Curr. Altern. Energy* **2019**, *3* (1), 3–17. https://doi.org/10.2174/1570180816666190112141857.

(12) *Transparent organic photovoltaics: A strategic niche to advance commercialization | Elsevier Enhanced Reader*. https://doi.org/10.1016/j.joule.2021.07.004.

(13) Liao, C.; Zhang, M.; Yao, M. Y.; Hua, T.; Li, L.; Yan, F. Flexible Organic Electronics in Biology: Materials and Devices. *Adv. Mater.* **2015**, *27* (46), 7493–7527. https://doi.org/10.1002/adma.201402625.

(14) Liu, K.; Ouyang, B.; Guo, X.; Guo, Y.; Liu, Y. Advances in Flexible Organic Field-Effect Transistors and Their Applications for Flexible Electronics. *Npj Flex. Electron.* **2022**, *6* (1), 1–19. https://doi.org/10.1038/s41528-022-00133-3.

(15) Forrest, S. R. The Path to Ubiquitous and Low-Cost Organic Electronic Appliances on Plastic. *Nature* **2004**, *428* (6986), 911–918. https://doi.org/10.1038/nature02498.

(16) Russ, B.; Glaudell, A.; Urban, J. J.; Chabinyc, M. L.; Segalman, R. A. Organic Thermoelectric Materials for Energy Harvesting and Temperature Control. *Nat. Rev. Mater.* **2016**, *1* (10), 1–14. https://doi.org/10.1038/natrevmats.2016.50.

(17) Yang, D.; Ma, D. Development of Organic Semiconductor Photodetectors: From Mechanism to Applications. *Adv. Opt. Mater.* **2019**, *7* (1), 1800522. https://doi.org/10.1002/adom.201800522.

(18) García de Arquer, F. P.; Armin, A.; Meredith, P.; Sargent, E. H. Solution-Processed Semiconductors for next-Generation Photodetectors. *Nat. Rev. Mater.* **2017**, *2* (3), 1–17. https://doi.org/10.1038/natrevmats.2016.100.

(19) Ling, M. M.; Bao, Z. Thin Film Deposition, Patterning, and Printing in Organic Thin Film Transistors. *Chem. Mater.* **2004**, *16* (23), 4824–4840. https://doi.org/10.1021/cm0496117.

(20) Gwinner, M. C.; Pietro, R. D.; Vaynzof, Y.; Greenberg, K. J.; Ho, P. K. H.; Friend, R. H.; Sirringhaus, H. Doping of Organic Semiconductors Using Molybdenum Trioxide: A Quantitative Time-Dependent Electrical and Spectroscopic Study. *Adv. Funct. Mater.* **2011**, *21* (8), 1432–1441. https://doi.org/10.1002/adfm.201002696.

(21) Sirringhaus, H. Reliability of Organic Field-Effect Transistors. *Adv. Mater.* **2009**, *21* (38–39), 3859–3873. https://doi.org/10.1002/adma.200901136.

(22) Jia, H.; Lei, T. Emerging Research Directions for N-Type Conjugated Polymers. *J. Mater. Chem. C* **2019**, *7* (41), 12809–12821. https://doi.org/10.1039/C9TC02632K.

(23) Lv, G.; Wang, H.; Tong, Y.; Dong, L.; Zhao, X.; Zhao, P.; Tang, Q.; Liu, Y. Flexible, Conformable Organic Semiconductor Proximity Sensor Array for Electronic Skin. *Adv. Mater. Interfaces* **2020**, *7* (16), 2000306. https://doi.org/10.1002/admi.202000306.

(24) Zhu, Y.; Zhu, Y.; Mao, H.; He, Y.; Jiang, S.; Zhu, L.; Chen, C.; Wan, C.; Wan, Q. Recent Advances in Emerging Neuromorphic Computing and Perception Devices. *J. Phys. Appl. Phys.* **2022**, *55* (5), 053002. https://doi.org/10.1088/1361-6463/ac2868.

(25) Oh, J. Y.; Rondeau-Gagné, S.; Chiu, Y.-C.; Chortos, A.; Lissel, F.; Wang, G.-J. N.; Schroeder, B. C.; Kurosawa, T.; Lopez, J.; Katsumata, T.; Xu, J.; Zhu, C.; Gu, X.; Bae, W.-G.; Kim, Y.; Jin, L.; Chung, J. W.; Tok, J. B.-H.; Bao, Z. Intrinsically Stretchable and Healable Semiconducting Polymer for Organic Transistors. *Nature* **2016**, *539* (7629), 411–415. https://doi.org/10.1038/nature20102.

(26) Nielsen, C. B.; Holliday, S.; Chen, H.-Y.; Cryer, S. J.; McCulloch, I. Non-Fullerene Electron Acceptors for Use in Organic Solar Cells. *Acc. Chem. Res.* **2015**, *48* (11), 2803–2812. https://doi.org/10.1021/acs.accounts.5b00199.

(27) Wadsworth, A.; Moser, M.; Marks, A.; Little, M. S.; Gasparini, N.; Brabec, C. J.; Baran, D.; McCulloch, I. Critical Review of the Molecular Design Progress in Non-Fullerene Electron Acceptors towards Commercially Viable Organic Solar Cells. *Chem. Soc. Rev.* **2019**, *48* (6), 1596–1625. https://doi.org/10.1039/C7CS00892A.

(28) Gurney, R. S.; Lidzey, D. G.; Wang, T. A Review of Non-Fullerene Polymer Solar Cells: From Device Physics to Morphology Control. *Rep. Prog. Phys.* **2019**, *82* (3), 036601. https://doi.org/10.1088/1361-6633/ab0530.

(29) Simões, J.; Dong, T.; Yang, Z. Non-Fullerene Acceptor Organic Photodetector for Skin-Conformable Photoplethysmography Applications. *Adv. Mater. Interfaces* **2022**, *9* (10), 2101897. https://doi.org/10.1002/admi.202101897.

(30) Sonar, P.; Lim, J. P. F.; Leok Chan, K. Organic Non-Fullerene Acceptors for Organic Photovoltaics. *Energy Environ. Sci.* **2011**, *4* (5), 1558–1574. https://doi.org/10.1039/C0EE00668H.

(31) *A High-Performance Solution-Processed Organic Photodetector for Near-Infrared Sensing - Huang - 2020 - Advanced Materials - Wiley Online Library*. https://onlinelibrary.wiley.com/doi/full/10.1002/adma.201906027 (accessed 2022-04-11).

(32) Diao, Y.; Shaw, L.; Bao, Z.; B. Mannsfeld, S. C. Morphology Control Strategies for Solution-Processed Organic Semiconductor Thin Films. *Energy Environ. Sci.* **2014**, *7* (7), 2145–2159. https://doi.org/10.1039/C4EE00688G.

(33) Moser, M.; Wadsworth, A.; Gasparini, N.; McCulloch, I. Challenges to the Success of Commercial Organic Photovoltaic Products. *Adv. Energy Mater.* **2021**, *11* (18), 2100056. https://doi.org/10.1002/aenm.202100056.

(34) Bronstein, H.; Nielsen, C. B.; Schroeder, B. C.; McCulloch, I. The Role of Chemical Design in the Performance of Organic Semiconductors. *Nat. Rev. Chem.* **2020**, *4* (2), 66–77. https://doi.org/10.1038/s41570-019-0152-9.

(35) Cheng, P.; Li, G.; Zhan, X.; Yang, Y. Next-Generation Organic Photovoltaics Based on Non-Fullerene Acceptors. *Nat. Photonics* **2018**, *12* (3), 131–142. https://doi.org/10.1038/s41566-018-0104-9.

(36) Xue, Q.; Xia, R.; Brabec, C. J.; Yip, H.-L. Recent Advances in Semi-Transparent Polymer and Perovskite Solar Cells for Power Generating Window Applications. *Energy Environ. Sci.* **2018**, *11* (7), 1688–1709. https://doi.org/10.1039/C8EE00154E.

(37) Traverse, C. J.; Pandey, R.; Barr, M. C.; Lunt, R. R. Emergence of Highly Transparent Photovoltaics for Distributed Applications. *Nat. Energy* **2017**, *2* (11), 849. https://doi.org/10.1038/s41560-017-0016-9.

(38) Brus, V. V.; Lee, J.; Luginbuhl, B.; Ko, S.-J.; Bazan, G. C.; Nguyen, T.-Q. Solution-Processed Semitransparent Organic Photovoltaics: From Molecular Design to Device Performance. *Adv. Mater. 0* (0), 1900904. https://doi.org/10.1002/adma.201900904.

(39) Green, M. A. Commercial Progress and Challenges for Photovoltaics. *Nat. Energy* **2016**, *1* (1), 15015. https://doi.org/10.1038/nenergy.2015.15.

(40) Arias, A. C.; MacKenzie, J. D.; McCulloch, I.; Rivnay, J.; Salleo, A. Materials and Applications for Large Area Electronics: Solution-Based Approaches. *Chem. Rev.* **2010**, *110* (1), 3–24. https://doi.org/10.1021/cr900150b.

(41) Dong, H.; Zhu, H.; Meng, Q.; Gong, X.; Hu, W. Organic Photoresponse Materials and Devices. *Chem Soc Rev* **2012**, *41* (5), 1754–1808. https://doi.org/10.1039/C1CS15205J.

(42) Ying, L.; Huang, F.; Bazan, G. C. Regioregular Narrow-Bandgap-Conjugated Polymers for Plastic Electronics. *Nat. Commun.* **2017**, *8*, 14047. https://doi.org/10.1038/ncomms14047.

(43) Cui, Q.; Bazan, G. C. Narrow Band Gap Conjugated Polyelectrolytes. *Acc. Chem. Res.* **2018**, *51* (1), 202–211. https://doi.org/10.1021/acs.accounts.7b00501.

(44) Emmott, C. J. M.; Röhr, J. A.; Campoy-Quiles, M.; Kirchartz, T.; Urbina, A.; Ekins-Daukes, N. J.; Nelson, J. Organic Photovoltaic Greenhouses: A Unique Application for Semi-Transparent PV? *Energy Environ. Sci.* **2015**, *8* (4), 1317–1328. https://doi.org/10.1039/C4EE03132F.

(45) Wu, Z.; Zhai, Y.; Kim, H.; Azoulay, J. D.; Ng, T. N. Emerging Design and Characterization Guidelines for Polymer-Based Infrared Photodetectors. *Acc. Chem. Res.* **2018**, *51* (12), 3144–3153. https://doi.org/10.1021/acs.accounts.8b00446.

(46) Liu, X.; Lin, Y.; Liao, Y.; Wu, J.; Zheng, Y. Recent Advances in Organic Near-Infrared Photodiodes. *J. Mater. Chem. C* **2018**, *6* (14), 3499–3513. https://doi.org/10.1039/C7TC05042A.

(47) Yu, G.; Gao, J.; Hummelen, J. C.; Wudl, F.; Heeger, A. J. Polymer Photovoltaic Cells: Enhanced Efficiencies via a Network of Internal Donor-Acceptor Heterojunctions. *Science* **1995**, *270* (5243), 1789–1791. https://doi.org/10.1126/science.270.5243.1789.

(48) Huang, Y.; Kramer, E. J.; Heeger, A. J.; Bazan, G. C. *Bulk Heterojunction Solar Cells: Morphology and Performance Relationships*. ACS Publications. https://doi.org/10.1021/cr400353v.

(49) Lee, H.; Park, C.; Sin, D. H.; Park, J. H.; Cho, K. Recent Advances in Morphology Optimization for Organic Photovoltaics. *Adv. Mater.* **2018**, *30* (34), 1800453. https://doi.org/10.1002/adma.201800453.

(50) Lee, J.; Ko, S.-J.; Lee, H.; Huang, J.; Zhu, Z.; Seifrid, M.; Vollbrecht, J.; Brus, V. V.; Karki, A.; Wang, H.; Cho, K.; Nguyen, T.-Q.; Bazan, G. C. Side-Chain Engineering of Nonfullerene Acceptors for Near-Infrared Organic Photodetectors and Photovoltaics. *ACS Energy Lett.* **2019**, *4* (6), 1401–1409. https://doi.org/10.1021/acsenergylett.9b00721.

(51) Lee, J.; Ko, S.-J.; Seifrid, M.; Lee, H.; McDowell, C.; Luginbuhl, B. R.; Karki, A.; Cho, K.; Nguyen, T.-Q.; Bazan, G. C. Design of Nonfullerene Acceptors with Near-Infrared Light Absorption Capabilities. *Adv. Energy Mater.* **2018**, *8* (26), 1801209. https://doi.org/10.1002/aenm.201801209.

(52) Yao, H.; Cui, Y.; Yu, R.; Gao, B.; Zhang, H.; Hou, J. Design, Synthesis, and Photovoltaic Characterization of a Small Molecular Acceptor with an Ultra-Narrow Band Gap. *Angew. Chem. Int. Ed.* **2017**, *56* (11), 3045–3049. https://doi.org/10.1002/anie.201610944.

(53) Zhang, G.; Zhao, J.; Chow, P. C. Y.; Jiang, K.; Zhang, J.; Zhu, Z.; Zhang, J.; Huang, F.; Yan, H. Nonfullerene Acceptor Molecules for Bulk Heterojunction Organic Solar Cells. *Chem. Rev.* **2018**, *118* (7), 3447–3507. https://doi.org/10.1021/acs.chemrev.7b00535.

(54) Hou, J.; Inganäs, O.; Friend, R. H.; Gao, F. Organic Solar Cells Based on Non-Fullerene Acceptors. *Nat. Mater.* **2018**, *17* (2), 119–128. https://doi.org/10.1038/nmat5063.

(55) Vuuren, R. D. J.; Armin, A.; Pandey, A. K.; Burn, P. L.; Meredith, P. Organic Photodiodes: The Future of Full Color Detection and Image Sensing. *Adv. Mater.* **2016**, *28* (24), 4766–4802. https://doi.org/10.1002/adma.201505405.

(56) Baeg, K.-J.; Binda, M.; Natali, D.; Caironi, M.; Noh, Y.-Y. Organic Light Detectors: Photodiodes and Phototransistors. *Adv. Mater.* **2013**, *25* (31), 4267–4295. https://doi.org/10.1002/adma.201204979.

(57) Lee, J.; Ko, S.-J.; Seifrid, M.; Lee, H.; Luginbuhl, B. R.; Karki, A.; Ford, M.; Rosenthal, K.; Cho, K.; Nguyen, T.-Q.; Bazan, G. C. Bandgap Narrowing in Non-Fullerene Acceptors: Single Atom Substitution Leads to High Optoelectronic Response Beyond 1000 Nm. *Adv. Energy Mater.* **2018**, *8* (24), 1801212. https://doi.org/10.1002/aenm.201801212.

(58) Cheng, Y.-J.; Yang, S.-H.; Hsu, C.-S. Synthesis of Conjugated Polymers for Organic Solar Cell Applications. *Chem. Rev.* **2009**, *109* (11), 5868–5923. https://doi.org/10.1021/cr900182s.

(59) Dou, L.; Liu, Y.; Hong, Z.; Li, G.; Yang, Y. Low-Bandgap Near-IR Conjugated Polymers/Molecules for Organic Electronics. *Chem. Rev.* **2015**, *115* (23), 12633–12665. https://doi.org/10.1021/acs.chemrev.5b00165.

(60) Li, W.; Hendriks, K. H.; Wienk, M. M.; Janssen, R. A. J. Diketopyrrolopyrrole Polymers for Organic Solar Cells. *Acc. Chem. Res.* **2016**, *49* (1), 78–85. https://doi.org/10.1021/acs.accounts.5b00334.

(61) Huo, L.; Zhou, Y.; Li, Y. Alkylthio-Substituted Polythiophene: Absorption and Photovoltaic Properties. *Macromol. Rapid Commun.* **2009**, *30* (11), 925–931. https://doi.org/10.1002/marc.200800785.

(62) Yao, H.; Chen, Y.; Qin, Y.; Yu, R.; Cui, Y.; Yang, B.; Li, S.; Zhang, K.; Hou, J. Design and Synthesis of a Low Bandgap Small Molecule Acceptor for Efficient Polymer Solar Cells. *Adv. Mater.* **2016**, *28* (37), 8283–8287. https://doi.org/10.1002/adma.201602642.

(63) Lee, J.; Kim, M.; Kang, B.; Jo, S. B.; Kim, H. G.; Shin, J.; Cho, K. Side-Chain Engineering for Fine-Tuning of Energy Levels and Nanoscale Morphology in Polymer Solar Cells. *Adv. Energy Mater.* **2014**, *4* (10), 1400087. https://doi.org/10.1002/aenm.201400087.

(64) Chen, S.; Yao, H.; Hu, B.; Zhang, G.; Arunagiri, L.; Ma, L.-K.; Huang, J.; Zhang, J.; Zhu, Z.; Bai, F.; Ma, W.; Yan, H. A Nonfullerene Semitransparent Tandem Organic Solar Cell with 10.5% Power Conversion Efficiency. *Adv. Energy Mater.* **2018**, *8* (31), 1800529. https://doi.org/10.1002/aenm.201800529.

(65) Li, S.; Ye, L.; Zhao, W.; Zhang, S.; Mukherjee, S.; Ade, H.; Hou, J. Energy-Level Modulation of Small-Molecule Electron Acceptors to Achieve over 12% Efficiency in Polymer Solar Cells. *Adv. Mater.* **2016**, *28* (42), 9423–9429. https://doi.org/10.1002/adma.201602776.

(66) Zhao, Q.; Qu, J.; He, F. Chlorination: An Effective Strategy for High-Performance Organic Solar Cells. *Adv. Sci.* **2020**, *7* (14), 2000509. https://doi.org/10.1002/advs.202000509.

(67) Xu, X.; Zhou, X.; Zhou, K.; Xia, Y.; Ma, W.; Inganäs, O. Large-Area, Semitransparent, and Flexible All-Polymer Photodetectors. *Adv. Funct. Mater.* **2018**, *28* (48), 1805570. https://doi.org/10.1002/adfm.201805570.

(68) Song, X.; Gasparini, N.; Nahid, M. M.; Chen, H.; Macphee, S. M.; Zhang, W.; Norman, V.; Zhu, C.; Bryant, D.; Ade, H.; McCulloch, I.; Baran, D. A Highly Crystalline Fused-Ring n-Type Small Molecule for Non-Fullerene Acceptor Based Organic Solar Cells and Field-Effect Transistors. *Adv. Funct. Mater.* **2018**, *28* (35), 1802895. https://doi.org/10.1002/adfm.201802895.

(69) Shi, X.; Zuo, L.; Jo, S. B.; Gao, K.; Lin, F.; Liu, F.; Jen, A. K.-Y. Design of a Highly Crystalline Low-Band Gap Fused-Ring Electron Acceptor for High-Efficiency Solar Cells with Low Energy Loss. *Chem. Mater.* **2017**, *29* (19), 8369–8376. https://doi.org/10.1021/acs.chemmater.7b02853.

(70) Chen, S.; Liu, Y.; Zhang, L.; Chow, P. C. Y.; Wang, Z.; Zhang, G.; Ma, W.; Yan, H. A Wide-Bandgap Donor Polymer for Highly Efficient Non-Fullerene Organic Solar Cells with a Small Voltage Loss. *J. Am. Chem. Soc.* **2017**, *139* (18), 6298–6301. https://doi.org/10.1021/jacs.7b01606.

(71) Seifrid, M. T.; Oosterhout, S. D.; Toney, M. F.; Bazan, G. C. Kinetic Versus Thermodynamic Orientational Preferences for a Series of Isomorphic Molecular Semiconductors. *ACS Omega* **2018**, *3* (8), 10198–10204. https://doi.org/10.1021/acsomega.8b01435.

(72) Ying, L.; Hsu, B. B. Y.; Zhan, H.; Welch, G. C.; Zalar, P.; Perez, L. A.; Kramer, E. J.; Nguyen, T.-Q.; Heeger, A. J.; Wong, W.-Y.; Bazan, G. C. Regioregular Pyridal[2,1,3]Thiadiazole π-Conjugated Copolymers. *J. Am. Chem. Soc.* **2011**, *133* (46), 18538–18541. https://doi.org/10.1021/ja207543g.

(73) Liu, Y.; Li, M.; Yang, J.; Xue, W.; Feng, S.; Song, J.; Tang, Z.; Ma, W.; Bo, Z. High-Efficiency As-Cast Organic Solar Cells Based on Acceptors with Steric Hindrance Induced Planar Terminal Group. *Adv. Energy Mater.* **2019**, *9* (32), 1901280. https://doi.org/10.1002/aenm.201901280.

(74) Cardona, C. M.; Li, W.; Kaifer, A. E.; Stockdale, D.; Bazan, G. C. Electrochemical Considerations for Determining Absolute Frontier Orbital Energy Levels of Conjugated Polymers for Solar Cell Applications. *Adv. Mater.* **2011**, *23* (20), 2367–2371. https://doi.org/10.1002/adma.201004554.

(75) Yang, Y.; Zhang, Z.-G.; Bin, H.; Chen, S.; Gao, L.; Xue, L.; Yang, C.; Li, Y. Side-Chain Isomerization on an n-Type Organic Semiconductor ITIC Acceptor Makes 11.77% High

Efficiency Polymer Solar Cells. *J. Am. Chem. Soc.* **2016**, *138* (45), 15011–15018. https://doi.org/10.1021/jacs.6b09110.

(76) Lin, Y.; Wang, J.; Zhang, Z.-G.; Bai, H.; Li, Y.; Zhu, D.; Zhan, X. An Electron Acceptor Challenging Fullerenes for Efficient Polymer Solar Cells. *Adv. Mater.* **2015**, *27* (7), 1170–1174. https://doi.org/10.1002/adma.201404317.

(77) Song, X.; Gasparini, N.; Ye, L.; Yao, H.; Hou, J.; Ade, H.; Baran, D. Controlling Blend Morphology for Ultrahigh Current Density in Nonfullerene Acceptor-Based Organic Solar Cells. *ACS Energy Lett.* **2018**, *3* (3), 669–676. https://doi.org/10.1021/acsenergylett.7b01266.

(78) Kini, G. P.; Jeon, S. J.; Moon, D. K. Latest Progress on Photoabsorbent Materials for Multifunctional Semitransparent Organic Solar Cells. *Adv. Funct. Mater.* **2021**, *31* (15), 2007931. https://doi.org/10.1002/adfm.202007931.

(79) Li, Y.; He, C.; Zuo, L.; Zhao, F.; Zhan, L.; Li, X.; Xia, R.; Yip, H.-L.; Li, C.-Z.; Liu, X.; Chen, H. High-Performance Semi-Transparent Organic Photovoltaic Devices via Improving Absorbing Selectivity. *Adv. Energy Mater.* **2021**, *11* (11), 2003408. https://doi.org/10.1002/aenm.202003408.

(80) Wu, Y.; Yang, H.; Zou, Y.; Dong, Y.; Yuan, J.; Cui, C.; Li, Y. A New Dialkylthio-Substituted Naphtho[2,3- c]Thiophene-4,9-Dione Based Polymer Donor for High-Performance Polymer Solar Cells. *Energy Environ. Sci.* **2019**, *12* (2), 675–683. https://doi.org/10.1039/C8EE03608J.

(81) Wang, J.; Zhang, J.; Xiao, Y.; Xiao, T.; Zhu, R.; Yan, C.; Fu, Y.; Lu, G.; Lu, X.; Marder, S. R.; Zhan, X. Effect of Isomerization on High-Performance Nonfullerene Electron Acceptors. *J. Am. Chem. Soc.* **2018**, *140* (29), 9140–9147. https://doi.org/10.1021/jacs.8b04027.

(82) Liu, G.; Li, T.; Zhan, X.; Wu, H.; Cao, Y. High-Sensitivity Visible–Near Infrared Organic Photodetectors Based on Non-Fullerene Acceptors. *ACS Appl. Mater. Interfaces* **2020**, *12* (15), 17769–17775. https://doi.org/10.1021/acsami.0c00191.

(83) Bristow, H.; Thorley, K. J.; White, A. J. P.; Wadsworth, A.; Babics, M.; Hamid, Z.; Zhang, W.; Paterson, A. F.; Kosco, J.; Panidi, J.; Anthopoulos, T. D.; McCulloch, I. Impact of Nonfullerene Acceptor Side Chain Variation on Transistor Mobility. *Adv. Electron. Mater.* **2019**, *5* (10), 1900344. https://doi.org/10.1002/aelm.201900344.

(84) Martino, N.; Ghezzi, D.; Benfenati, F.; Lanzani, G.; R. Antognazza, M. Organic Semiconductors for Artificial Vision. *J. Mater. Chem. B* **2013**, *1* (31), 3768–3780. https://doi.org/10.1039/C3TB20213E.

(85) Park, S.; Fukuda, K.; Wang, M.; Lee, C.; Yokota, T.; Jin, H.; Jinno, H.; Kimura, H.; Zalar, P.; Matsuhisa, N.; Umezu, S.; Bazan, G. C.; Someya, T. Ultraflexible Near-Infrared

Organic Photodetectors for Conformal Photoplethysmogram Sensors. *Adv. Mater.* **2018**, *30* (34), 1802359. https://doi.org/10.1002/adma.201802359.

(86) Huang, Z.; Carey, J. E.; Liu, M.; Guo, X.; Mazur, E.; Campbell, J. C. Microstructured Silicon Photodetector. *Appl. Phys. Lett.* **2006**, *89* (3), 033506. https://doi.org/10.1063/1.2227629.

(87) Geum, D.-M.; Kim, S.; Kim, S. K.; Kang, S.; Kyhm, J.; Song, J.; Choi, W. J.; Yoon, E. Monolithic Integration of Visible GaAs and Near-Infrared InGaAs for Multicolor Photodetectors by Using High-Throughput Epitaxial Lift-off toward High-Resolution Imaging Systems. *Sci. Rep.* **2019**, *9* (1), 18661. https://doi.org/10.1038/s41598-019-55159-x.

(88) Allen, J. Photoplethysmography and Its Application in Clinical Physiological Measurement. *Physiol. Meas.* **2007**, *28* (3), R1. https://doi.org/10.1088/0967-3334/28/3/R01.

(89) Welch, G. C.; Bakus, R. C.; Teat, S. J.; Bazan, G. C. Impact of Regiochemistry and Isoelectronic Bridgehead Substitution on the Molecular Shape and Bulk Organization of Narrow Bandgap Chromophores. *J. Am. Chem. Soc.* **2013**, *135* (6), 2298–2305. https://doi.org/10.1021/ja310694t.

(90) Sun, H.; Ryno, S.; Zhong, C.; Ravva, M. K.; Sun, Z.; Körzdörfer, T.; Brédas, J.-L. Ionization Energies, Electron Affinities, and Polarization Energies of Organic Molecular Crystals: Quantitative Estimations from a Polarizable Continuum Model (PCM)-Tuned Range-Separated Density Functional Approach. *J. Chem. Theory Comput.* **2016**, *12* (6), 2906–2916. https://doi.org/10.1021/acs.jctc.6b00225.

(91) Patel, D. G. (Dan); Feng, F.; Ohnishi, Y.; Abboud, K. A.; Hirata, S.; Schanze, K. S.; Reynolds, J. R. It Takes More Than an Imine: The Role of the Central Atom on the Electron-Accepting Ability of Benzotriazole and Benzothiadiazole Oligomers. *J. Am. Chem. Soc.* **2012**, *134* (5), 2599–2612. https://doi.org/10.1021/ja207978v.

(92) Wang, B.; Feng, G.; Seifrid, M.; Wang, M.; Liu, B.; Bazan, G. C. Antibacterial Narrow-Band-Gap Conjugated Oligoelectrolytes with High Photothermal Conversion Efficiency. *Angew. Chem. Int. Ed.* **2017**, *56* (50), 16063–16066. https://doi.org/10.1002/anie.201709887.

(93) Kaltenbrunner, M.; White, M. S.; Głowacki, E. D.; Sekitani, T.; Someya, T.; Sariciftci, N. S.; Bauer, S. Ultrathin and Lightweight Organic Solar Cells with High Flexibility. *Nat. Commun.* **2012**, *3* (1), 770. https://doi.org/10.1038/ncomms1772.

(94) Kaltenbrunner, M.; Sekitani, T.; Reeder, J.; Yokota, T.; Kuribara, K.; Tokuhara, T.; Drack, M.; Schwödiauer, R.; Graz, I.; Bauer-Gogonea, S.; Bauer, S.; Someya, T. An Ultra-Lightweight Design for Imperceptible Plastic Electronics. *Nature* **2013**, *499* (7459), 458–463. https://doi.org/10.1038/nature12314.

(95) Li, W.; Ye, L.; Wang, T. Morphological Characterization and Manipulation of Organic Solar Cells. In *Organic Solar Cells*; John Wiley & Sons, Ltd, 2022; pp 519–554. https://doi.org/10.1002/9783527833658.ch14.

(96) Ma, X.; Kong, J.; Wang, W.; Li, X. Green-Solvent Engineering for Depositing Qualified Phenyl-C61-Butyl Acid Methyl Ester Films for Inverted Flexible Perovskite Solar Cells. *ACS Appl. Mater. Interfaces* **2023**, *15* (1), 1042–1052. https://doi.org/10.1021/acsami.2c17694.

(97) Duan, C.; Cai, W.; Y. Hsu, B. B.; Zhong, C.; Zhang, K.; Liu, C.; Hu, Z.; Huang, F.; C. Bazan, G.; J. Heeger, A.; Cao, Y. Toward Green Solvent Processable Photovoltaic Materials for Polymer Solar Cells: The Role of Highly Polar Pendant Groups in Charge Carrier Transport and Photovoltaic Behavior. *Energy Environ. Sci.* **2013**, *6* (10), 3022–3034. https://doi.org/10.1039/C3EE41838C.

(98) Chen, X.; Liu, X.; Burgers, M. A.; Huang, Y.; Bazan, G. C. Green-Solvent-Processed Molecular Solar Cells. *Angew. Chem. Int. Ed.* **2014**, *53* (52), 14378–14381. https://doi.org/10.1002/anie.201409208.

(99) Nguyen, T. L.; Lee, C.; Kim, H.; Kim, Y.; Lee, W.; Oh, J. H.; Kim, B. J.; Woo, H. Y. Ethanol-Processable, Highly Crystalline Conjugated Polymers for Eco-Friendly Fabrication of Organic Transistors and Solar Cells. *Macromolecules* **2017**, *50* (11), 4415–4424. https://doi.org/10.1021/acs.macromol.7b00452.

(100) Li, Z.; Ying, L.; Zhu, P.; Zhong, W.; Li, N.; Liu, F.; Huang, F.; Cao, Y. A Generic Green Solvent Concept Boosting the Power Conversion Efficiency of All-Polymer Solar Cells to 11%. *Energy Environ. Sci.* **2019**, *12* (1), 157–163. https://doi.org/10.1039/C8EE02863J.

(101) Walker, B.; Tamayo, A.; Duong, D. T.; Dang, X.-D.; Kim, C.; Granstrom, J.; Nguyen, T.-Q. A Systematic Approach to Solvent Selection Based on Cohesive Energy Densities in a Molecular Bulk Heterojunction System. *Adv. Energy Mater.* **2011**, *1* (2), 221–229. https://doi.org/10.1002/aenm.201000054.

(102) Sun, H.; Zhong, C.; Brédas, J.-L. Reliable Prediction with Tuned Range-Separated Functionals of the Singlet–Triplet Gap in Organic Emitters for Thermally Activated Delayed Fluorescence. *J. Chem. Theory Comput.* **2015**, *11* (8), 3851–3858. https://doi.org/10.1021/acs.jctc.5b00431.

(103) Jackson, N. E.; Savoie, B. M.; Kohlstedt, K. L.; Olvera de la Cruz, M.; Schatz, G. C.; Chen, L. X.; Ratner, M. A. Controlling Conformations of Conjugated Polymers and Small Molecules: The Role of Nonbonding Interactions. *J. Am. Chem. Soc.* **2013**, *135* (28), 10475–10483. https://doi.org/10.1021/ja403667s.

(104) Li, S.; Ye, L.; Zhao, W.; Zhang, S.; Ade, H.; Hou, J. Significant Influence of the Methoxyl Substitution Position on Optoelectronic Properties and Molecular Packing of Small-

Molecule Electron Acceptors for Photovoltaic Cells. *Adv. Energy Mater.* **2017**, *7* (17), 1700183. https://doi.org/10.1002/aenm.201700183.

(105) Wang, T.; Brédas, J.-L. Nonfullerene Small-Molecule Acceptors for Organic Photovoltaics: Understanding the Impact of Methoxy Substitution Position on Molecular Packing and Electron-Transfer Properties. *Adv. Funct. Mater.* **2019**, *29* (9), 1806845. https://doi.org/10.1002/adfm.201806845.

(106) Cui, Y.; Zhu, P.; Liao, X.; Chen, Y. Recent Advances of Computational Chemistry in Organic Solar Cell Research. *J. Mater. Chem. C* **2020**, *8* (45), 15920–15939. https://doi.org/10.1039/D0TC03709E.

(107) Kunz, T. Full Functionalization of the Thieno[3,2-b]Thiophene Scaffold. Benzo[b]Thiophenes via Intramolecular Carbomagnesiation of Alkynyl(Aryl)Thioethers. Preparation and Reactions of Solid Organozinc Reagents.

(108) Li, T.; Zhang, H.; Xiao, Z.; Rech, J. J.; Niu, H.; You, W.; Ding, L. A Carbon–Oxygen-Bridged Hexacyclic Ladder-Type Building Block for Low-Bandgap Nonfullerene Acceptors. *Mater. Chem. Front.* **2018**, *2* (4), 700–703. https://doi.org/10.1039/C8QM00004B.

(109) Aleeva, Y.; Pignataro, B. Recent Advances in Upscalable Wet Methods and Ink Formulations for Printed Electronics. *J. Mater. Chem. C* **2014**, *2* (32), 6436–6453. https://doi.org/10.1039/C4TC00618F.

(110) Ng, L. W. T.; Lee, S. W.; Chang, D. W.; Hodgkiss, J. M.; Vak, D. Organic Photovoltaics' New Renaissance: Advances Toward Roll-to-Roll Manufacturing of Non-Fullerene Acceptor Organic Photovoltaics. *Adv. Mater. Technol.* **2022**, *7* (10), 2101556. https://doi.org/10.1002/admt.202101556.

(111) Zhang, H.; Yao, H.; Hou, J.; Zhu, J.; Zhang, J.; Li, W.; Yu, R.; Gao, B.; Zhang, S.; Hou, J. Over 14% Efficiency in Organic Solar Cells Enabled by Chlorinated Nonfullerene Small-Molecule Acceptors. *Adv. Mater.* **2018**, *30* (28), 1800613. https://doi.org/10.1002/adma.201800613.

(112) Wu, Z.; Yao, W.; London, A. E.; Azoulay, J. D.; Ng, T. N. Elucidating the Detectivity Limits in Shortwave Infrared Organic Photodiodes. *Adv. Funct. Mater.* **2018**, *28* (18), 1800391. https://doi.org/10.1002/adfm.201800391.

(113) Gong, X.; Tong, M.; Xia, Y.; Cai, W.; Moon, J. S.; Cao, Y.; Yu, G.; Shieh, C.-L.; Nilsson, B.; Heeger, A. J. High-Detectivity Polymer Photodetectors with Spectral Response from 300 Nm to 1450 Nm. *Science* **2009**, *325* (5948), 1665–1667. https://doi.org/10.1126/science.1176706.

(114) Zhang, J.; Tan, H. S.; Guo, X.; Facchetti, A.; Yan, H. Material Insights and Challenges for Non-Fullerene Organic Solar Cells Based on Small Molecular Acceptors. *Nat. Energy* **2018**, *3* (9), 720–731. https://doi.org/10.1038/s41560-018-0181-5.

(115) Eun, H. J.; Kye, H.; Kim, D.; Jin, I. S.; Jung, J. W.; Ko, S.-J.; Heo, J.; Kim, B.-G.; Kim, J. H. Effective Dark Current Suppression for High-Detectivity Organic Near-Infrared Photodetectors Using a Non-Fullerene Acceptor. *ACS Appl. Mater. Interfaces* **2021**, *13* (9), 11144–11150. https://doi.org/10.1021/acsami.0c22808.

(116) Anabestani, H.; Nabavi, S.; Bhadra, S. Advances in Flexible Organic Photodetectors: Materials and Applications. *Nanomaterials* **2022**, *12* (21), 3775. https://doi.org/10.3390/nano12213775.

(117) Liu, F.; Zhou, L.; Liu, W.; Zhou, Z.; Yue, Q.; Zheng, W.; Sun, R.; Liu, W.; Xu, S.; Fan, H.; Feng, L.; Yi, Y.; Zhang, W.; Zhu, X. Organic Solar Cells with 18% Efficiency Enabled by an Alloy Acceptor: A Two-in-One Strategy. *Adv. Mater.* **2021**, *33* (27), 2100830. https://doi.org/10.1002/adma.202100830.

(118) Xia, K.; Li, Y.; Wang, Y.; Portilla, L.; Pecunia, V. Narrowband-Absorption-Type Organic Photodetectors for the Far-Red Range Based on Fullerene-Free Bulk Heterojunctions. *Adv. Opt. Mater.* **2020**, *8* (8), 1902056. https://doi.org/10.1002/adom.201902056.

(119) *The integration of semi-transparent photovoltaics on greenhouse roof for energy and plant production | Elsevier Enhanced Reader*. https://doi.org/10.1016/j.renene.2018.01.044.

(120) Zhao, Y.; Cheng, P.; Yang, H.; Wang, M.; Meng, D.; Zhu, Y.; Zheng, R.; Li, T.; Zhang, A.; Tan, S.; Huang, T.; Bian, J.; Zhan, X.; Weiss, P. S.; Yang, Y. Towards High-Performance Semitransparent Organic Photovoltaics: Dual-Functional p-Type Soft Interlayer. *ACS Nano* **2022**, *16* (1), 1231–1238. https://doi.org/10.1021/acsnano.1c09018.

(121) Song, S.; Cho, H. W.; Jeong, J.; Yoon, Y. J.; Park, S. Y.; Song, S.; Woo, B. H.; Jun, Y. C.; Walker, B.; Kim, J. Y. Dichroic Sb2O3/Ag/Sb2O3 Electrodes for Colorful Semitransparent Organic Solar Cells. *Sol. RRL* **2020**, *4* (9), 2000201. https://doi.org/10.1002/solr.202000201.

(122) Yoo, G. Y.; Jeong, J.; Lee, S.; Lee, Y.; Yoon, H. C.; Chu, V. B.; Park, G. S.; Hwang, Y. J.; Kim, W.; Min, B. K.; Do, Y. R. Multiple-Color-Generating Cu(In,Ga)(S,Se)2 Thin-Film Solar Cells via Dichroic Film Incorporation for Power-Generating Window Applications. *ACS Appl. Mater. Interfaces* **2017**, *9* (17), 14817–14826. https://doi.org/10.1021/acsami.7b01416.

(123) Simone, G.; Dyson, M. J.; Meskers, S. C. J.; Janssen, R. A. J.; Gelinck, G. H. Organic Photodetectors and Their Application in Large Area and Flexible Image Sensors: The Role of Dark Current. *Adv. Funct. Mater.* **2020**, *30* (20), 1904205. https://doi.org/10.1002/adfm.201904205.

(124) Wang, C.; Zhang, X.; Hu, W. Organic Photodiodes and Phototransistors toward Infrared Detection: Materials, Devices, and Applications. *Chem. Soc. Rev.* **2020**, *49* (3), 653–670. https://doi.org/10.1039/C9CS00431A.

(125) Takacs, C. J.; Sun, Y.; Welch, G. C.; Perez, L. A.; Liu, X.; Wen, W.; Bazan, G. C.; Heeger, A. J. Solar Cell Efficiency, Self-Assembly, and Dipole–Dipole Interactions of Isomorphic Narrow-Band-Gap Molecules. *J. Am. Chem. Soc.* **2012**, *134* (40), 16597–16606. https://doi.org/10.1021/ja3050713.

(126) Duong, D. T.; Walker, B.; Lin, J.; Kim, C.; Love, J.; Purushothaman, B.; Anthony, J. E.; Nguyen, T.-Q. Molecular Solubility and Hansen Solubility Parameters for the Analysis of Phase Separation in Bulk Heterojunctions. *J. Polym. Sci. Part B Polym. Phys.* **2012**, *50* (20), 1405–1413. https://doi.org/10.1002/polb.23153.

(127) Campana, F.; Kim, C.; Marrocchi, A.; Vaccaro, L. Green Solvent-Processed Organic Electronic Devices. *J. Mater. Chem. C* **2020**, *8* (43), 15027–15047. https://doi.org/10.1039/D0TC03610B.

(128) Bernardo, G.; Lopes, T.; Lidzey, D. G.; Mendes, A. Progress in Upscaling Organic Photovoltaic Devices. *Adv. Energy Mater.* **2021**, *11* (23), 2100342. https://doi.org/10.1002/aenm.202100342.

(129) Lee, S.; Jeong, D.; Kim, C.; Lee, C.; Kang, H.; Woo, H. Y.; Kim, B. J. Eco-Friendly Polymer Solar Cells: Advances in Green-Solvent Processing and Material Design. *ACS Nano* **2020**, *14* (11), 14493–14527. https://doi.org/10.1021/acsnano.0c07488.

(130) Fan, Q.; Zhu, Q.; Xu, Z.; Su, W.; Chen, J.; Wu, J.; Guo, X.; Ma, W.; Zhang, M.; Li, Y. Chlorine Substituted 2D-Conjugated Polymer for High-Performance Polymer Solar Cells with 13.1% Efficiency via Toluene Processing. *Nano Energy* **2018**, *48*, 413–420. https://doi.org/10.1016/j.nanoen.2018.04.002.

(131) Ji, G.; Zhao, W.; Wei, J.; Yan, L.; Han, Y.; Luo, Q.; Yang, S.; Hou, J.; Ma, C.-Q. 12.88% Efficiency in Doctor-Blade Coated Organic Solar Cells through Optimizing the Surface Morphology of a ZnO Cathode Buffer Layer. *J. Mater. Chem. A* **2018**, *7* (1), 212–220. https://doi.org/10.1039/C8TA08873J.

(132) Zhou, H.; Yang, L.; Stuart, A. C.; Price, S. C.; Liu, S.; You, W. Development of Fluorinated Benzothiadiazole as a Structural Unit for a Polymer Solar Cell of 7 % Efficiency. *Angew. Chem. Int. Ed.* **2011**, *50* (13), 2995–2998. https://doi.org/10.1002/anie.201005451.

(133) Tang, M. L.; Oh, J. H.; Reichardt, A. D.; Bao, Z. Chlorination: A General Route toward Electron Transport in Organic Semiconductors. *J. Am. Chem. Soc.* **2009**, *131* (10), 3733–3740. https://doi.org/10.1021/ja809045s.

(134) Hilgeroth, P. S.; Thümmler, J. F.; Binder, W. H. 3D Printing of Triamcinolone Acetonide in Triblock Copolymers of Styrene–Isobutylene–Styrene as a Slow-Release System. *Polymers* **2022**, *14* (18), 3742. https://doi.org/10.3390/polym14183742.

(135) Verstraeten, F.; Gielen, S.; Verstappen, P.; Kesters, J.; Georgitzikis, E.; Raymakers, J.; Cheyns, D.; Malinowski, P.; Daenen, M.; Lutsen, L.; Vandewal, K.; Maes, W. Near-Infrared Organic Photodetectors Based on Bay-Annulated Indigo Showing Broadband Absorption and High Detectivities up to 1.1 Mm. *J. Mater. Chem. C* **2018**, *6* (43), 11645–11650. https://doi.org/10.1039/C8TC04164D.

(136) Lan, Z.; Lei, Y.; Chan, W. K. E.; Chen, S.; Luo, D.; Zhu, F. Near-Infrared and Visible Light Dual-Mode Organic Photodetectors. *Sci. Adv.* **2020**, *6* (5), eaaw8065. https://doi.org/10.1126/sciadv.aaw8065.

(137) Yang, C.; Liu, D.; Bates, M.; Barr, M. C.; Lunt, R. R. How to Accurately Report Transparent Solar Cells. *Joule* **2019**, *3* (8), 1803–1809. https://doi.org/10.1016/j.joule.2019.06.005.

(138) Koster, L. J. A.; Mihailetchi, V. D.; Xie, H.; Blom, P. W. M. Origin of the Light Intensity Dependence of the Short-Circuit Current of Polymer/Fullerene Solar Cells. *Appl. Phys. Lett.* **2005**, *87* (20), 203502. https://doi.org/10.1063/1.2130396.

(139) Koster, L. J. A.; Mihailetchi, V. D.; Ramaker, R.; Blom, P. W. M. Light Intensity Dependence of Open-Circuit Voltage of Polymer:Fullerene Solar Cells. *Appl. Phys. Lett.* **2005**, *86* (12), 123509. https://doi.org/10.1063/1.1889240.

(140) Brus, V. V.; Proctor, C. M.; Ran, N. A.; Nguyen, T.-Q. Capacitance Spectroscopy for Quantifying Recombination Losses in Nonfullerene Small-Molecule Bulk Heterojunction Solar Cells. *Adv. Energy Mater.* **2016**, *6* (11), 1502250. https://doi.org/10.1002/aenm.201502250.

(141) Koster, L. J. A.; Mihailetchi, V. D.; Xie, H.; Blom, P. W. M. Origin of the Light Intensity Dependence of the Short-Circuit Current of Polymer/Fullerene Solar Cells. *Appl. Phys. Lett.* **2005**, *87* (20), 203502. https://doi.org/10.1063/1.2130396.

(142) Proctor, C. M.; Nguyen, T.-Q. Effect of Leakage Current and Shunt Resistance on the Light Intensity Dependence of Organic Solar Cells. *Appl. Phys. Lett.* **2015**, *106* (8), 083301. https://doi.org/10.1063/1.4913589.

(143) Vollbrecht, J.; Brus, V. V.; Ko, S.-J.; Lee, J.; Karki, A.; Cao, D. X.; Cho, K.; Bazan, G. C.; Nguyen, T.-Q. Quantifying the Nongeminate Recombination Dynamics in Nonfullerene Bulk Heterojunction Organic Solar Cells. *Adv. Energy Mater.* **2019**, *9* (32), 1901438. https://doi.org/10.1002/aenm.201901438.

(144) Du, Z.; Mainville, M.; Vollbrecht, J.; Dixon, A. L.; Schopp, N.; Schrock, M.; Peng, Z.; Huang, J.; Chae, S.; Ade, H.; Leclerc, M.; Reddy, G. N. M.; Nguyen, T.-Q. Insights into Bulk-Heterojunction Organic Solar Cells Processed from Green Solvent. *Sol. RRL* **2021**, *5* (8), 2100213. https://doi.org/10.1002/solr.202100213.

(145) Dou, L.; Chen, C.-C.; Yoshimura, K.; Ohya, K.; Chang, W.-H.; Gao, J.; Liu, Y.; Richard, E.; Yang, Y. Synthesis of 5H-Dithieno[3,2-b:2′,3′-d]Pyran as an Electron-Rich Building Block for Donor–Acceptor Type Low-Bandgap Polymers. *Macromolecules* **2013**, *46* (9), 3384–3390. https://doi.org/10.1021/ma400452j.

(146) Sun, K.; Xiao, Z.; Lu, S.; Zajaczkowski, W.; Pisula, W.; Hanssen, E.; White, J. M.; Williamson, R. M.; Subbiah, J.; Ouyang, J.; Holmes, A. B.; Wong, W. W. H.; Jones, D. J. A Molecular Nematic Liquid Crystalline Material for High-Performance Organic Photovoltaics. *Nat. Commun.* **2015**, *6* (1), 6013. https://doi.org/10.1038/ncomms7013.

(147) Kumar, R. J.; MacDonald, J. M.; Singh, Th. B.; Waddington, L. J.; Holmes, A. B. Hierarchical Self-Assembly of Semiconductor Functionalized Peptide α-Helices and Optoelectronic Properties. *J. Am. Chem. Soc.* **2011**, *133* (22), 8564–8573. https://doi.org/10.1021/ja110858k.

(148) Yang, L.; Zhang, S.; He, C.; Zhang, J.; Yang, Y.; Zhu, J.; Cui, Y.; Zhao, W.; Zhang, H.; Zhang, Y.; Wei, Z.; Hou, J. Modulating Molecular Orientation Enables Efficient Nonfullerene Small-Molecule Organic Solar Cells. *Chem. Mater.* **2018**, *30* (6), 2129–2134. https://doi.org/10.1021/acs.chemmater.8b00287.

Mass and NMR spectra

Chapter 1

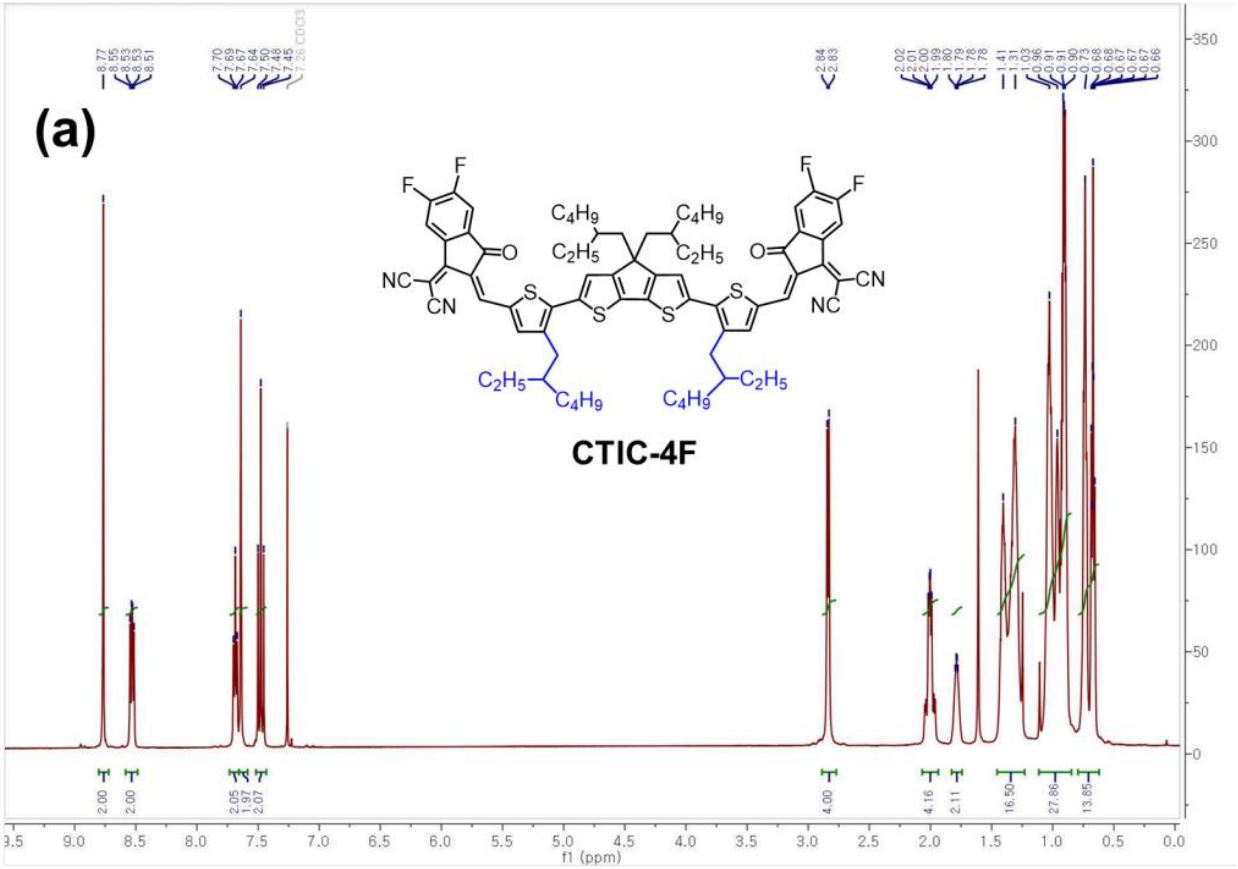
(a)
CTIC-4F
f1 (ppm)

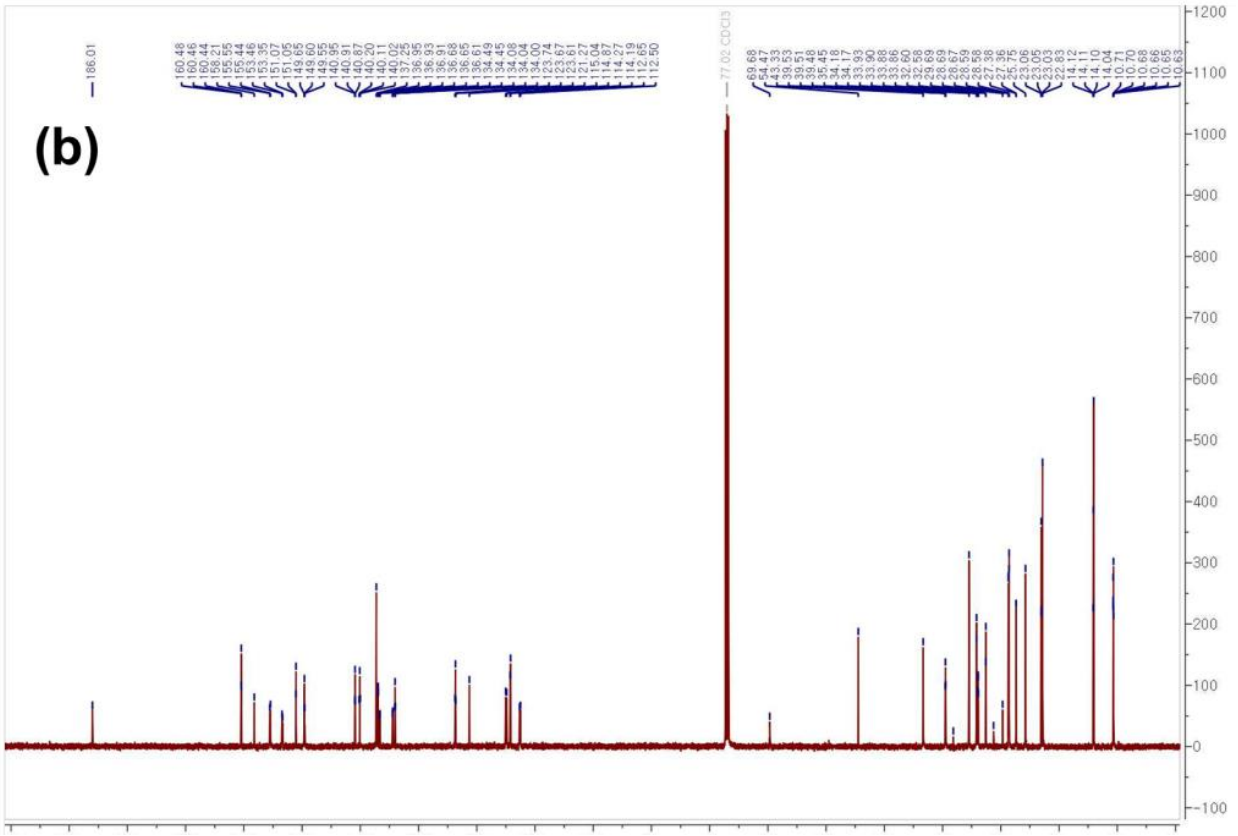
(b)

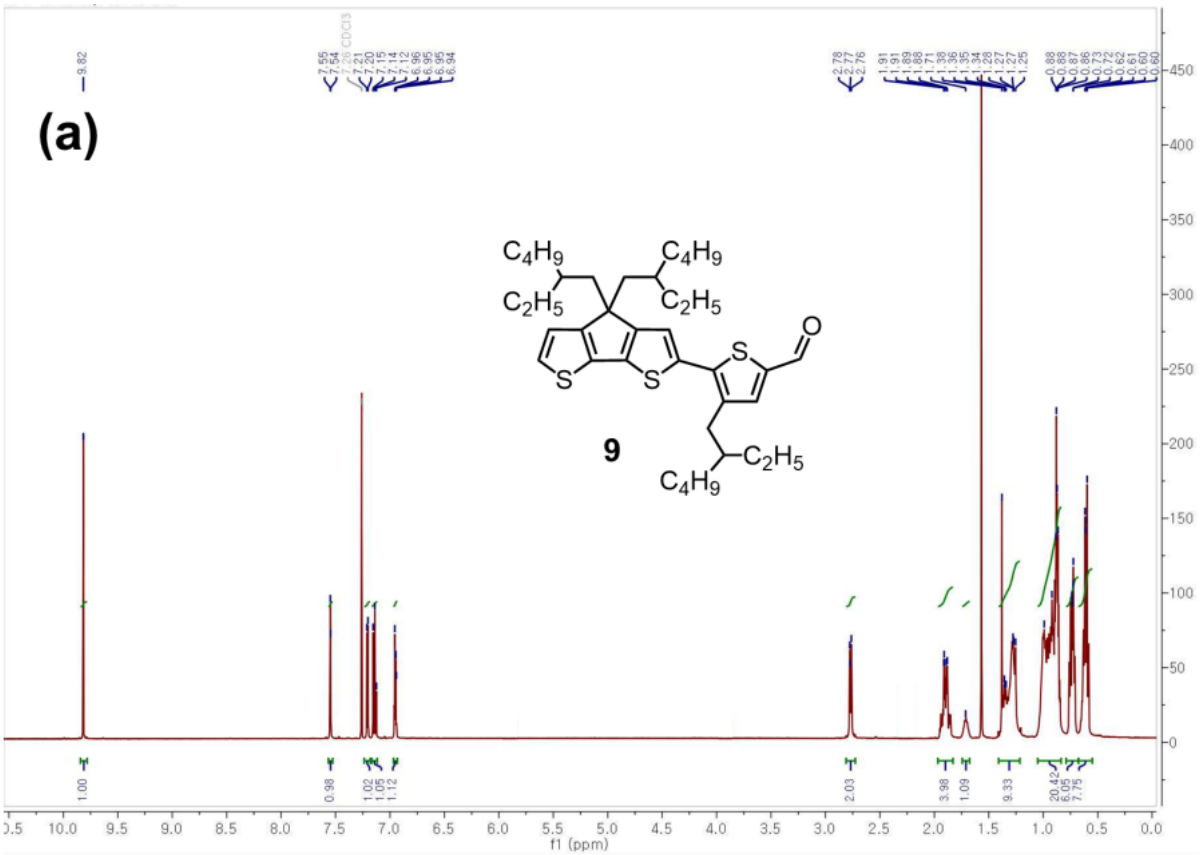
(a)
9
f1 (ppm)

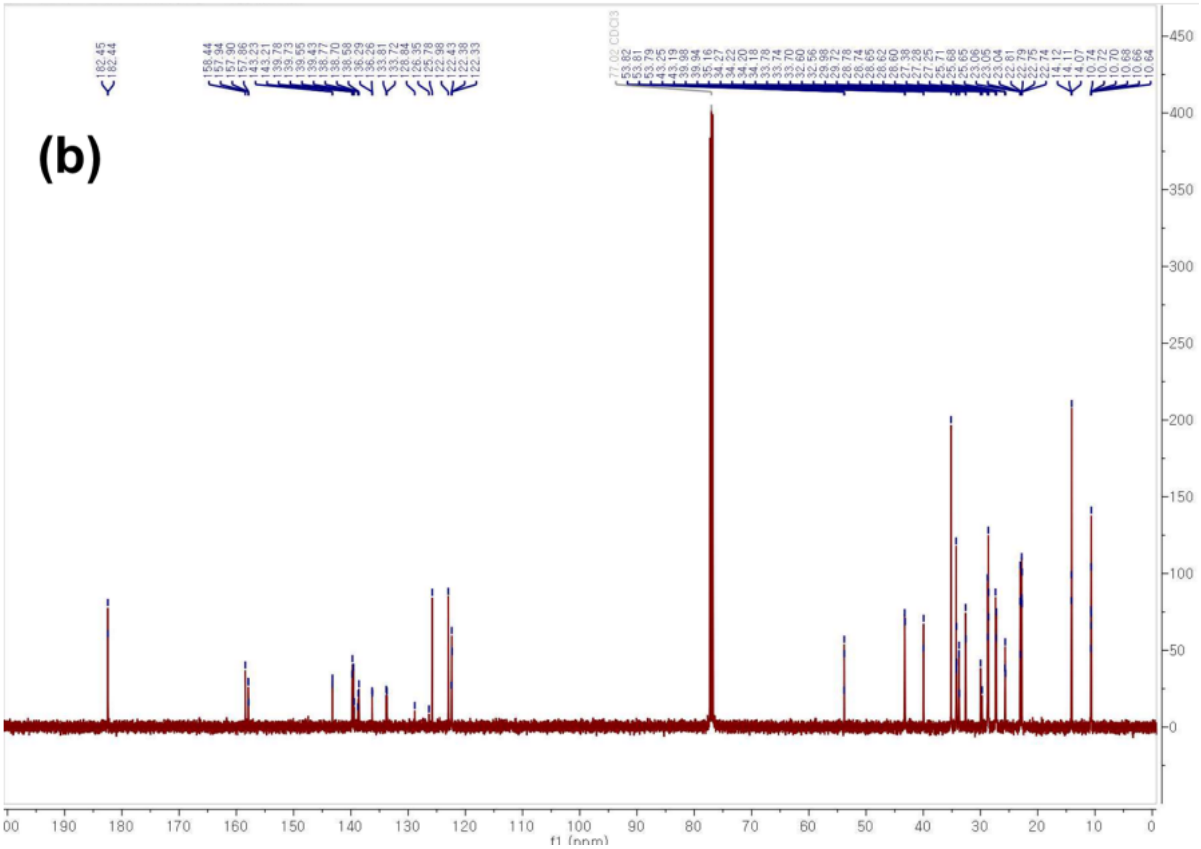
(b)
f1 (ppm)

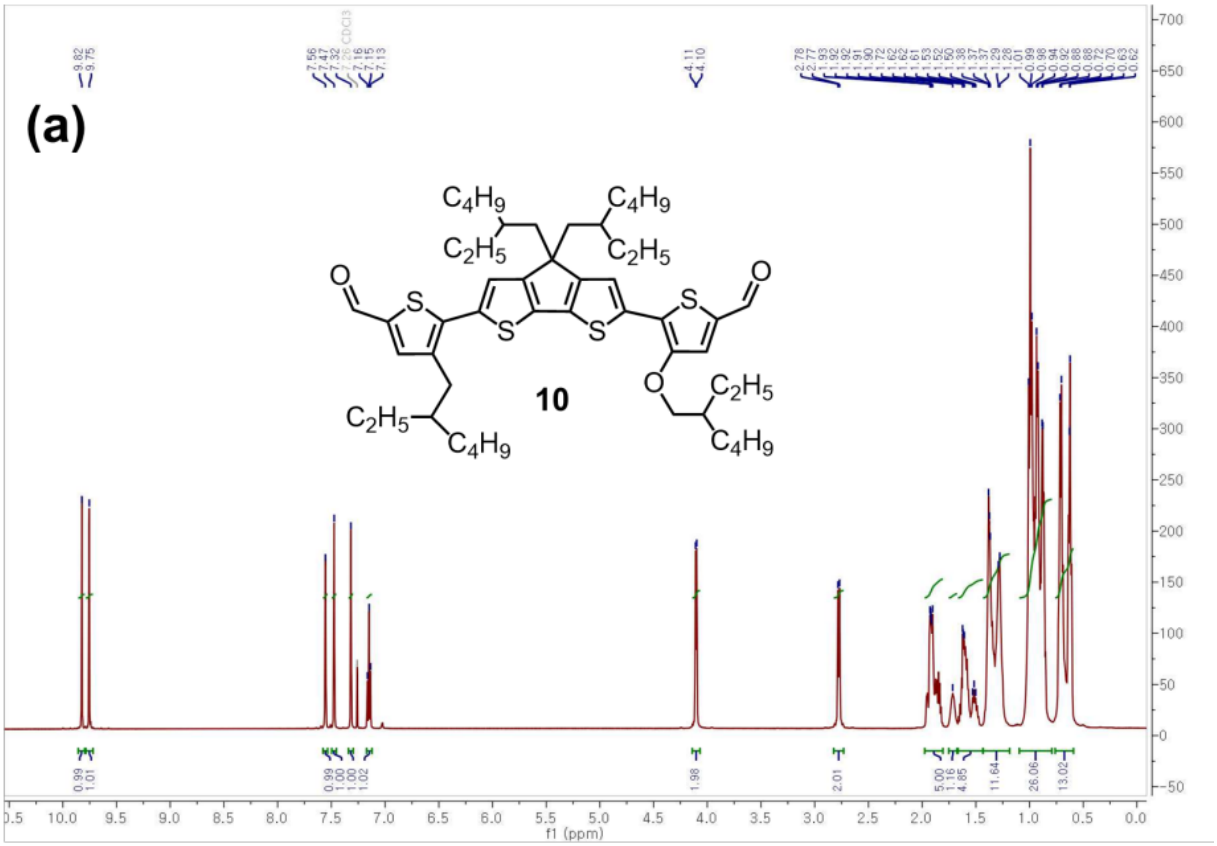
(a)
10
f1 (ppm)

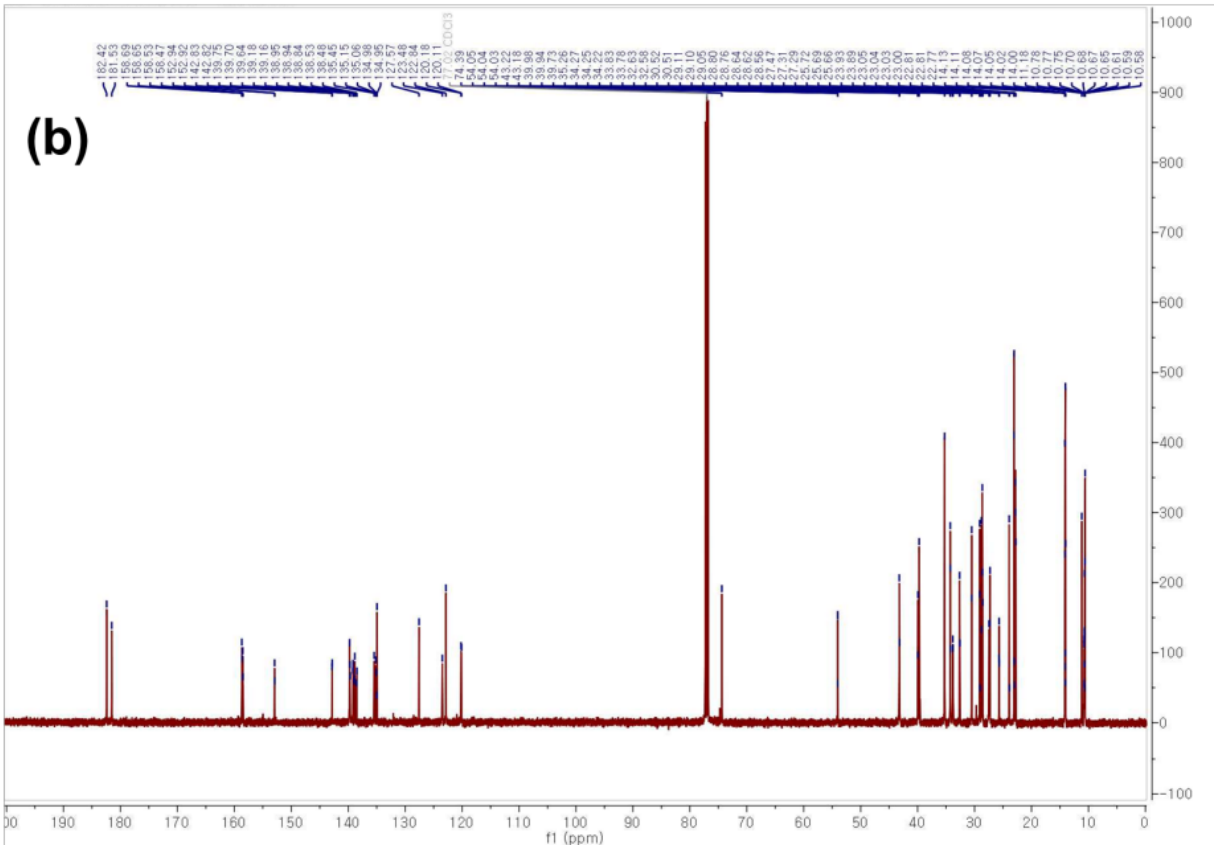
(b)
f1 (ppm)

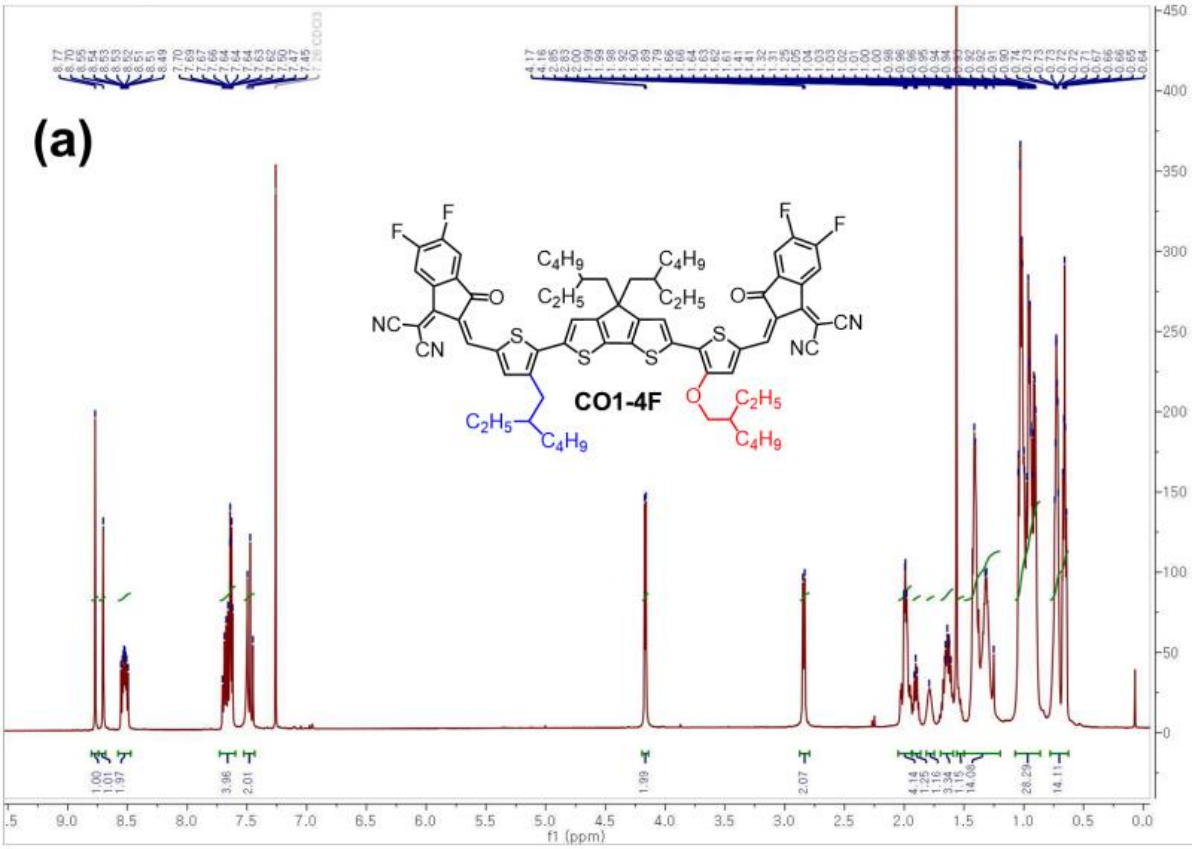
(a)
CO1-4F
f1 (ppm)

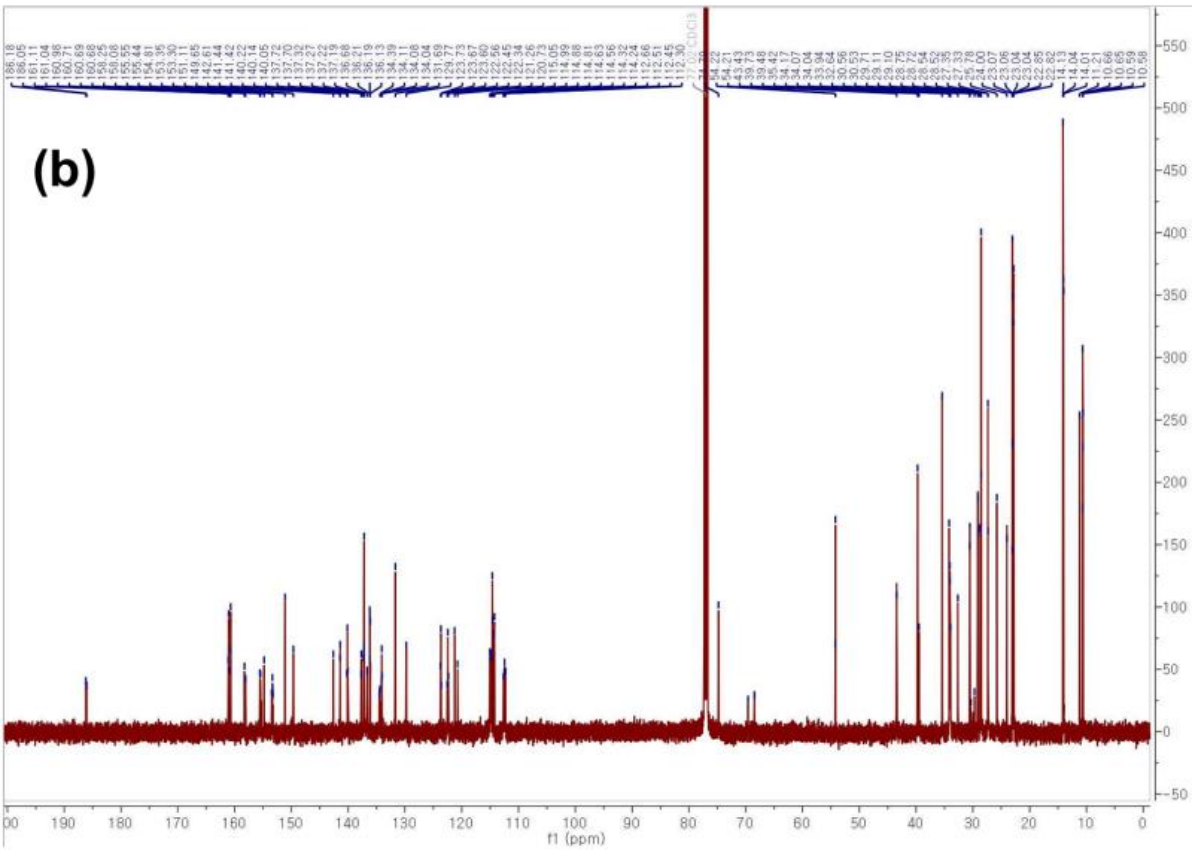
(b)
f1 (ppm)

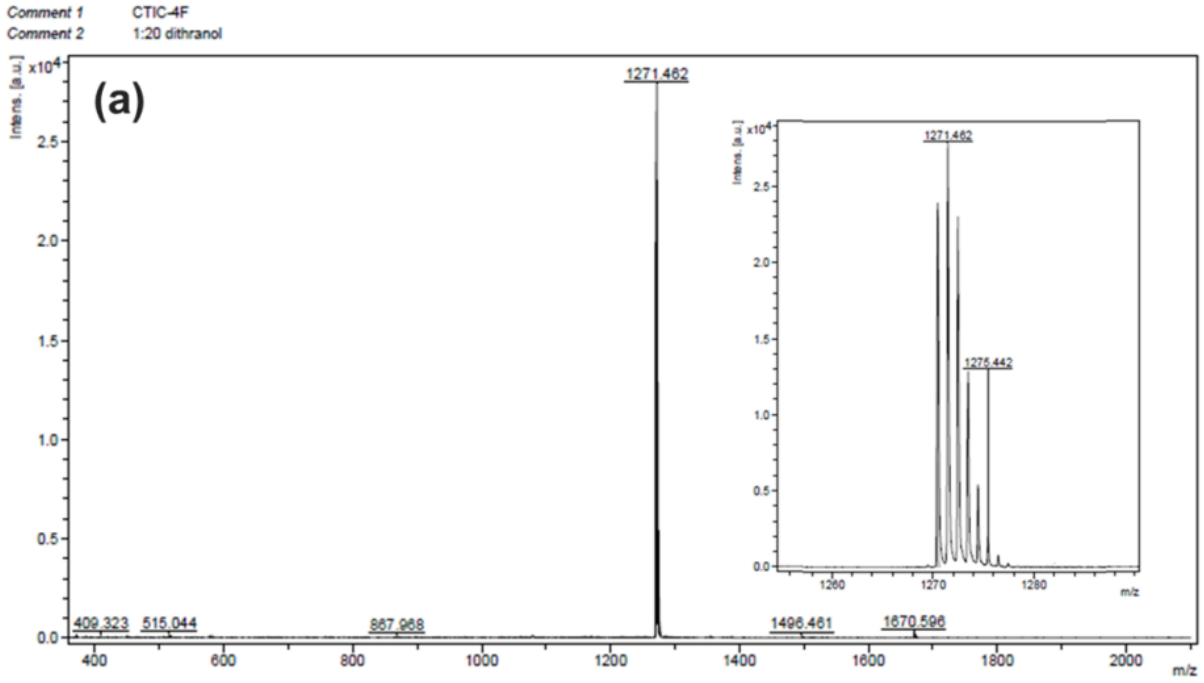
Comment 1 CTIC-4F
Comment 2 1:20 dithranol
(a)
Intens. [a.u.] x10^4
1271.462
1275.442
409.323
515.044
867.968
1496.461
1670.596
m/z

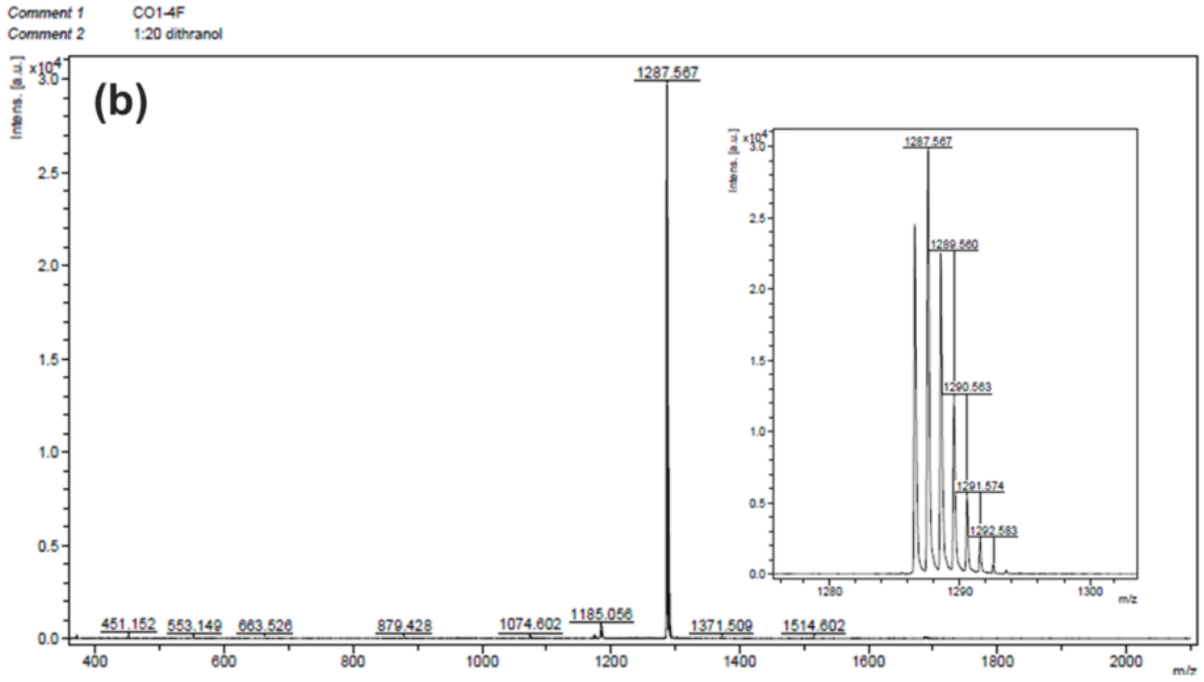
Comment 1 CO1-4F
Comment 2 1:20 dithranol
(b)
Intens. [a.u.] x10^4
1287.567
1289.560
1290.563
1291.574
1292.583
451.152
553.149
663.526
879.428
1074.602
1185.056
1371.509
1514.602
m/z

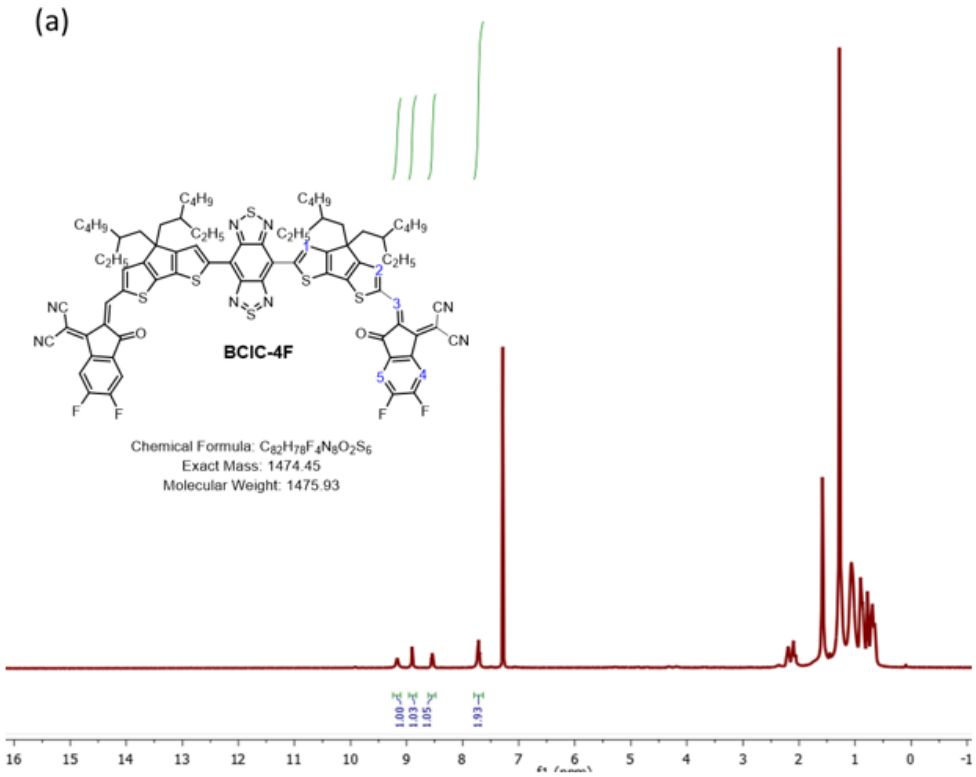
(a)
BCIC-4F
Chemical Formula: C82H78F4N8O2S6
Exact Mass: 1474.45
Molecular Weight: 1475.93
1.00
1.03
1.05
1.93
16 15 14 13 12 11 10 9 8 7 6 5 4 3 2 1 0 -1

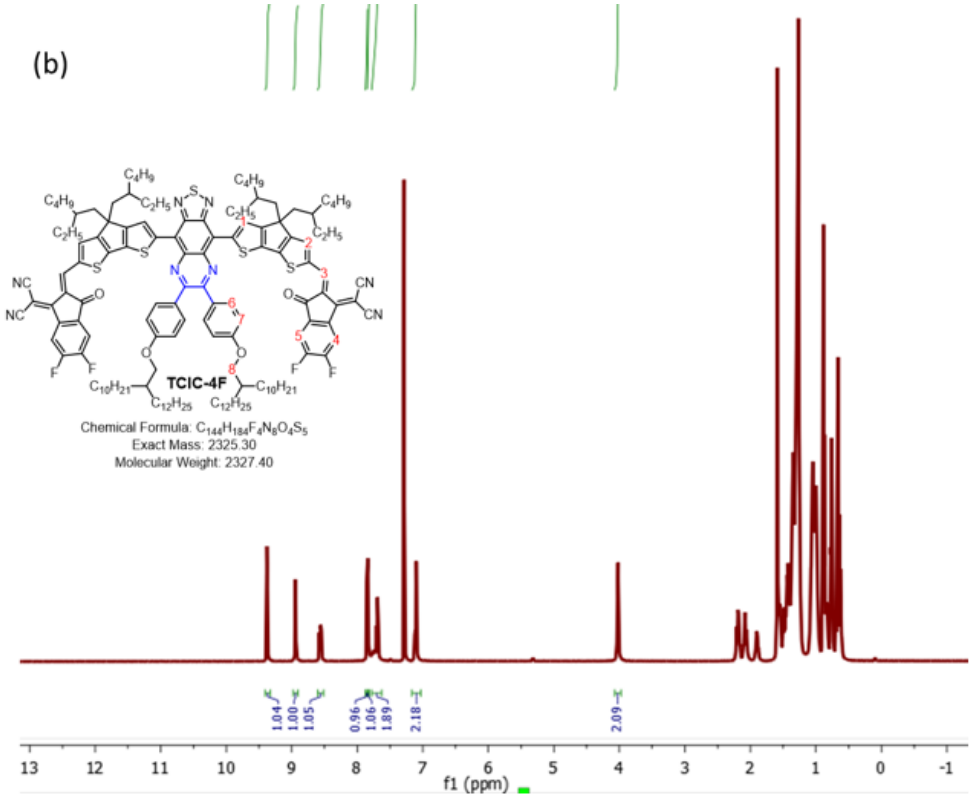
(b)
TCIC-4F
Chemical Formula: C144H184F4N8O4S5
Exact Mass: 2325.30
Molecular Weight: 2327.40
1.04
1.00
1.05
0.96
1.06
1.89
2.18
2.09
13 12 11 10 9 8 7 6 5 4 3 2 1 0 -1
f1 (ppm)

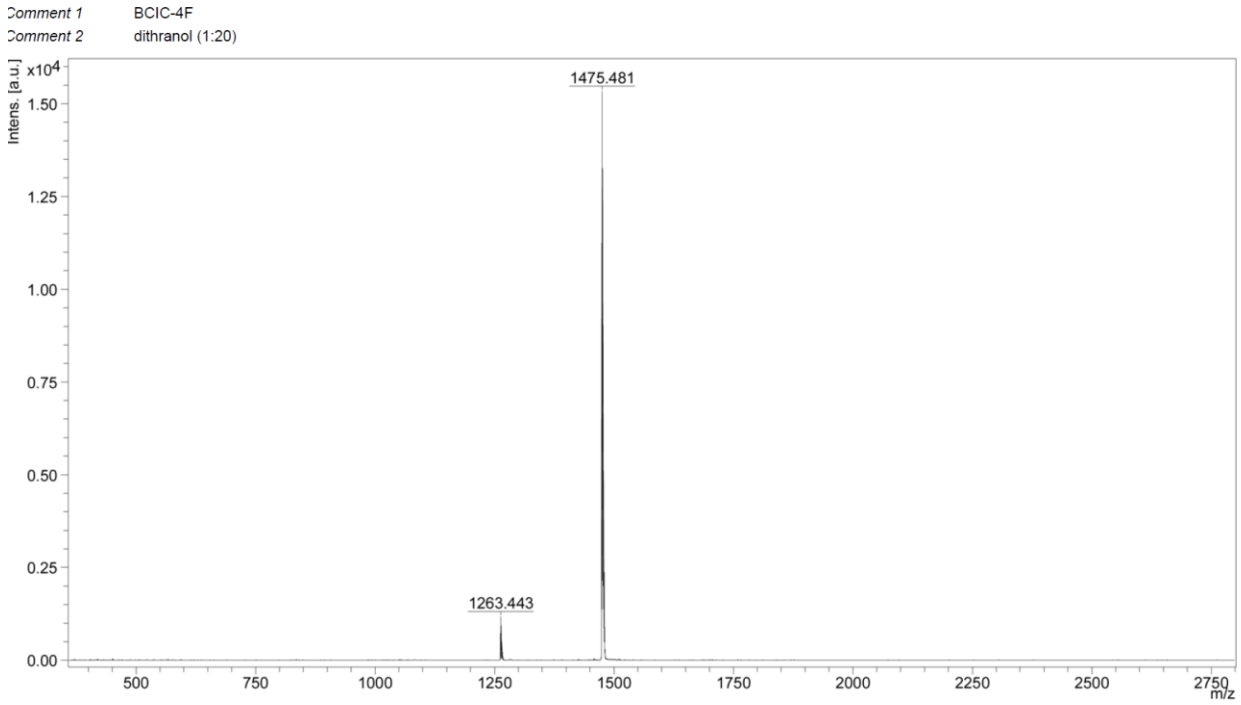
Comment 1 BCIC-4F
Comment 2 dithranol (1:20)
Intens. [a.u.]
x10^4
1.50
1.25
1.00
0.75
0.50
0.25
0.00
1475.481
1263.443
500
750
1000
1250
1500
1750
2000
2250
2500
2750
m/z

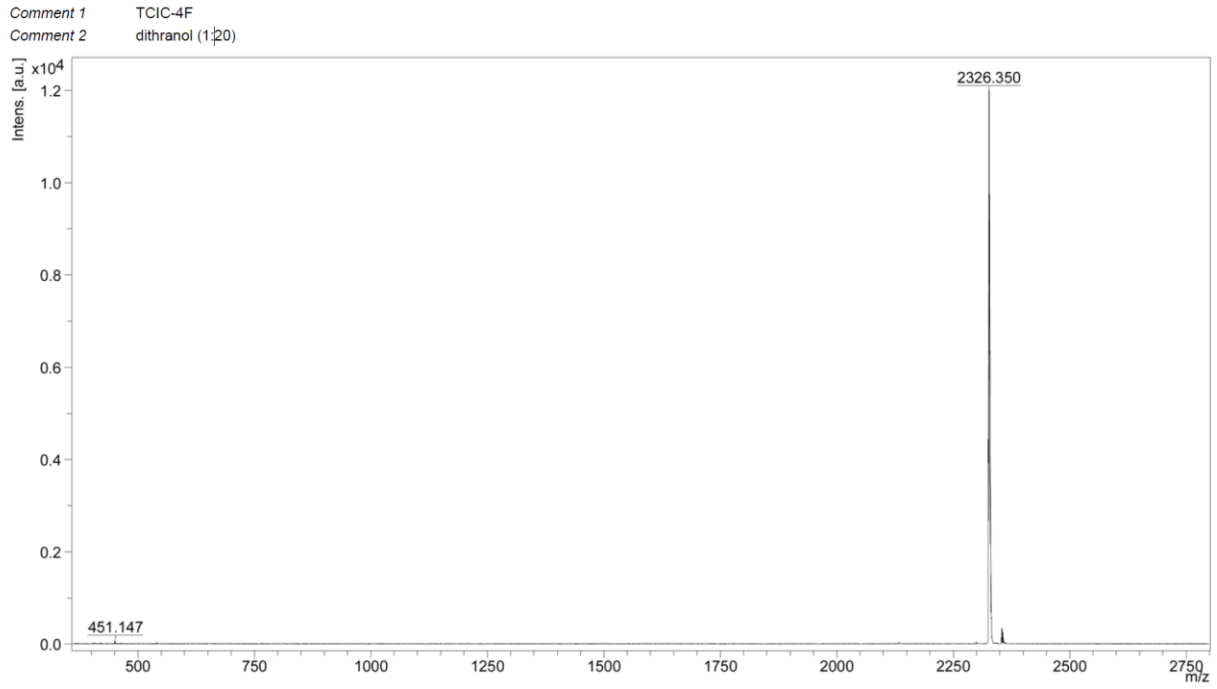
Comment 1 TCIC-4F
Comment 2 dithranol (1:20)
Intens. [a.u.]
x10^4
1.2
1.0
0.8
0.6
0.4
0.2
0.0
2326.350
451.147
500
750
1000
1250
1500
1750
2000
2250
2500
2750
m/z

Chapter 3

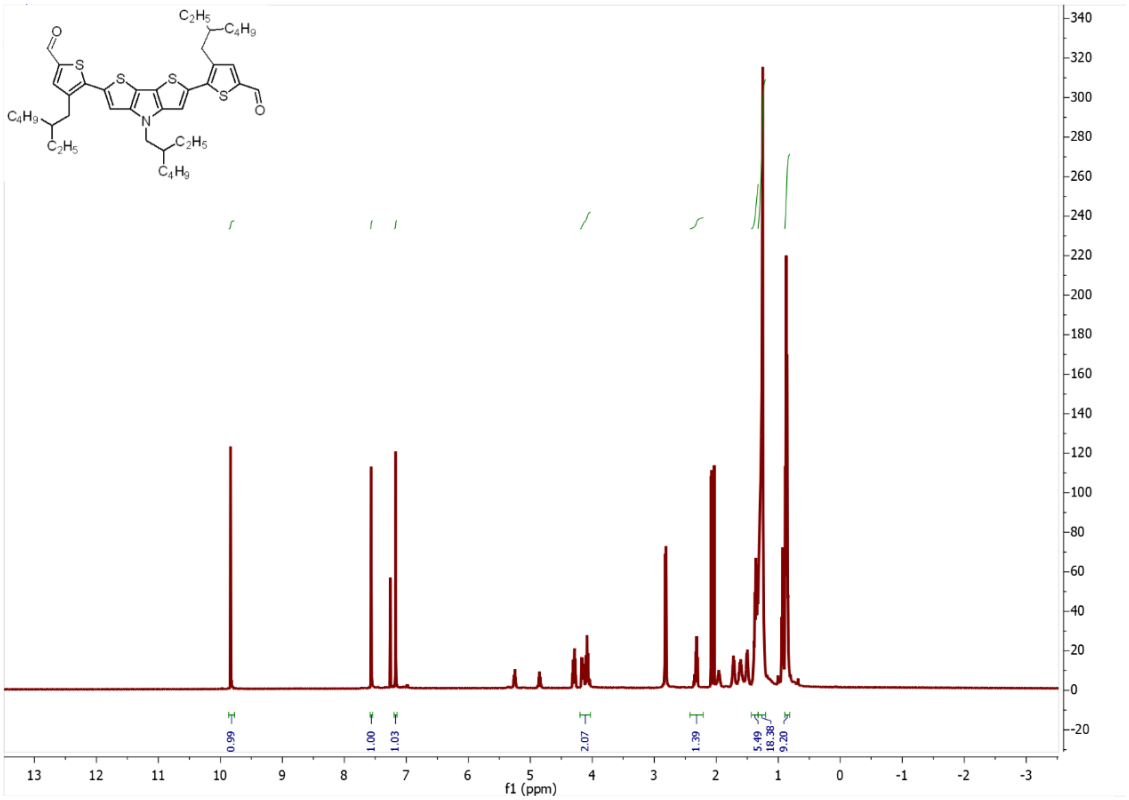

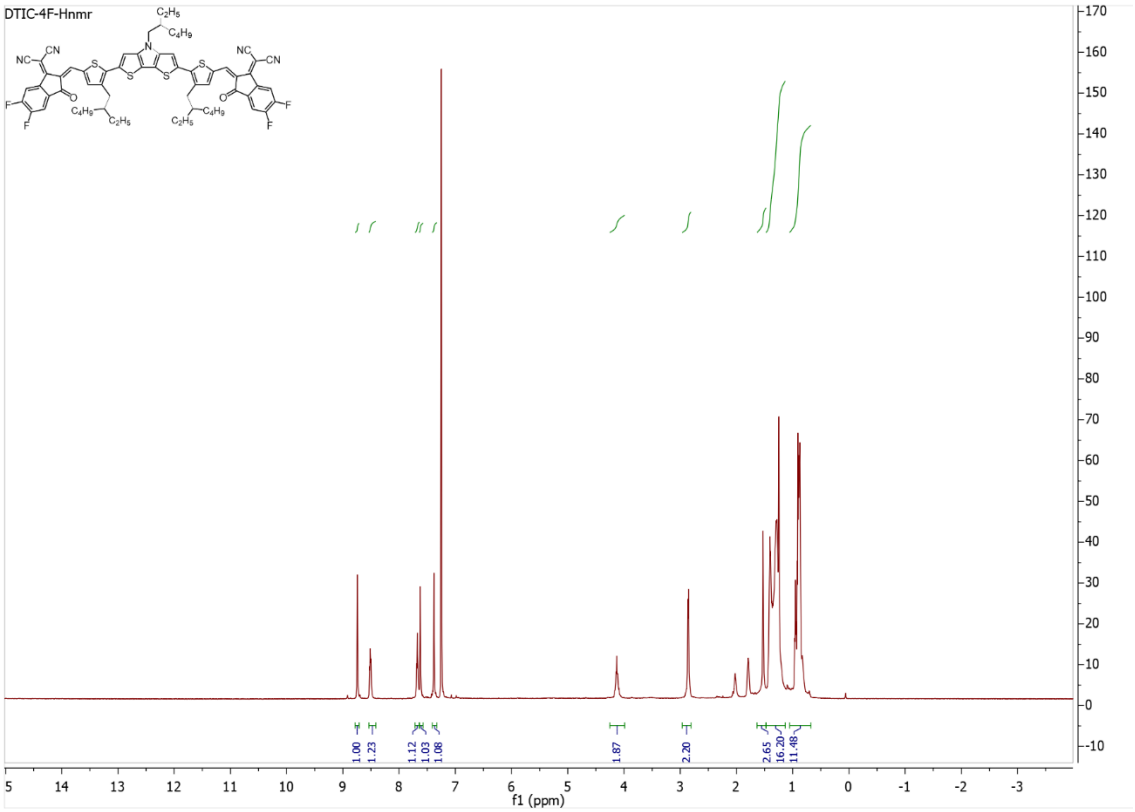

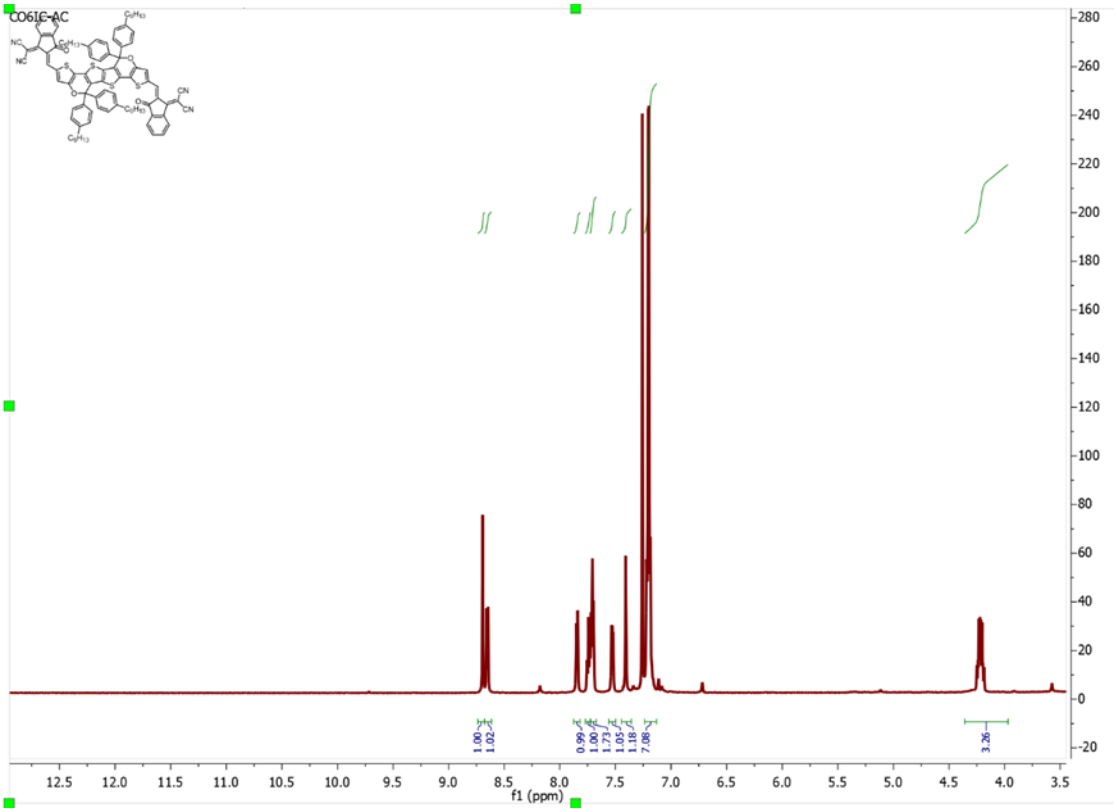
CO61C-AC
f1 (ppm)

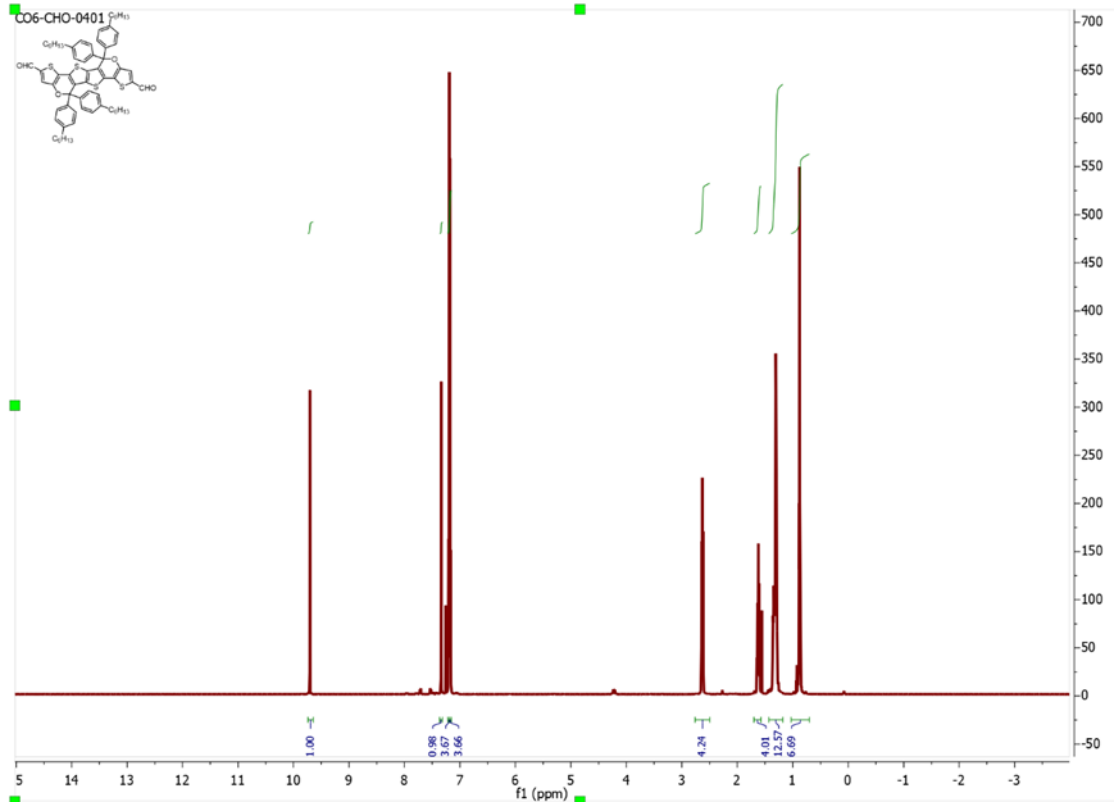
CO6-CHO-0401
f1 (ppm)

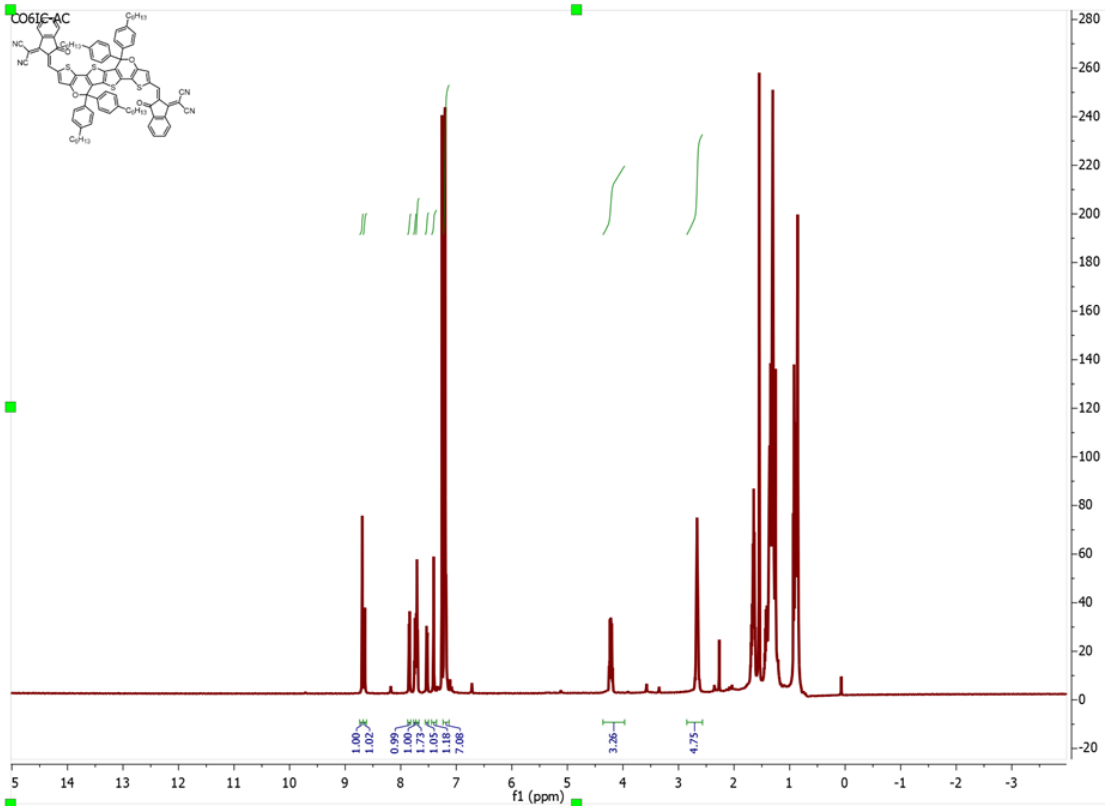
CO61C-AC
f1 (ppm)

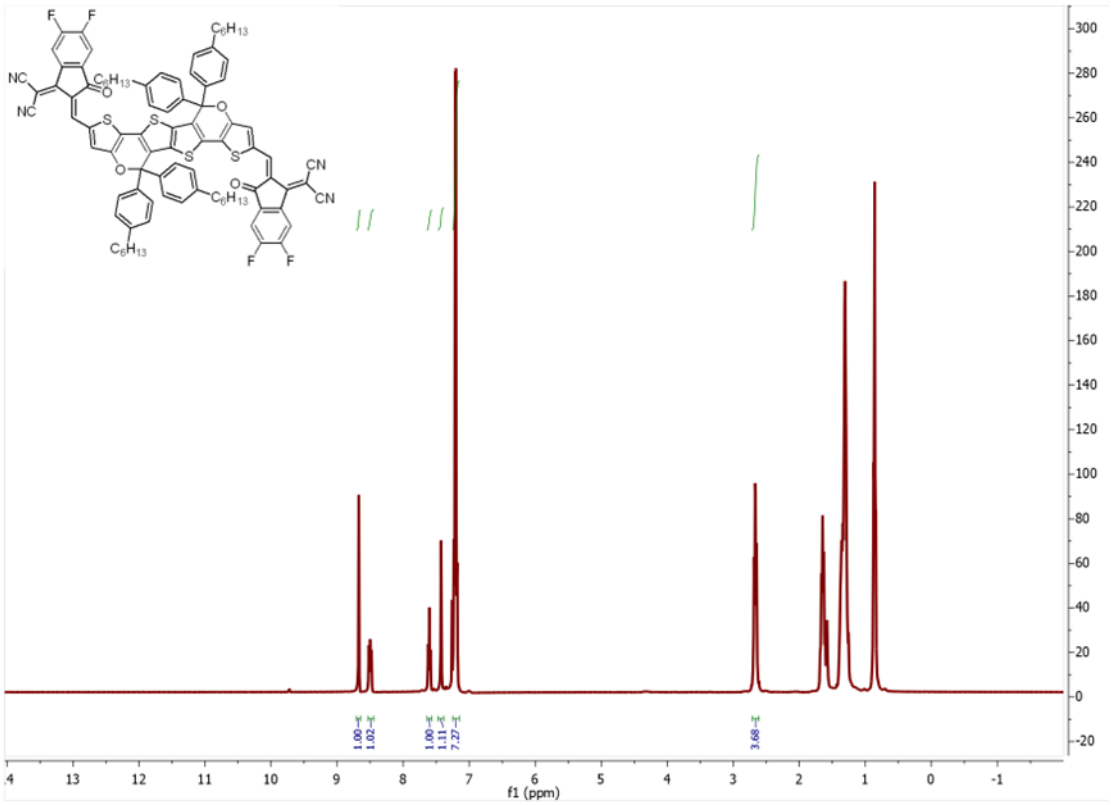
f1 (ppm)

Chapter 4

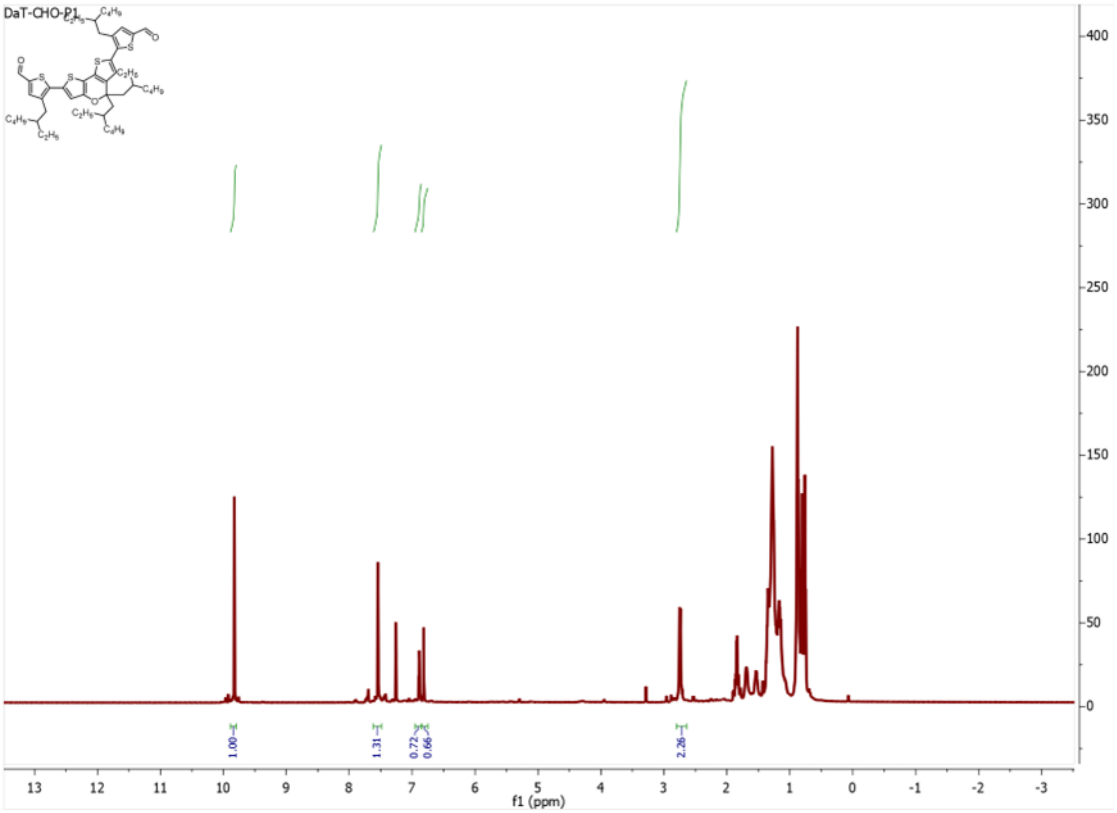
DaT-CHO-P1
1.00
1.31
0.72
0.66
2.26
f1 (ppm)

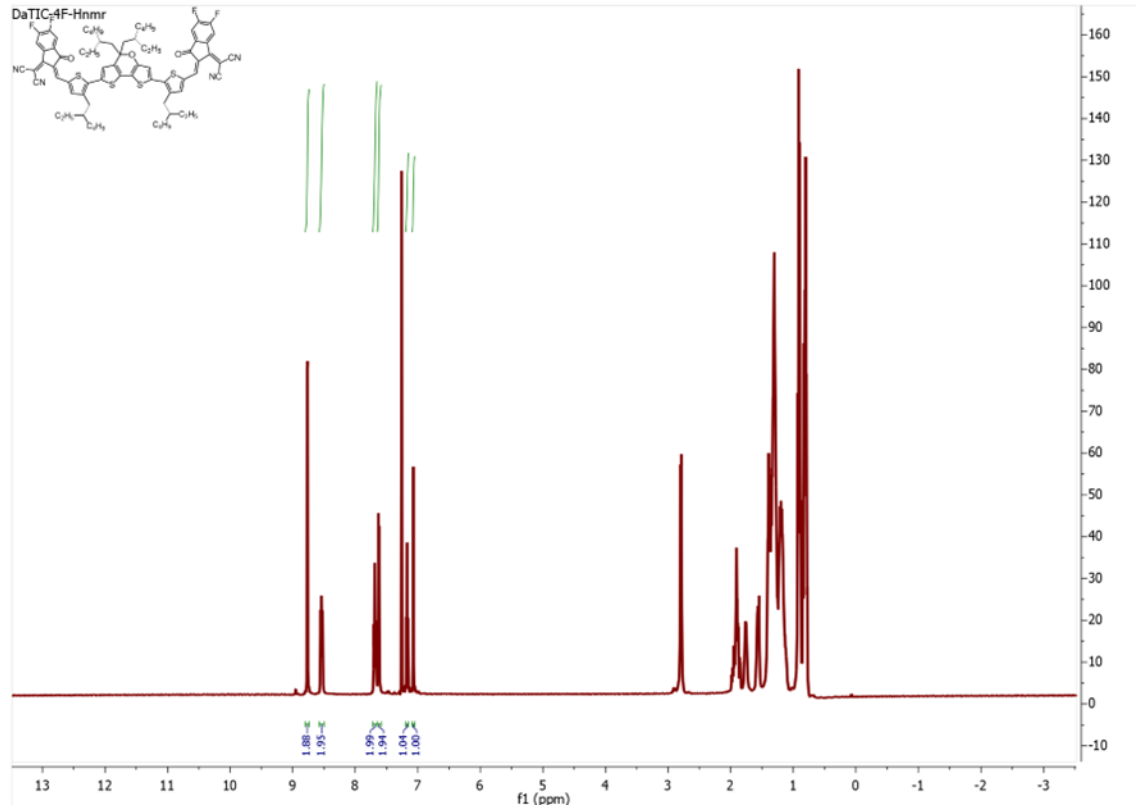
DaTIC-4F-Hnmr
1.88
1.95
1.99
1.94
1.04
1.00
f1 (ppm)

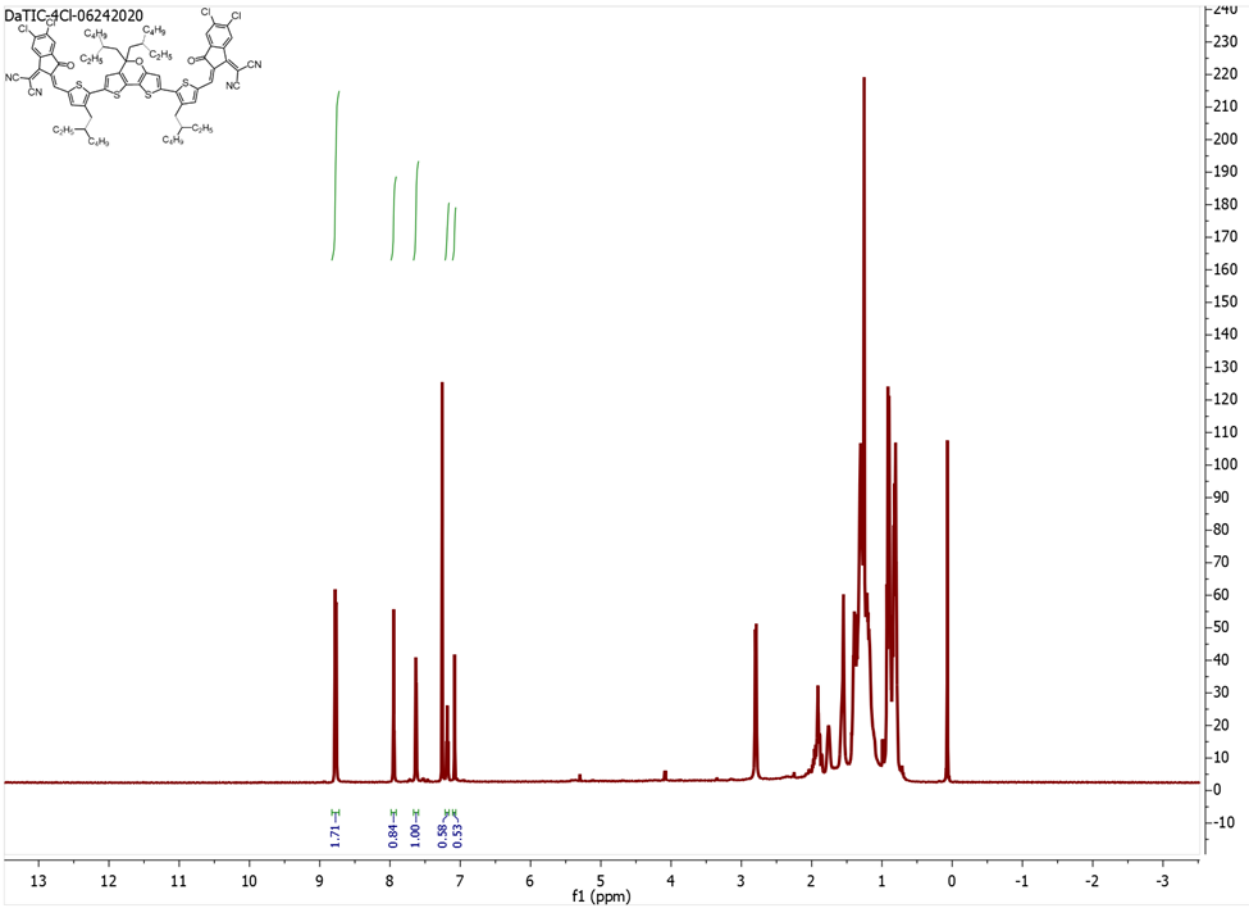
DaTIC-4Cl-06242020
1.71
0.84
1.00
0.58
0.53
f1 (ppm)

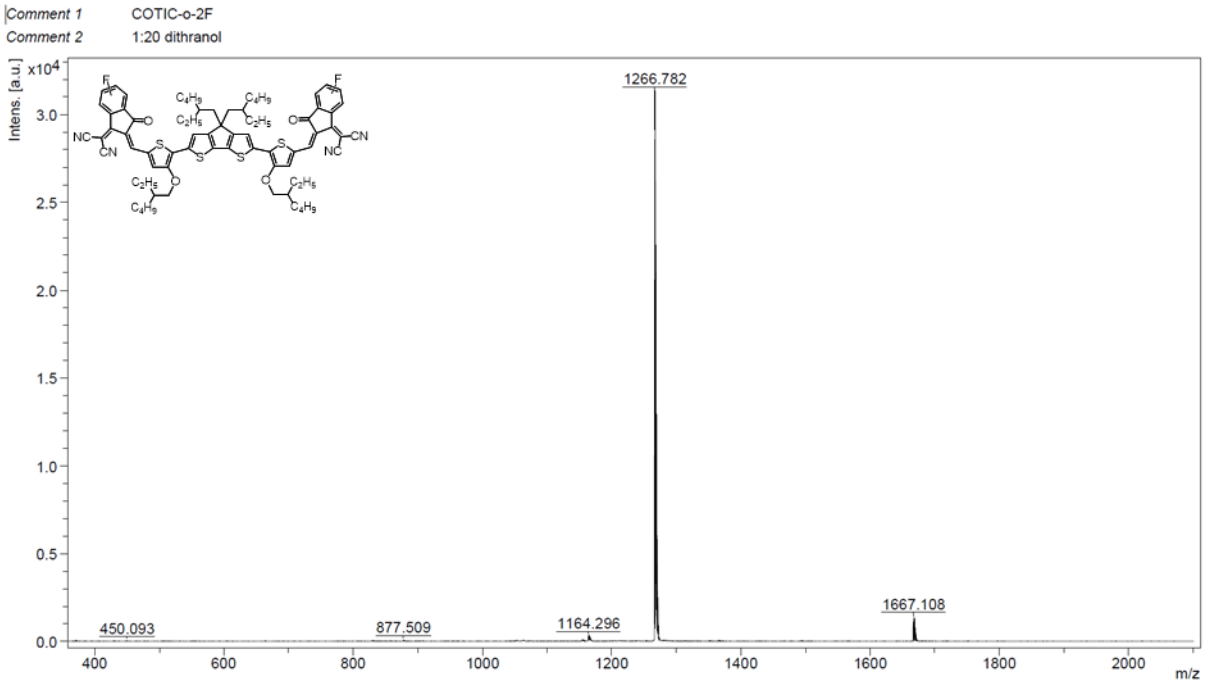
Comment 1 COTIC-o-2F
Comment 2 1:20 dithranol
Intens. [a.u.]
x10^4
1266.782
1667.108
450.093
877.509
1164.296
m/z

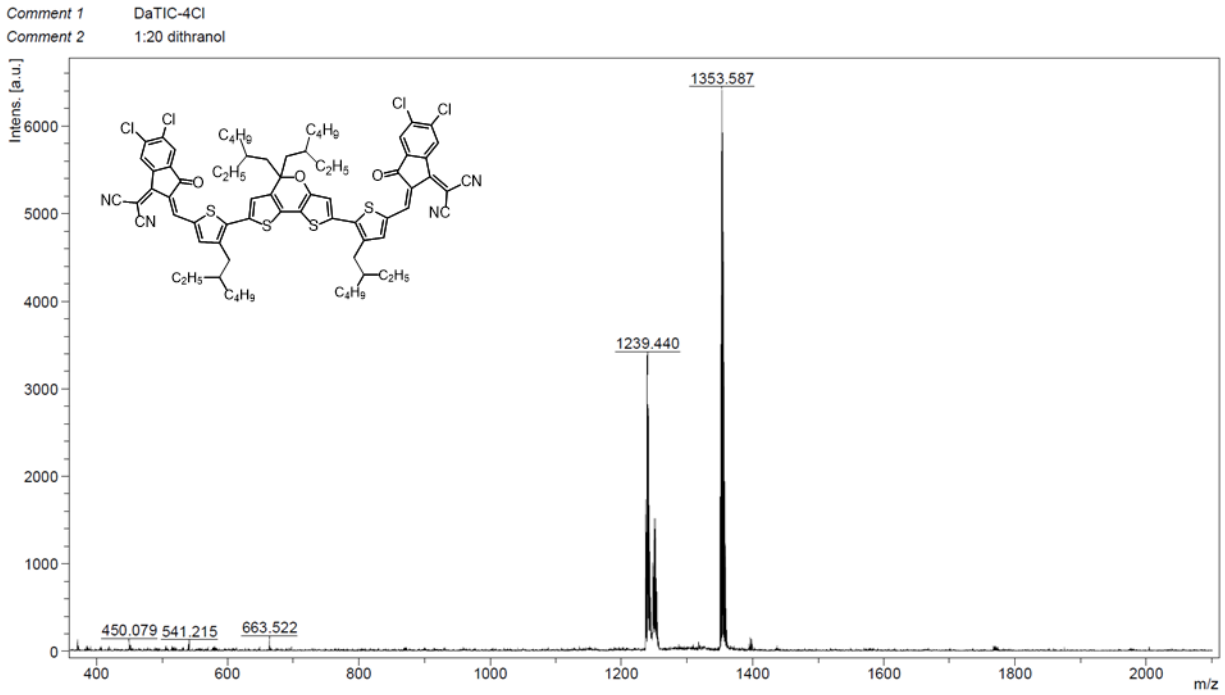
Comment 1 DaTIC-4Cl
Comment 2 1:20 dithranol
Intens. [a.u.]
1353.587
1239.440
450.079
541.215
663.522
m/z

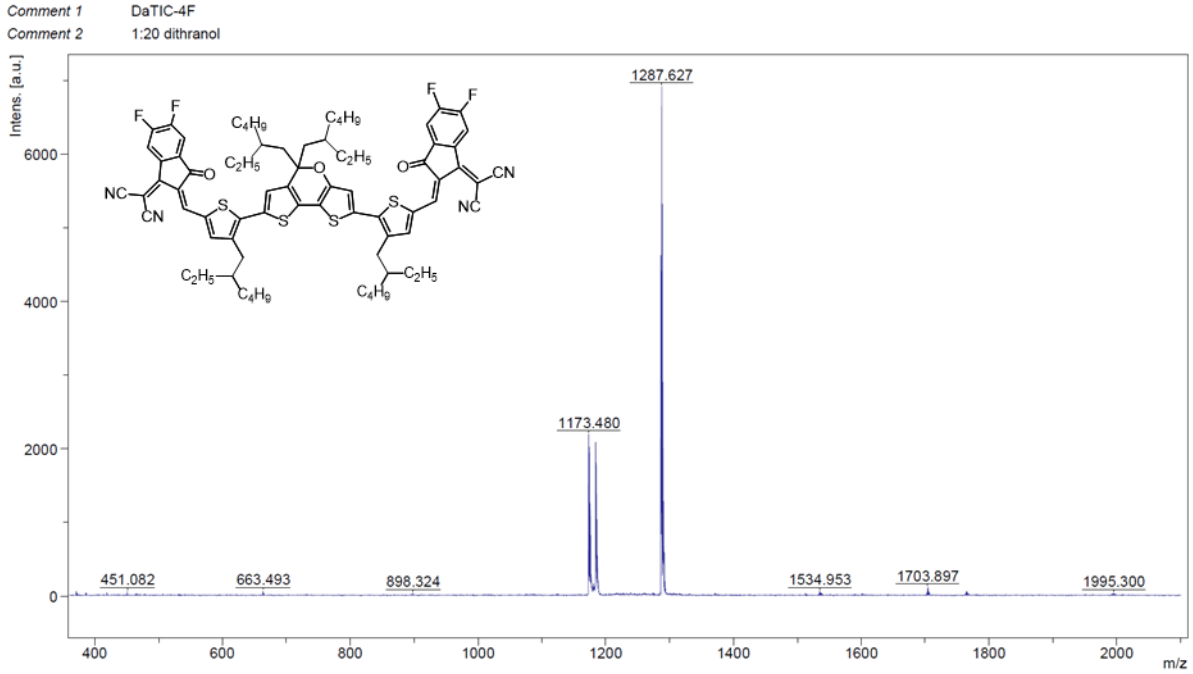
Comment 1 DaTIC-4F
Comment 2 1:20 dithranol
Intens. [a.u.]
1287.627
1173.480
451.082
663.493
898.324
1534.953
1703.897
1995.300
m/z